UNIVERSITÀ DEGLI STUDI DI TRIESTE

XXVIII CICLO DEL DOTTORATO DI RICERCA IN
ENVIRONMENTAL AND INDUSTRIAL FLUID MECHANICS

Large-eddy simulation of wind-driven circulation in a peri-alpine lake: implications of complex surrounding orography and thermal stratification on hydrodynamics of Lake Ledro

settore disciplinare ICAR/01

PH.D STUDENT:
Marco Antonio SANTO
PH.D. PROGRAM COORDINATOR:
Prof. Pierpaolo OMARI
P. Om
THESIS SUPERVISOR:
Prof. Vincenzo ARMENIO
VArmenio
THESIS CO-SUPERVISOR:
Dr Federico ROMAN
Federico Roman

Academic Year 2015–2016

Abstract

In the present thesis I investigate the wind-driven circulation and mixing in a peri-alpine lake (Lake of Ledro) located in Trentino Alto Adige (Italy). It represents an interesting case study because of two main reasons: it is surrounded by mountains, which affect wind distribution and consequently produce a non homogeneous wind stress of the lake surface; in recent years the lake has suffered for intense blooms of the harmful cyanobacterium *Planktothrix Rubescens*, occurring in the winter season, characterized by the absence stratification. The study is carried out numerically, using a high-resolution, eddy resolving Large Eddy Simulation (LES) model (LES-COAST). The model resolves directly the large scales of motion and parametrizes the small ones by means of the Anisotropic Smagorinsky Model (ASM). The complexity of the coastline and bathymetry is treated by the Immersed Boundary Method which, combined with a curvilinear grid, provides a feasible tool for the study of the hydrodynamics of semi-closed or closed areas like a peri-alpine lake. To the best of author's knowledge this work represents the first application of a LES model to an actual lake as whole, considering its shape and its dimensions.

Two types of boundary condition for the time changing wind stress are used: spatially homogeneous and non-homogeneous. The former is reproduced by applying to the lake's surface the wind velocity and the direction measured by a floating meteo station located in the center of the lake during the week 16-22 of January 2012, whereas the latter is obtained by the regional scale Weather Research and Forecasting model (WRF) for the same week, making a first attempt of coupling air-water models. The analysis of the wind-driven circulation, as well as of the high-order statistics, has been performed with the aforementioned wind conditions. The analysis shows the presence of downwelling/upwelling areas along the windward/leeward coastline respectively, providing an explanation of the bloom of cyanobacterium at the lake surface observed under winter conditions. Moreover, peculiar superstreaks, which span over the entire depth of the lake, have been simulated, enhancing the vertical mixing in the water column. The bottom boundary layer has been studied in both unstratified and stratified case. The role of the Coriolis force in such a small lake is highlighted, together with the effect of the simplification of the computational domain with respect to the actual geometry. The eddy viscosities values have been computed and they have shown, among other analysis, the presence of a minimum stress plane which has been confirmed by the study of the Turbulent Kinetic Energy. The evolution in time of the TKE and its dissipation rate in both wind regimes indicate the presence of equilibrium turbulence even under the unsteady conditions herein studied, moreover it provide an estimation of phase lag of the two quantities between the surface and the bottom of the lakes. Under wind inhomogeneity, turbulent mixing appears enhanced with respect to the simplified homogeneous wind case. In presence of thermal stratification the eddy viscosities, the turbulent kinetic energy and TKE dissipation rate are smaller with respect to the non stratified case, and evidences of the presence of the BBL in the stratified case are provided. Convergence and divergence areas confined in the surface mixed layer are shown, in particular in presence of strong wind squalls and inhomogeneity they appear aligned with the isotherms. The present thesis has to be considered as a first step toward the study of the hydrodynamics and of the internal waves in stratified lakes with different wind conditions.

Contents

List of Figures

Chapter 1

Chapter 2

Chapter 3

Chapter 4

Chapter 5

Chapter 6

Chapter 7

Chapter 1

INTRODUCTION

Lakes and reservoirs are complex systems where transport of substances (oxygen, nutrients, pollutants) and heat (affecting the thermal stratification) depend on slow flows. The primary source of momentum is the wind stress on the water surface, so that mixing is effective in the surface layer, while the interior remains relatively calm (e.g. Wuest and Lorke, 2003). Mixing is further reduced in presence of a strong density stratification, which can reduce the exchanges across the pycnocline even to molecular diffusion rates. In this context, convective flows and large scale turbulent structures are important because they effectively contribute to the vertical transport, producing local downwelling and upwelling phenomena that are not easily modelled.

Modelling turbulence in lentic systems is indeed a complicate issue. Standard applications rely on Reynolds Averaged Navier-Stokes (RANS) equations, possibly including transport equations for the turbulent kinetic energy and its dissipation rate (e.g., k-ϵ models). In case of small basins, stratification, rotation and topographic effects, together with the wind-driven source of momentum, make the calibration of large scale circulation models difficult, and suggest the use of eddy-resolving models (see Burchard (2008) for a discussion). Among the alternative choices, direct numerical simulations (DNS), based on the solution of the three-dimensional, unsteady, Navier-Stokes equations up to the dissipation (Kolmogorov) scales of turbulence are unfeasible due to a non-affordable computational cost (see Piomelli (1999) for a discussion). Over the last 30 years, large eddy simulation (LES), an intermediate technique between RANS and DNS, has proved to be a good candidate to solve fluid dynamic problems characterized by complex physics and geometry. In LES the large scales of turbulence, more anisotropic and energetic, are solved directly through a 3-dimensional unsteady simulation, while the small scales, which are dissipative and characterized by a more universal behaviour, are modelled by using a subgrid scale (SGS) model. LES has proved to be a useful tool to simulate complex flows, whose accurate reproduction is not straightforward using standard RANS-like methodologies (Sarkar and Armenio, 2013).

Very few examples are present in literature where LES has been used to study hydrodynamic processes in lakes or coastal basins. LES was used to understand processes involved in sidearms of lakes due to thermal forcing in absence of wind (Dittko et al, 2013), and to investigate fundamental processes occurring in real scale basins but referring to simple rectangular domains (Sander et al., 2000; Scalo et al., 2013; Mironov et al., 2002). Recently, an eddy-resolving LES model (LES-COAST) has been developed to simulate the hydrodynamics within full-scale closed or semi-closed coastal basins (Roman et al., 2010). Complex coastline and bathymetry are reproduced by a combination of curvilinear structured grid and immersed boundaries (Roman et al., 2009b). The SGS momentum and temperature fluxes are parameterized by the Anisotropic Smagorinsky Model (ASM), designed to work for the highly anisotropic grid cells required for simulations where the horizontal length scales are more than one order of magnitude larger than the vertical ones (Roman et al., 2010). The model was successfully used to reproduce wind-driven circulations in the industrial harbour of Trieste (Italy) (Petronio et al., 2013) and in the Barcelona harbour (Spain) under typical conditions (Galea at al., 2014).

So far, LES-COAST has been applied for coastal areas considering a constant unidirectional and homogeneous wind stress at the air-water surface. However, such approach is not appropriate for lakes where the surrounding orography is complex and the wind field is strongly inhomogeneous (Laval et al., 2003; Rueda et al., 2005). In fact, distinctive features of lakes located in complex orography contexts are thermally-driven atmospheric circulations. They develop especially in clear-sky days and mark the local wind climatology with a pronounced daily periodicity, as their direction regularly reverses between day and night (Serafin and Zardi, 2010; Rampanelli et al., 2004). Thermally-driven circulations may develop at a valley scale (up-valley during the day and down-valley at night) and/or at smaller scales, influencing only a slope of the valley and, hence, a portion of the lake. As a consequence, wind data that can be derived from punctual observations may not be representative of the actual spatial distribution of the wind speed and direction over the lake. In these cases fine resolution meteorological simulations are needed to properly take into account the mechanical effects of the topography on the wind field and to adequately simulate the development of thermally-driven local circulations.

In the present thesis the wind-driven circulation in a lake has been studied using an eddy-resolving model and considering the actual geometric features of the lake and the surrounding, first with a neutral stratification then in presence of a thermal stable stratification. In the former case a spatial homogeneous wind field is used, both steady and varying in time according to the data recorded by a meteorological station located at the center of the lake (Fig. 1.1a); finally is used the realistic wind forcing obtained from high-resolution inhomogeneous and time-dependent wind fields simulated by means of the atmospheric Weather Research and Forecasting model (WRF), a well-known meteorological model which can be applied to study sites with small horizontal and vertical dimensions in complex terrain (Papanastasiou et al. (2010), Arrilaga et al. (2016)). Whereas, for the stratified case, an homogeneous steady wind field first, and then an inhomogeneous wind have been applied.

Among the others, Lake Ledro (northern Italy, see Fig. 1.1) is an interesting site to be studied with a LES model for three main reasons.

- Lake Ledro serves as a water reservoir for the hydroelectric power plant in Riva del Garda, and represents one of the main tourist attractions in the area. In recent years, the lake has been subject to abundant blooms of the harmful cyanobacteria *Planktothrix Rubescens* (Barbato,

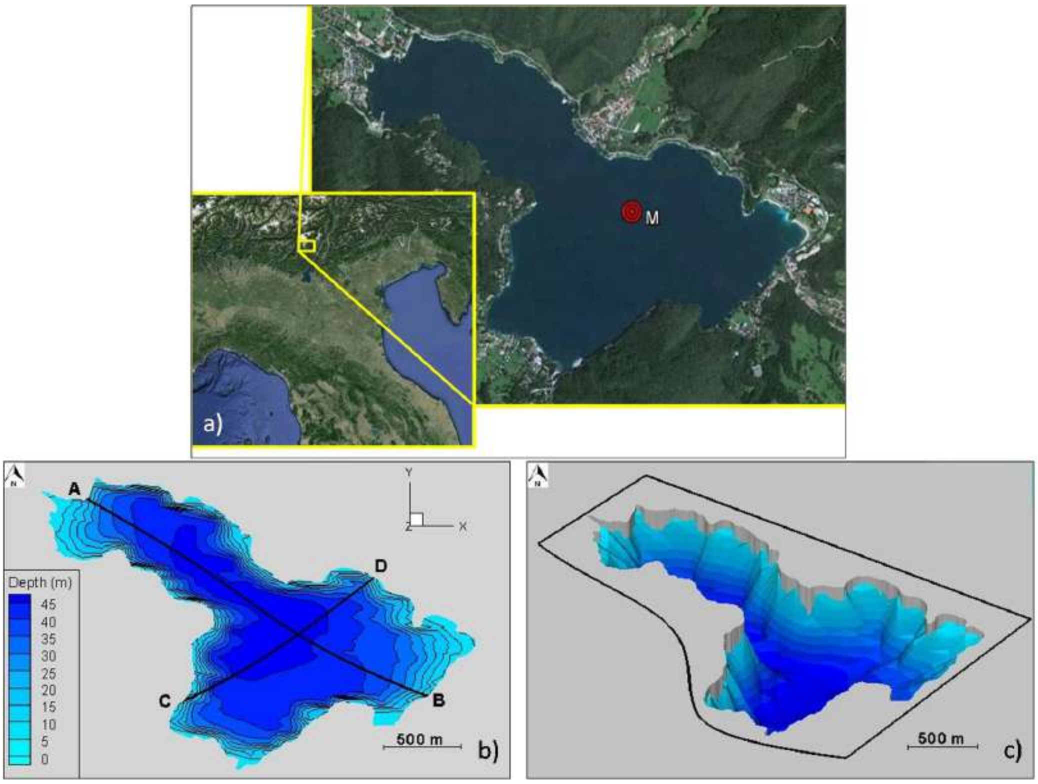

Figure 1.1: Position and bathymetry of Lake Ledro: a) satellite image and location, the red point indicates the position of the platform hosting the meteorological station; b) depth contours and main axes AB and CD; c) bathymetry reconstructed by the Immersed Boundary Method (IBM), showing the edge of the curvilinear computational domain (in black), the rigid bodies of shoreline (in grey) and bathymetry (blue). The vertical dimension in (c) is elongated by a factor 500 with respect to the horizontal axes. The same distortion is applied also in the following figures.

1977), similar to what happened in other sub-alpine lakes in Europe (Salmaso et al., 2006; D'Alelio and Salmaso, 2011). In this respect, the blooms of *P. rubescens* have become a matter of serious concern for local communities and for the regional administration. While it has been recognized that the nutrients loads (primarily phosphorus) related to agriculture and livestock associated to the presence of a waste water treatment plant play a role in the ecological problem (Boscaini et al., 2012), the influence of physical processes on the transport of cyanobacteria is not completely clarified yet.

The optimal conditions for the growth of *P. rubescens* during summer and autumn occur at the lower end of the metalimnion (10-20 m). They appear at the lake surface in winter time, producing red patches floating over the surface, with a rate that is not justified by their own mobility. Indeed, these cyanobacteria are able to regulate their position depending on temperature stratification by means of vacuoles, which allow them to move slowly in the water column, with a velocity of just about 40-80 cm/day (Posch et al., 2012; Whitton, 2012). The vertical movement is primarily related to the weakening of the thermal stratification. Together with the observation that blooms are mostly present along the windward coast (Boscaini et al., 2012), this suggests that physical processes like upwelling, which can accelerate the surface spreading, may affect the phenomenon in a significant way.

- Lake Ledro (Fig.1.1) is located in Trentino (Italy) at 652 m a.s.l. and comprises a surface area of 2.1 km^2, a capacity of 68×10^6 m^3 and a maximum depth of 48 m. It is located in a valley surrounded by a complex orography with peaks that reach 1988 m a.s.l., close to Lake Garda, where distinctive thermally-driven circulations develop (Laiti et al., 2014; Giovannini et al., 2015). Local orographic features channel the wind to certain directions and, together with vegetation canopy or anthropogenic structures, affect the wind distribution (Laval et al., 2003; Rueda et al., 2005), resulting in peculiar lake circulations (Podsetchine and Schernewski, 1999; Rubbert et al., 2004; Toffolon and Rizzi, 2009).

- Its own dimensions allow for numerical simulations to be performed in a reasonable computational time using a sufficiently refined grid able to reproduce the main structures of the turbulence motion.

Here is simulated first a winter case where thermal stratification is nearly absent then a spring case with a stable thermal stratification. The winter is known as a typical period for *P. rubescens* to emerge at the lake surface. To this end, we selected the week 16-22 January 2012, when the maximum temperature difference along the water column was less than 0.4 °C, thus allowing to neglect buoyancy effects on lake hydrodynamics as a first approximation. For the spring case an idealized stable stratification has been used with a temperature difference between the surface and the bottom of about 5°C. The aim is to improve the knowledge of the large-scale turbulent structures that develop in complex lakes, and to detect the processes that facilitate the upwelling of the toxic cyanobacteria up to the lake surface.

The thesis is structured as follows. Chapter 2 describes the mathematical model and the main features of LES-COAST model; Chapter 3 reports the characteristics of the meteorological simulation and the reconstruction of the wind forcing and of the computational domain. In Chapter 4 a preliminary simulation of the wind driven circulation in a simplified domain with a constant and steady wind will be presented. In Chapter 5 are discussed the results for an idealized case where the wind measured at the center of the lake is applied homogeneously over the surface of the lake. Results for the realistic case with the inhomogeneous wind are in Chapter 6. Then Chapter 7 will reports the results of the stratified case. Finally, in Chapter 8 concluding remarks are given.

Chapter 2

LES-COAST MODEL

2.1 Turbulent Environmental Flow

Environmental flows are characterised by high value of Reynolds Number which means high turbulence intensity. Turbulent flow carries vorticity and is composed by eddies of different size interacting each other. The larger eddies, comparable to the dimension of the flow domain, extract energy from the mean flow therefore are responsible of producing turbulent energy. These large eddies break up in smaller and smaller eddies producing the energy cascade till reaching the Kolmogorov scale which is the characteristic length where viscous forces are no more negligible and dissipation of turbulent energy occurs. Between the large scale eddies and the smaller ones, when Re is big enough, the inertial sub-range take place, where the eddies carrying energy from the former to the latter one without dissipating it. By moving from the physical space to the frequency wave-number space is necessary visualize the distribution of the turbulent energy associated to each turbulent oscillation. As shown in Fig.2.1 the smaller wave-numbers k are representative of the large (low frequency) eddies, conversely the higher k to the small (high frequency) eddies. By increasing the Reynolds number the dissipation takes place at smaller scales thus the width of the power spectrum increases. As direct consequence the DNS that solves the entire flow field up to the Kolmogorov scales requires a number of grid points for each domain's dimension proportional to the Reynolds number ~ $Re^{3/4}$ (Piomelli (1999)). Since the number of required points have to be employed in three dimensional space and the time evolution also depends on the cell's length, the DNS computational cost rises up to Re^3 making DNS an appropriate model act to explore the physics of the flow but just for small Reynolds number. Reynolds-averaged Navier–Stokes (RANS) models on the contrary are designed to remove all the unsteady motions such as turbulence by adding an eddy-viscosity producing a laminar flow with a velocity field that is the mean of the turbulent velocity field, making this method computational less expensive. RANS method cannot perform well for high Reynolds number especially close to the wall where most turbulence is produced. As described in the next section the LES method which is a kind of middle ground model between DNS and RANS is a more appropriate model for environmental-high Reynolds number simulation.

2.2 Large Eddy Simulation Method

The environmental flows are governed by the Navier - Stokes (NS) equation. In the most of the application the NS equation are considered under the Boussinesq approximation which assume density fluctuations negligible.

As shown in the section 1 Large Eddy Simulation methodology is based on the idea that the large energy-containing eddies, affected by boundary condition and varying from flow to flow, are resolved while the smaller ones are modelled. The concept arises from the properties of the small scales turbulent structures: they are produced by large eddies and are homogeneous, isotropic, dissipative and reach the equilibrium shortly compared to the largest ones, because of these properties they can be considered universal, thus the smaller structures can be modelled.

Because of these classification is necessary to split the variables in resolved large scale part ($\overline{f}$), which length are comparable with the grid's cell dimension $\Delta_{x,y,z}$, and unresolved Sub Grid Scales (SGS) part (f') by applying a filter

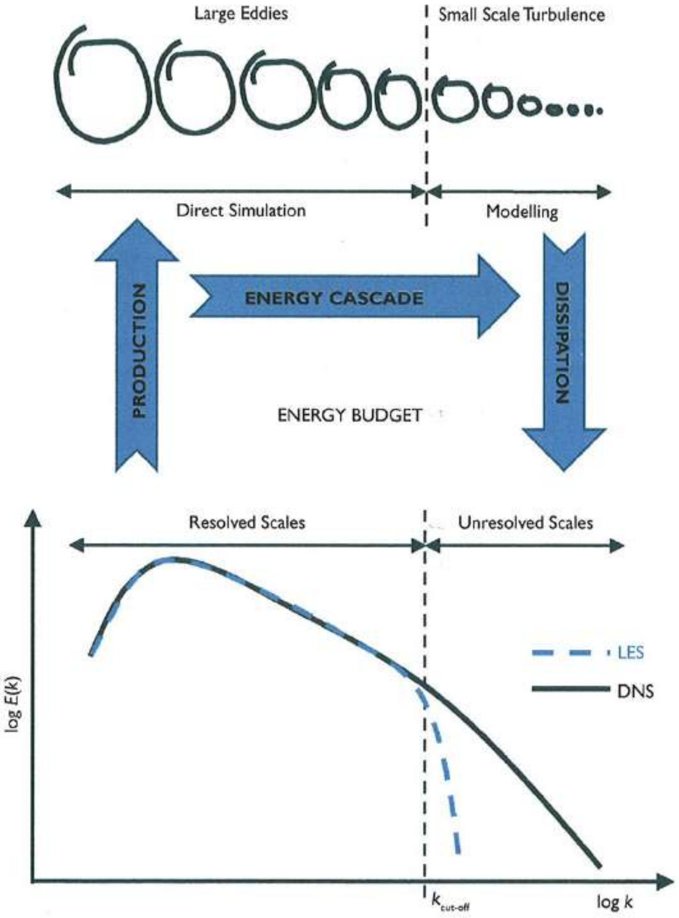

Figure 2.1: Energy flux and turbulent power spectra of an energy cascade in relation with the resolved and modelled part of turbulence in LES models. source:Rodi (2013)

$$\overline{f}(x) = \int_D G(x - x')f(x')dx' \tag{2.1}$$

where D is the entire domain and G is the top-hat filter function defined as:

$$G(x) = \begin{cases} 1/\bar{\Delta} & \text{if } \mid x \mid \leq \bar{\Delta}/2 \\ 0 & \text{otherwise} \end{cases} \tag{2.2}$$

where the $\bar{\Delta}$ is proportional to the grid's cell characteristic length and affect the precision of the simulation. It's important to choose an appropriate filter width in order to let the eddies associated to a wavenumber scale $k_{cut-off}$ $(O(2\pi/\bar{\Delta}))$ to belong to the sub-inertial range. By applying this filter to the NS equations we obtain

$$\frac{\partial \overline{u}_i}{\partial x_i} = 0\,, \tag{2.3}$$

$$\frac{\partial \overline{u}_i}{\partial t} + \frac{\partial \overline{u}_i \overline{u}_j}{\partial x_j} = -\frac{1}{\rho_0}\frac{\partial \overline{p}}{\partial x_i} + \nu \frac{\partial^2 \overline{u}_i}{\partial x_j \partial x_j} - 2\epsilon_{ijk}\Omega_j \overline{u}_k - \frac{\overline{\rho}}{\rho_0} g_i \delta_{i,3} - \frac{1}{\rho_0}\frac{\partial \tau_{ij}^{SGS}}{\partial x_j}\,, \tag{2.4}$$

where u_i, Ω_i and g_i are the i-th components of the velocity, earth rotation and gravitation acceleration vectors respectively, ϵ_{ijk} is the Levi-Civita symbol, p is the hydrodynamic pressure and ν the kinematic viscosity. Here u_1, u_2, u_3 or u, v, w denote the velocity components along x_1, x_2, x_3 or x, y, z The frame of reference has the origin over the free surface, x_1, x_2 over the horizontal plane and x_3 pointing upward. The filtering operation applied to the non-linear term of the NS equation introduces the subgrid-scale (SGS) Reynolds stress

$$\tau_{ij}^{SGS} = \overline{u_i u_j} - \overline{u}_i \overline{u}_j \tag{2.5}$$

In particular the term τ_{ij}^{SGS} comes up from the Leonard's decomposition of the filtered nonlinear advection term:

$$\overline{u_i u_j} = \underbrace{\overline{\overline{u}_i \overline{u}_j} - \overline{u}_i \overline{u}_j}_{\mathbf{L}} + \underbrace{\overline{\overline{u}_i u'_j} + \overline{\overline{u}_j u'_i}}_{\mathbf{C}} + \underbrace{\overline{u'_i u'_j}}_{\mathbf{R}} + \overline{u}_i \overline{u}_j. \tag{2.6}$$

and represents the effect of the unresolved fluctuations on the resolved motion, it can be expressed as a summation of three terms:

- L is called Leonard Term or *outscatter* term, it represents the interaction among two large-scales eddies which produces small-scale turbulence;
- C represents the interaction between the large-scales eddies and the small-scales eddies, it can transfer energy in either direction, this is why is called *cross* term.
- R is the *backscatter* term which represents the interaction between two small-scales eddies and large-scale eddies producing transferring of energy from the small to the large scales eddies.

The term (τ_{ij}^{SGS}), that represent the effect of the small scale on the resolved scales, must be modelled by an SGS Model.

2.2.1 Smagorinsky Model

Despite the fact τ_{ij}^{SGS} represents different physics and different interaction between large-resolved and small-scales eddies the SGS stresses are modelled as an entire unit. These stresses need to be modelled by means of a subgrid-scale model: based on the idea that turbulence can be represented as an increased viscosity, the Smagorinsky model Smagorinsky (1963) assume that the anisotropic part of the subgrid-scale stress tensor τ_{ij}^{SGS} is related to the resolved strain rate tensor $\overline{S}_{ij}$ through a SGS eddy viscosity ν_τ as follows:

$$\tau_{ij}^{SGS} - \frac{\delta_{ij}}{3}\tau_{kk} = -2\nu_T\overline{S}_{ij} = -\nu_T\left(\frac{\partial\overline{u}_i}{\partial x_j} + \frac{\partial\overline{u}_j}{\partial x_i}\right). \tag{2.7}$$

where ν_T is the eddy viscosity parameter which can be defined as the product of a turbulent velocity scale (q_{sgs}) and a length scale (l):

$$\nu_T = q_{sgs}l. \tag{2.8}$$

The velocity scale arises from a balance between the dissipation of the turbulent kinetic energy due to the small eddies (ϵ_{SGS}) and the energy transferred from the resolved scales to the smaller ones ($\tau_{ij}\overline{S}_{ij}$).

$$\epsilon_{SGS} = -\tau_{ij}^{SGS}\overline{S}_{ij} \tag{2.9}$$

By taking ϵ_{SGS} as q_{sgs}^3/l and using 2.7, 2.8, 2.9 we get

$$q_{sgs} = \sqrt{2\overline{S}_{ij}\overline{S}_{ij}}l = |\overline{S}_{ij}|l \tag{2.10}$$

leading to

$$\nu_T = l^2|\overline{S}_{ij}|. \tag{2.11}$$

Whereas the length scale is proportional to the dimension of the cell, $\Delta_{x,y,z}$ as follows:

$$l = C_s\Delta_{x,y,z} \tag{2.12}$$

where C_s is the Smagorinsky constant commonly considered between 0.065 and 0.2 which depend on the flow field. Finally the eddy viscosity can be written as below:

$$\nu_T = (C_s\Delta)^2|\overline{S}_{ij}| \tag{2.13}$$

In the case of coastal areas, as well as for lakes, finding a unique length scale representative of the three dimensions of the cells could lead to an overestimation of the eddy viscosity in all directions because of the strong anisotropy of the cells used to discretize the domain. In order to overcome this problem the ASM developed by Roman et al. (2010) has been adopted. The model uses a two-SGS-eddy-viscosity (vertical and horizontal) concept. The quantities are defined as:

$$\nu_{\tau,V} = (C_V L_V)^2\,|\overline{S}_V|\,, \tag{2.14}$$

$$\nu_{\tau,H} = (C_H L_H)^2\,|\overline{S}_H|\,, \tag{2.15}$$

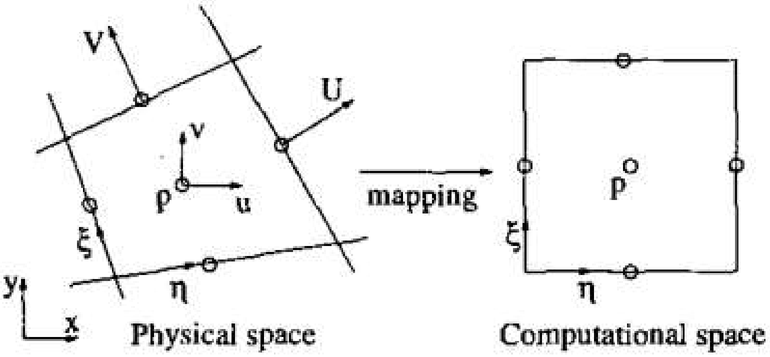

Figure 2.2: Control volume of a non-staggered grid.

where $L_H = \sqrt{{\Delta_x}^2 + {\Delta_y}^2}$ and $L_V = \Delta_z$, and

$$|\overline{S}_H| = \sqrt{2\overline{S}_{11}^2 + 2\overline{S}_{22}^2 + 4\overline{S}_{12}^2}\,, \tag{2.16}$$

$$|\overline{S}_V| = \sqrt{4\overline{S}_{13}^2 + 2\overline{S}_{33}^2 + 4\overline{S}_{23}^2}\,. \tag{2.17}$$

In the equations above, the subscripts V and H stand for vertical and horizontal respectively. The calibration of the empirical constants C_V and C_H was carried out in Roman et al. (2010) by simulating a standard turbulent-plane Poiseuille flow with increasing grid anisotropy, quantified through the grid aspect-ratio $\sqrt{\Delta_x^2 + \Delta_y^2}/\Delta_z$ (with $\Delta_x \sim \Delta_y$), and comparing the results with reference experimental and benchmark numerical data. In our case the average aspect ratio is $L(H)/L(V) \approx 10$, suggesting us to adopt $C_H = 0.028$ and $C_V = 0.3$ (see Roman et al. (2010)).

2.2.2 Curvilinear Coordinates

Geophysical flows have often irregular geometries, it can be helpful to discretize the domain by curvilinear grids (ξ_i) in order to optimize the inactive cells (see Fig. 2.2). The governing equation are transformed in curvilinear form:

$$\frac{\partial U_m}{\partial \xi_m} = 0 \tag{2.18}$$

$$\frac{\partial J^{-1}u_i}{\partial t} + \frac{\partial F_{im}}{\partial \xi_m} = J^{-1}B_i \tag{2.19}$$

in which B_i represent the body forces like Coriolis and buoyancy and F_{im} is defined as:

$$F_{im} = U_m u_i + J^{-1}\frac{\partial \xi_m}{\partial x_i}p - \nu G^{mn}\frac{\partial u_i}{\partial \xi_n} \tag{2.20}$$

where $\xi_m, (m = 1, 2, 3)$ are the coordinates in transformed computational space$(\xi = (x, y, z), \eta = (x, y, z), \zeta(x, y, z))$, and

- $J^{-1} = det(\frac{\partial x_i}{\partial \xi_j})$ inverse of the Jacobian, it represents the volume of the cell
- $U_m = J^{-1}\frac{\partial \xi_m}{\partial x_j}u_j$ is the volume flux normal to the surface of constant ξ_m
- $G^{mn} = J^{-1}\frac{\partial \xi_m}{\partial x_j}\frac{\partial \xi_n}{\partial x_j}$ mesh skewness tensor

The transformed pressure term represents the flux of the pressure gradient through the faces of the cell in the physical domain, while the third term on the right hand side of equation (2.20) is the transformed diffusive term, which represents the fluxes of the viscous stresses through the cell faces of the cell.

The solution of equations 2.18 and 2.19 is based on fractional step method described in Zang et al. (1994). The non staggered grid shown in Fig. 2.2 is applied: the pressure and Cartesian velocity are defined at the center of the cell while contravariant fluxes (denoted by capital letters) are defined at the boundary of cells. By discretizing the momentum equation gives:

$$\begin{aligned} J^{-1}\frac{u_i^{n+1} - u_i^n}{\Delta t} = \frac{3}{2}(C(u_i^n) + D_E(u_i^n) + B_i^n) - \frac{1}{2}(C(u_i^{n-1}) + \\ D_E(u_i^{n-1}) + B_i^{n-1}) + R_i(p^{n+1}) + \frac{1}{2}(D_I(u_i^{n+1}) + D_I(u_i^n)) \end{aligned} \tag{2.21}$$

where

$$C_i = -\frac{\partial}{\partial \xi_m}(U_m u_i), \tag{2.22}$$

$$R_i = -\frac{\partial}{\partial \xi_m}(J^{-1}\frac{\partial \xi_m}{\partial x_i}), \tag{2.23}$$

$$D_I = -\frac{\partial}{\partial \xi_m}(\nu G^{mn}\frac{\partial}{\partial \xi_n}), \quad m = n \tag{2.24}$$

$$D_E = -\frac{\partial}{\partial \xi_m}(\nu G^{mn}\frac{\partial}{\partial \xi_n}), \quad m \neq n. \tag{2.25}$$

$\delta/\delta\xi_m$ represents discrete finite difference operators in the computational space; superscripts represent the time step; C represents the convective term; R_i is the discrete operator for the pressure gradient terms; and D_E and D_I are discrete operators representing respectively the off-diagonal viscous terms (treated explicitly) and the diagonal viscous terms (treated implicitly). The time-advancement is carried out by using the second order accurate Adam-Bashfort method for the explicit terms (C_i and D_E) and the Crank-Nicolson scheme for the implicit term D_I. With the exception of the convective terms, which is discretized by a QUICK scheme all the spatial derivatives are approximated by second-order central differences. The fractional step method used to solve 2.21 consists in splitting the solution procedure in two steps: *predictor* and *corrector* part. The former part solves the *intermediate velocity* u^* which satisfy the advective and diffusive transport and body force action only:

$$\begin{aligned}\left(I - \frac{\Delta t}{2J^{-1}}\right)(u_i^* - u_i^n) = \frac{\Delta t}{J^{-1}}[\frac{3}{2}(C_i^n + D_E(u_i^n) + B_i^n) - \\ \frac{1}{2}(C_i^{n-1} + D_E(u_i^{n-1}) + B_i^{n-1}) + R_i(p^{n+1}) + \frac{1}{2}(D_I(u_i^{n+1} + u_i^n))]\end{aligned} \tag{2.26}$$

in which I is the identity matrix. The *corrector* step finds u_i^{i+1} by means of u^*, which satisfies the continuity equation, both velocities are related to the pressure gradient by:

$$u_i^{n+1} - u_i^* = \frac{\Delta t}{J^{-1}}[R_i(\phi^{n+1})] \tag{2.27}$$

the variable ϕ is related to p as follows:

$$R_i(p) = \left(J^{-1} - \frac{\Delta t}{2} D_I\right)\left(\frac{R_i(\phi)}{J^{-1}}\right) \tag{2.28}$$

By interpolating the 2.27 to the cell's faces we obtain:

$$U_m^{n+1} = U_m^n - \Delta t\left(G^{mn}\frac{\partial \phi^{n+1}}{\partial \xi_n}\right) \tag{2.29}$$

in which U_m^* is the intermediate volume flux and is defined as: $U_m^{n+1} = J^{-1}(\partial \xi_m / \partial x_j) u_j^*$. By substituting 2.29 into the continuity equation finally we obtain the Poisson equation for ϕ^{n+1}

$$\frac{\partial}{\partial \xi_m}\left(G^{mn}\frac{\partial \phi^{n+1}}{\partial \xi_n}\right) = \frac{1}{\Delta t}\frac{\partial U_m^*}{\partial \xi_m} \tag{2.30}$$

which is solved by a multigrid method.

2.3 Computational Domain and Boundary Conditions over the Solid Walls

The coastal flow, as well as lakes, have an irregular shape which is hard to be discretized optimally. The methodology that is used to overcome this obstacle consist of two tools:

- Curvilinear Grids (described in sec 2.2.2) which is able to optimize the number of cells aimed at solving the fluid part of the computational domain without resort to body-fitted mesh, representing a tough job for an irregular domain.

- Immersed Boundary Method (IBM) reconstructing the shoreline and bathymetry of the domain which are immersed in the curvilinear grid changing the equation of momentum by introducing a discrete body forces that mimics the effect of the solid boundaries. This methodology, initially designed for orthogonal grids, has been adapted to the curvilinear coordinates by Roman et al. (2009b).

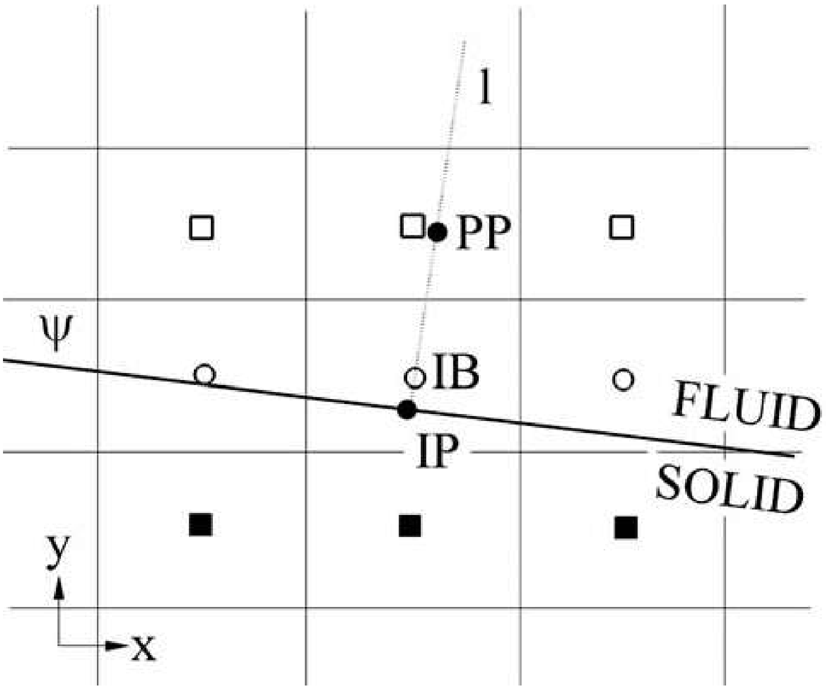

Figure 2.3: Classification of solid nodes (■), immersed body nodes (○) and fluid nodes (□) depending on the interface Ψ for a two-dimensional grid. Identification of the Intersection Point (IP) and Projection Point (PP) relative to the Immersed Boundary node IB.

When simulating wall-bounded turbulence for real-scale environmental problems via LES, the direct solution of the viscous wall layer is infeasible because of the difficulties to explicitly parametrize the wall roughness from one hand, and because of the computational time required to fulfill this task. The total cost of a simulation solving the inner layer by LES has been estimated to scale as $Re^{2.4}$ because of the fine mesh required to solve the smaller turbulent structures that develop close to the boundaries Piomelli (2008). In order to circumvent this problem, among the others, a technique is to skip the solution of the near-wall layer and to parametrize the wall-shear stress through a model. When this technique is employed in conjunction with Immersed Bodies (IBs), since the grid cell is usually not aligned with the IB, the imposition of a shear stress becomes difficult and undesirable consequences like velocity much higher or wall shear stress much smaller than the expected values could show up. In order to model the wall shear stress in conjunction with the IBM methods LES-COAST use the wall-layer model developed by Roman et al. (2009a). It is based, first, on the evaluation of the velocity off the solid surface (IB point) reconstructed from an interior point (PP point) assuming that the velocity profile has a logarithm shape, second, on the evaluation of an eddy viscosity necessary for the reconstruction of the shear stress at the IB-cell's interface (see Fig. 2.3). Since the integral scale of the first off boundary point is too small any SGS model is infeasible. Based on the mixing lenght theory a RANS-like eddy viscosity is adopted:

$$\nu_t = C_w \kappa u_\tau d_{IB} \tag{2.31}$$

where d_{IB} is the distance between the IB point and the surface of the immersed boundary, κ is the von Karman constant, u_τ is the shear velocity, and $C_w \approx 1.5$ the intensification coefficient which relate the Reynolds shear stress at the cell's interface with the wall shear stress.

Chapter 3

RECONSTRUCTION OF DOMAIN AND WIND FORCING

3.1 Reconstruction of the Computational Domain

Lake Ledro has an irregular shape that is difficult to reproduce numerically using structured-grid solvers. Here I used the mixed approach which takes advantage of the curvilinear grids for reproducing the gross structure of the bathymetry and of the Immersed Boundary Method (IBM) for the details not reproducible using curvilinear structured grids (see Section 2.3).

Figure 1.1c depicts the shoreline and bathymetry. A curvilinear grid (whose upper boundary lines are depicted in black) was generated and the immersed boundaries (IBs) were introduced to reproduce the actual bathymetry.

For the present study, the computational domain is discretized into 256 points along the north-west/south-east direction (parallel to axis AB in Fig. 1.1b), 128 points along the north-east/south-west direction (parallel to axis CD), and 32 points along the vertical. The grid obtained is curvilinear in the horizontal planes and orthogonal along the vertical. As mentioned above, this results in cells size of about 12 m in the horizontal direction and 1.3 m along the vertical.

Two different values are adopted to model roughness. In order to reproduce the effect of different sediment types and vegetation, the littoral and bottom roughness is setted equal to 0.01 m and 0.003 m, respectively. The bottom roughness value was assumed in analogy with Lake Alpnach Lorke et al. (2002).

The lake surface is considered as a flat free-slip surface, over which the wind stress acts.

3.2 Reconstruction of Wind Forcing

The wind stress τ_w is computed using the wind speed (U_{10}) 10 m above the lake surface:

$$\tau_w = \rho_a C_{10} U_{10}^2 \,, \tag{3.1}$$

where ρ_a is the air density. The drag coefficient is calculated as

$$C_{10} = 0.0044\, U_{10}^{-1.15}, \qquad U_{10} < 1\,\mathrm{m\,s^{-1}} \tag{3.2}$$

$$C_{10} = (0.8 + 0.065\, U_{10}) \times 10^{-3}, \qquad U_{10} > 1\,\mathrm{m\,s^{-1}} \,, \tag{3.3}$$

with U_{10} expressed in $\mathrm{m\,s^{-1}}$.

The estimation of the drag coefficient of the former regime (3.2) was suggested by Wuest and Lorke (2003), whereas the latter relation (3.3) follows from Wu (1982). Actually, it should be considered the fact that the atmosphere is not neutral along the daily cycle. This may alter the velocity frofile. However, data on the stability of the atmosphere were not available, and, for sake of simplification, this effect on the velocity field has been neglected. Moreover, in order to trigger and sustain turbulence at the surface, a zero-mean random fluctuation (with standard deviation equal to 20% the mean value) is added to the mean wind stress (3.1). To investigate the wind-driven circulation in Lake Ledro two scenarios were considered: the Homogeneous Wind Case (HWC) and the Inhomogeneous Wind Case (IWC). The HWC is

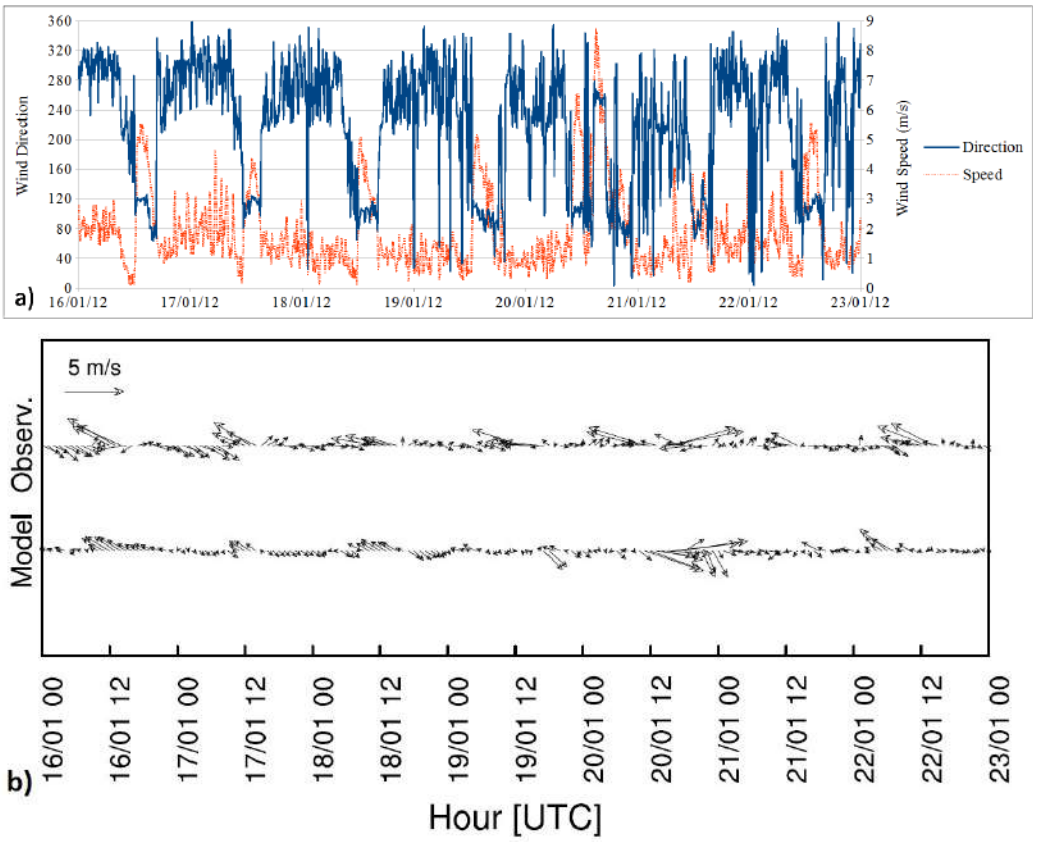

Figure 3.1: Wind speed and direction recorded at the platform M (see position in Fig. 1.1a): a) time series between 16 and 22 January 2012; b) comparison between the wind measured at the station and the value simulated by WRF.

run by using the wind direction and speed measured 2.8 m above the water surface (Fig.3.1a) by a weather station in a platform located at point M of Fig. 1.1a (Boscaini et al., 2012). Wind data are extrapolated to 10 m using the power-law wind profile described in Hsu et al. (1994), assuming a neutrally stratified atmosphere and a smooth surface with a standard roughness length of 10^{-4} m. Hence, U_{10} was obtained by multiplying the wind velocity measured at 2.8 m by a factor 1.1.

The IWC was run by using the wind speed and direction, 10 m above the surface, simulated by WRF, thus making a first step towards the coupling of air-water models. WRF is a state-of-the-art and open-source prognostic atmospheric model, and it is one of the most used tools in the meteorological community for both research and operational applications (Skamarock et al., 2008). The simulation performed for the present case covers the time period 16-22 January 2012; it starts at 18:00 UTC of 15 January 2015 and the first 6 h, being spuriously affected by the initialization, are not considered for the analysis. The horizontal domain used is composed of four two-way nested domains with 100x100, 91x91, 91x100, and 79x79 cells, and grid spacing of 10.8, 3.6, 1.2, and 0.4 km, respectively. For the vertical resolution, 27 levels are used. The initial and boundary conditions are supplied by the 6-hourly National Centers for Environmental Prediction (NCEP) Final Operational Global Analysis data on 1-degree grids. The model output is written every 15 min.

In order to perform realistic high-resolution simulations in complex terrain, a key requisite is a high-resolution topography dataset. For this reason a topography dataset with an original spatial resolution of 1" (~ 30 m) is adopted. These data are slightly smoothed to prevent numerical instability at sharp edges. As regards the land use, the Corine Land Cover (CLC) dataset updated to 2006 (http://www.eea.europa.eu) is used for the present meteorological simulations. For further details see Giovannini et al. (2015). The simulated wind velocity was obtained in WRF on 36 equally spaced points, which were mapped on each grid point at the surface of the hydrodynamic model through a bi-harmonic spline interpolation.

The simulated period (16-22 January 2012) is characterized by the development of a periodic alternation of a weak down-valley (north-westerly) wind at night and a stronger up-valley (south-easterly) wind during afternoon, reaching a typical maximum intensity of 5-6 $\mathrm{m\,s^{-1}}$ (Fig.3.1a). The periodicity of wind speed and direction is more evident in the first three days (16-18 January). In the remaining days the periodicity is less clear probably due to influence of synoptic-scale events, more evident in the afternoon of day 5, when a strong north-westerly wind, reaching 9 $\mathrm{m\,s^{-1}}$, blew for some hours. A comparison between the measured and simulated wind at the central platform in the first four days is shown in Fig. 3.1B. The numerical results are in a good agreement in the first days three days. Some disagreements are present in the last two days of the simulation, although WRF is able to reproduce the synoptic-scale event recorded at the measurement point. The disagreement does not affect the present analysis, since the results of the meteorological simulation are used here to study the effect of the spatial inhomogeneity of the wind over the lake, rather than for having a perfect reproduction of the wind at a certain location.

The following analysis first focuses on turbulence characterization using the homogeneous wind field, and then highlights the specific features originated by the spatially variable forcing. The symbol $\tilde{.}$ denotes averaging performed either in time ($\langle . \rangle_t$) or in space and time ($\langle . \rangle$), according to the specific discussion of the results presented hereafter. The quantity u'_i denotes the resolving fluctuations of the i-component of the velocity field and the quantity U_H is the module of the mean horizontal velocity field.

Chapter 4

HOMOGENEOUS STEADY WIND

Before investigating the effect of the inhomogeneity of the wind on the hydrodynamics of Lake Ledro with a neutral stratification, it is necessary to highlight both the effect of the geometry of the lake and of the Coriolis force on the turbulence's characteristics. For this purpose, in the present Chapter an idealized simplified rectangular domain is utilized, whose dimensions are similar to the dimensions of Lake Ledro, together with an homogeneous steady wind.

4.1 The Velocity Field

The Lake Ledro is represented by a rectangular domain whose dimensions are 2560m × 1280m × 38m along the major, minor and vertical axis of the lake, corresponding to the x, y and z artesian coordinates respectively. The computational domain is discretized into 256 points along the x-axis 128 points along the y-axis and 32 points along the vertical axis, resulting in an orthogonal grid with cells whose aspect ratio is similar to the one used for the discretization of Lake Ledro. The synthetic wind used over the free surface blows in the opposite direction of the x-axis, with $U_{10} = 4m/s$ giving rise to the Homogeneous Steady Wind Case (HSWC).

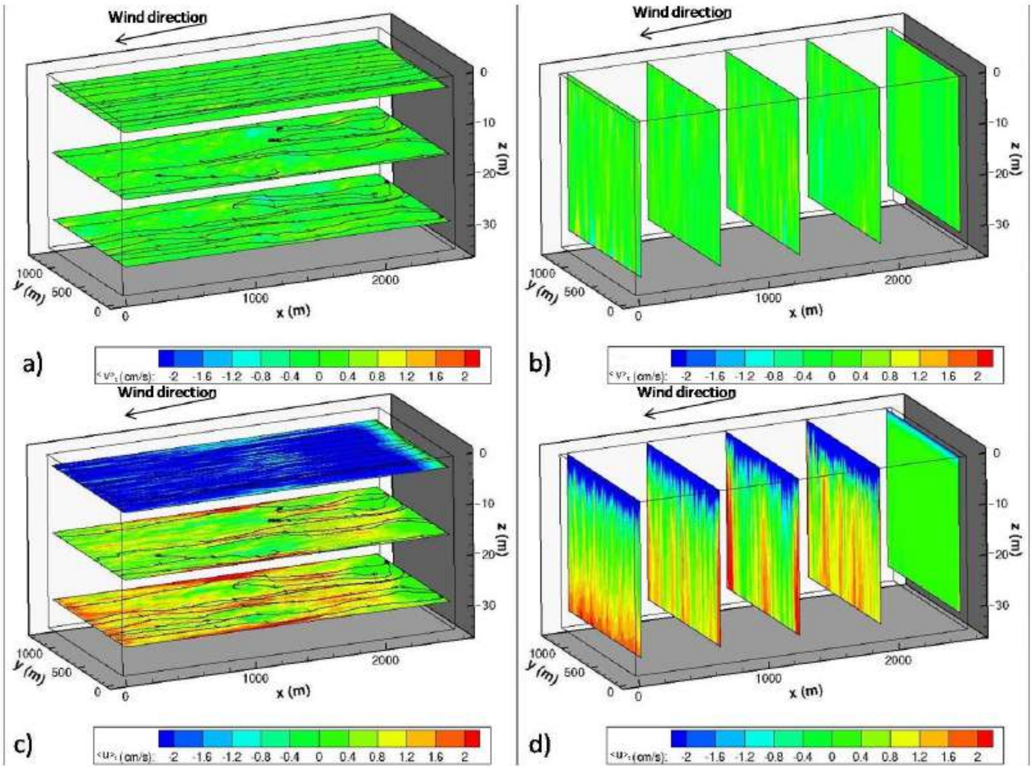

Figure 4.1: HSWC in absence of Coriolis force. Snapshot of the streamtracers and of the horizontal velocity field averaged over 6 hours at the steady state with $U_{10} = 4m/s$: velocity v (a,b) and u (c,d) at different horizontal planes and transects.

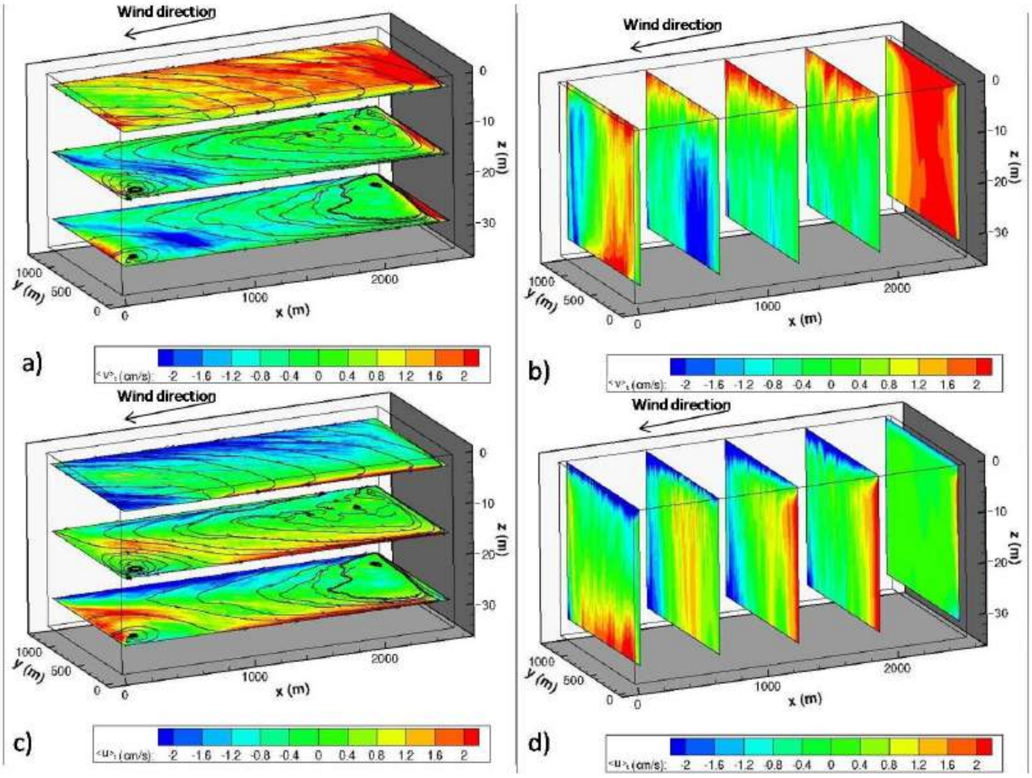

Figure 4.2: HSWC with Coriolis force. Snapshot of the streamtracers and of the horizontal velocity field averaged over 6 hours at the steady state with U_{10} = $4m/s$: velocity v (a,b) and u (c,d) at different horizontal planes and transects.

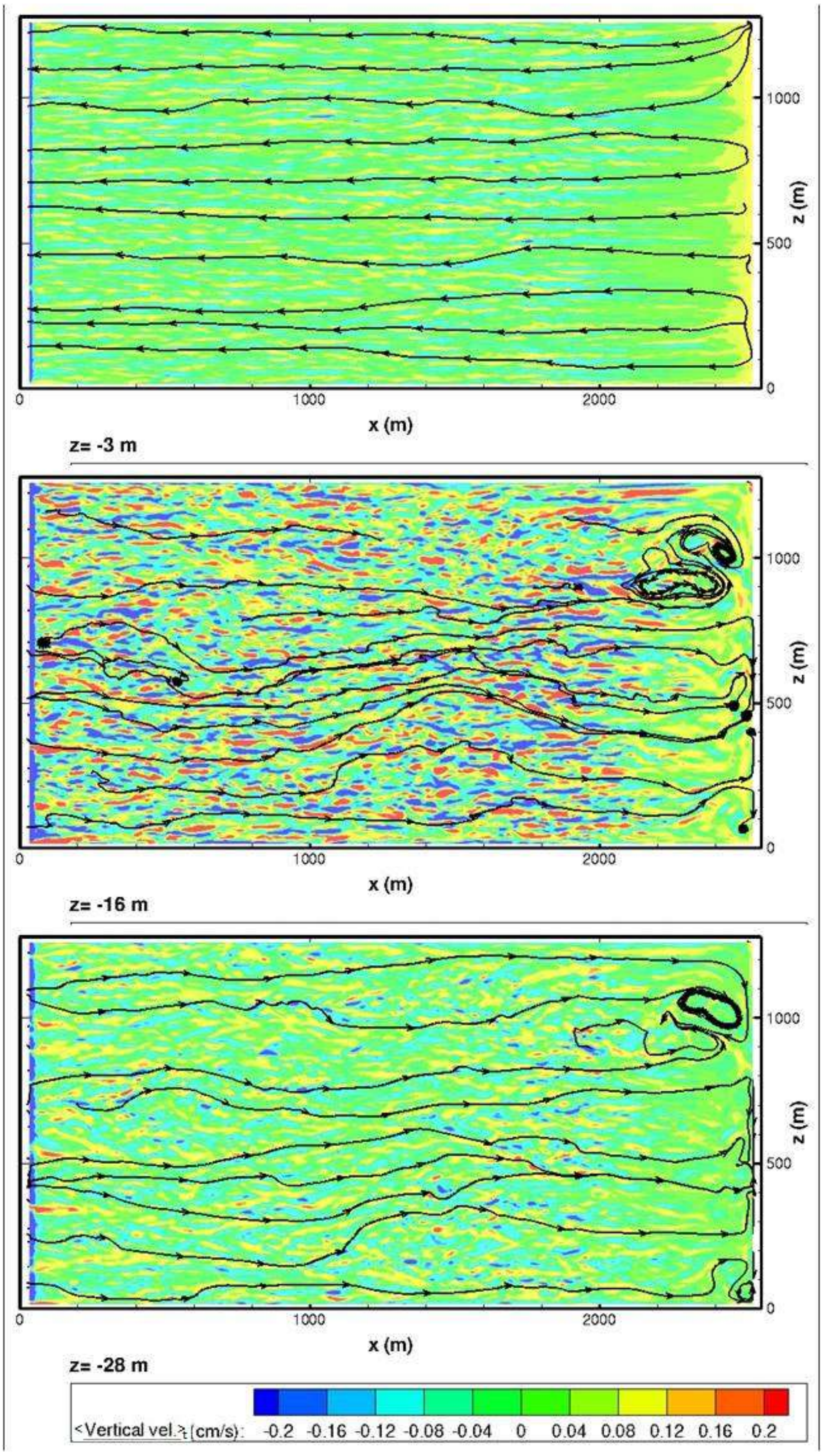

Figure 4.3: HSWC in absence of Coriolis force. Snapshot of the streamtracers and of the vertical velocity field averaged over 6 hours at steady state with $U_{10} = 4m/s$ at different horizontal planes.

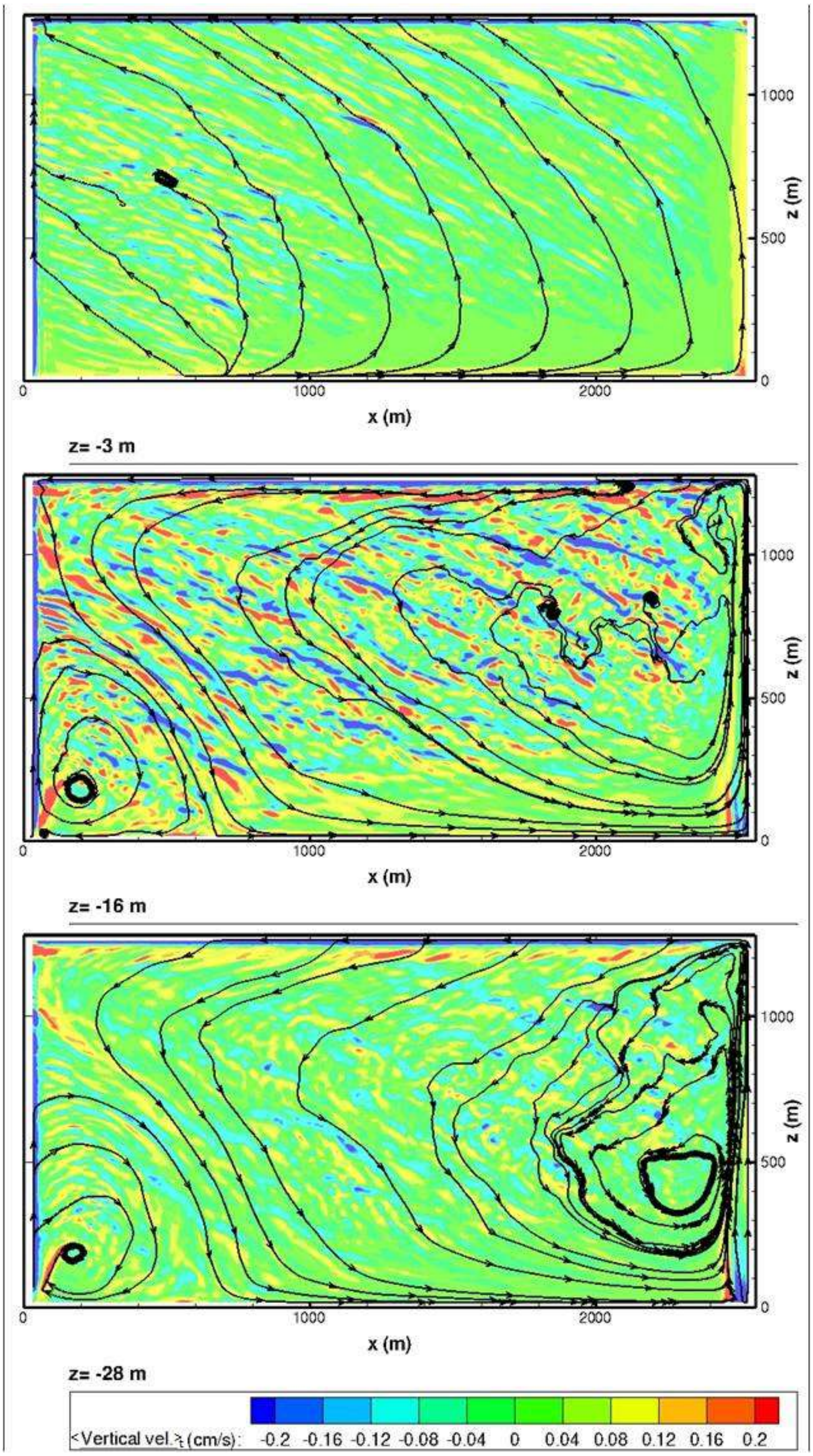

Figure 4.4: HSWC with Coriolis force. Snapshot of the streamtracers and of the vertical velocity field averaged over 6 hours at steady state with $U_{10} = 4m/s$ at different horizontal planes.

As a representative example of the wind-driven circulation occurring in a such simplified domain 6-hour average snapshots of the horizontal velocity field were extracted after simulation time of three days (i.e. when the flow has reached the steady state). Figure 4.1 shows the horizontal components of velocity and streamtracers at different horizontal planes and transects in absence of Coriolis force. For simplicity the wind direction is taken as the direction of reference. The $\langle v \rangle_t$ velocity is mostly equal to zero in the whole domain, meanwhile $\langle u \rangle_t$ is aligned with the wind direction in the top 5 meters. Specifically, by looking at the vertical profile of the streamwise velocity shown in Fig. 4.5a it is possible to appreciate how $\langle u \rangle_t$ inverts its direction below 10 m depth. This indicates the presence of a return flow in the interior of the domain and thus the presence of downwelling and upwelling areas along the leeward and windward sides, respectively. In Fig. 4.3 the contour plots of the vertical velocity at three different planes in absence of Coriolis force are shown, where the downwelling areas (blue color) and upwellig areas (red color) are depicted along the leeward and windward side, respectively.

Dimensional analysis suggests that despite the dimension of the lake being small, the Rossby number $Ro = U/(Lf)$ is of the order of 0.05 (hence $<< 1$), due to the small horizontal velocity scales present in the lake ($U \sim 10^{-2}$ $\mathrm{m\,s^{-1}}$, $L = 2000$ m and $f = 2\Omega_3 sen\ \theta = 10^{-4}$ $\mathrm{s^{-1}}$, where θ is the latitude). In Fig. 4.2 is possible to appreciate the effect of the Coriolis force on the wind-driven currents of a such simplified domain. Unlike the aforementioned case $\langle v \rangle_t$ is no more equal to zero and the velocity field is not homogeneous on the horizontal planes. Also, the horizontal velocity at the free surface is tilted to the right with respect to the wind direction. Specifically, $\langle u \rangle_t$ has the same direction of the wind (blue color in Fig. 4.2c,d) along the right half-side at the surface layer and along the right wall; whereas the velocity has an opposite direction (red color in Fig. 4.2c,d) at the bottom downwind side and along the left wall. This gives rise to upwelling and downwelling areas along the windward/rightward and leeward/leftward side of the domain (see Fig. 4.4). A recirculation area is developed at the bottom left corner of the windward side giving rise to higher velocities around it. Furthermore, the inversion of circulation occurs between 5 m and 10 m depth (Fig. 4.5).

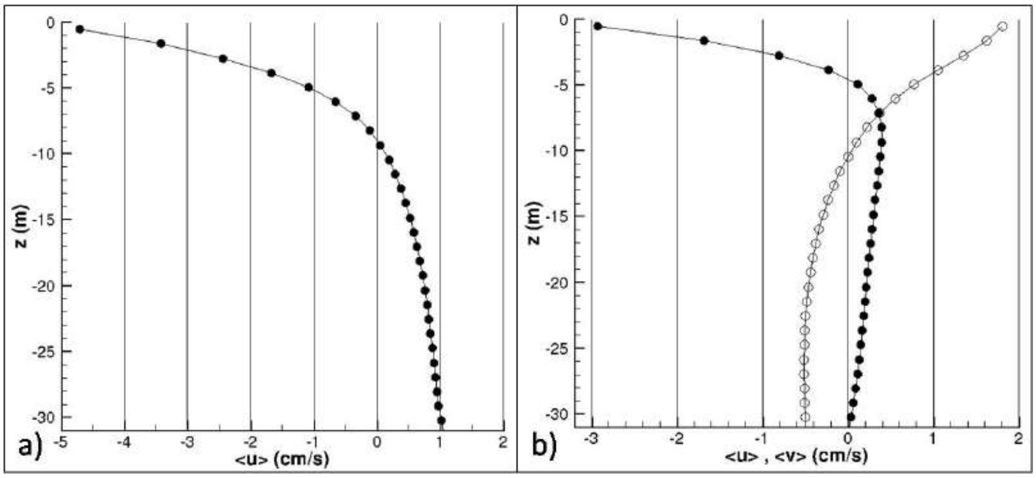

Figure 4.5: Vertical profiles of space-time $\langle u \rangle$ ($\bullet$) and $\langle v \rangle$ ($\circ$) averaged over 2 hours at steady state a) without Coriolis force and b) in presence of Coriolis force.

The central part of the domain is characterized by marked differences in vertical and horizontal velocities (Fig. 4.3, 4.4), similar to stripes, suggesting the presence of wind-generated turbulent structures, as already detected in other LES applications (Petronio et al., 2013; Galea at al., 2014), and observed in physical experiments for shallow-water wall-bounded turbulence (V. Nikora, 2015, private communication). These superstreaks consist of rotating vortices with the axis approximately aligned with the direction of the motion and resemble the Couette streaks first presented in Lee and Kim (1991) and Papavassiliou and Hanratty (1997). The turbulent structures have the same characteristics as the ones shown in Tejada-Martinez and Grosch (2007) in their case without the vortex force which is representative of the interaction between the Stokes drift and the shear current. In Galea at al. (2014) these structures were shown to span over a length of tens of meters in the streamwise direction and to persist for hours. These circulations enhance vertical mixing along the water column.

4.2 Eddy Viscosity with Different Geometries

Turbulent transport of momentum in lakes is expected to occur at a much larger rate in the horizontal direction, possibly affecting the general circulation (Toffolon and Rizzi, 2009). This turbulence anisotropy is partly due to the effect of the relative shallowness of these water bodies, and partly due to the effect of stratification.

Down-gradient turbulent transport is usually quantified through the vertical and horizontal eddy viscosity coefficients. The concept of eddy viscosity is based on the gradient-diffusion hypothesis which assumes the anisotropic Reynolds stress tensor be aligned with the mean rate of the strain tensor Eq. (2.7). Although such an assumption is somehow crude (Kundu, 2012), it is generally accepted in the scientific and engineering communities.

The vertical and horizontal eddy viscosities are expressed respectively as:

$$\nu_H = \frac{\sqrt{\widetilde{u'v'}^2}}{\sqrt{(\frac{\partial \tilde{u}}{\partial y} + \frac{\partial \tilde{v}}{\partial x})^2}} + \nu_{\tau,H} \,, \tag{4.1}$$

$$\nu_V = \frac{\sqrt{\widetilde{u'w'}^2 + \widetilde{v'w'}^2}}{\sqrt{(\frac{\partial \tilde{u}}{\partial z})^2 + (\frac{\partial \tilde{v}}{\partial z})^2}} + \nu_{\tau,V} \,, \tag{4.2}$$

where $\nu_{\tau,H}$ and $\nu_{\tau,V}$ are respectively the SGS contributions of Eqs. 2.15 2.14.

Note that here the eddy viscosities have been calculated by using the Reynolds stresses and velocity gradients obtained in an operation of post-processing by averaging the data of our eddy resolving simulation. Standard models often use parametrization of eddy viscosity based on theory and calibration obtained for open ocean under steady or quasi-steady forcing. However, the dynamics of a small lake under a diurnal cycle of thermally-driven winds may be substantially different from the former simplified conditions. Thus, in the next Section is analized the spatial distribution of the eddy viscosity with a spatially homogeneous steady wind with and without Coriolis force in three cases: an (infinite) ocean, a simplified rectangular domain and in Lake Ledro.

Hereafter is discussed the vertical profile of vertical eddy viscosity calcu-

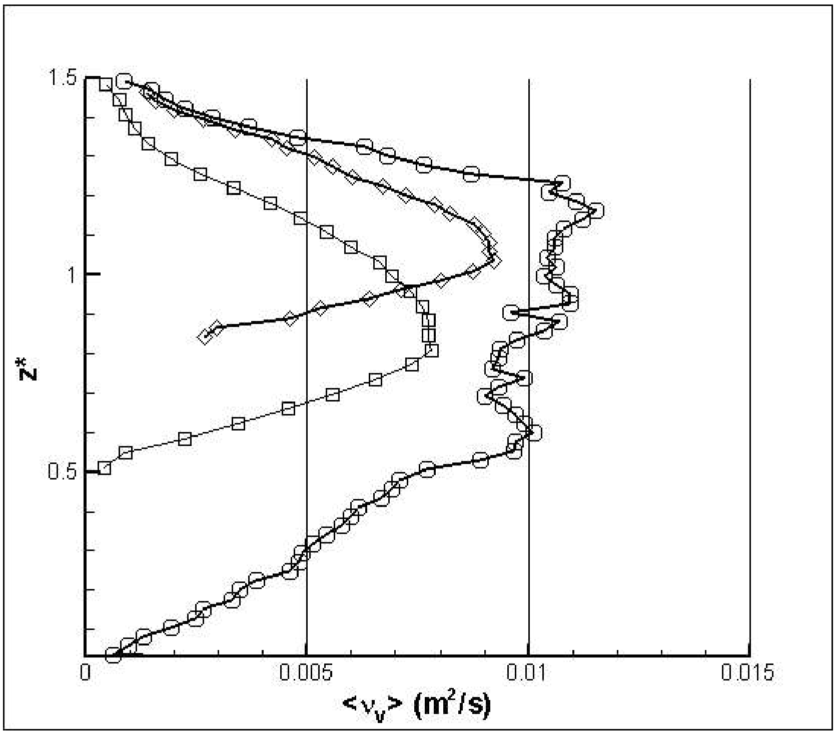

Figure 4.6: HSWC. Vertical profile of vertical eddy viscosity $\langle\nu_V\rangle$ in presence of Coriolis force obtained in three cases: for an unbounded turbulent Ekman layer (○); for the simplified rectangular domain (⋄) and for Lake Ledro (□) under steady wind. Unlike the rest of the thesis, here the free surface is at $z^* = 1.5$.

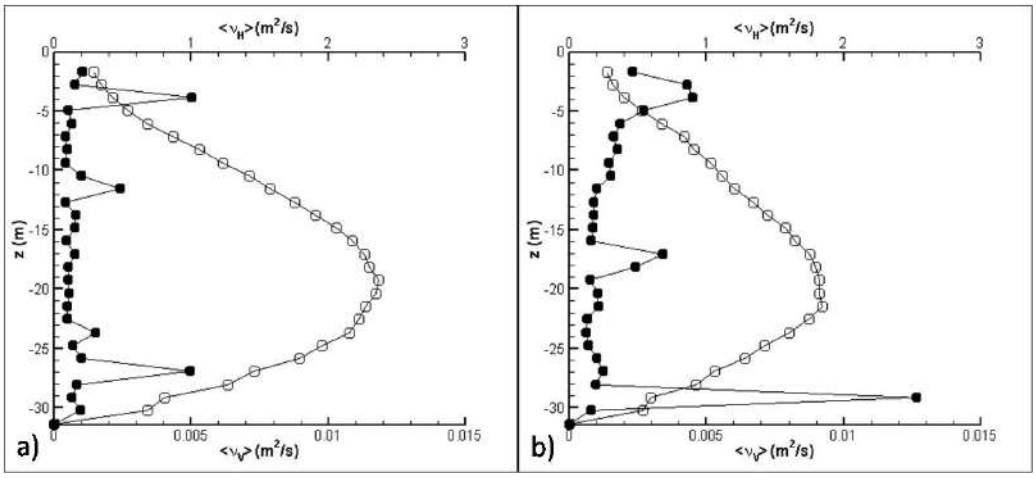

Figure 4.7: HSWC. Vertical profile of 2-hour average vertical eddy viscosity $\langle \nu_V \rangle$ (○) and horizontal eddy viscosity $\langle \nu_H \rangle$ (•) obtained in the rectangular domain : a) simulation without Coriolis force; b) simulation with Coriolis force.

lated with Eq. 4.2 in view of the results obtained in (Zikanov et al., 2003) for a LES of an infinite Reynolds number surface Ekman layer. Then is analized the effect of Earth's rotation and of solid boundaries on the spatial distribution of eddy viscosities.

The conditions for the development of an oceanic Ekman layer at $Re_E = u^*/\sqrt{f\,\nu}$ = with $u^* = \sqrt{\tau_w/\rho}$ has been reproduced. The vertical profile of $\langle \nu_V \rangle$, averaged over a time window of 2 hours (Fig. 4.6) qualitatively agrees with that of Zikanov et al. (2003). Specifically, in the surface layer the vertical eddy viscosity increases linearly with depth reaching its maximum at around $z* = z/L = 1.25$, where $L = u^*/f$ is the turbulent length scale. The eddy viscosity profiles obtained by Zikanov et al. (2003) were generated in presence of a steady wind; note that in the case of Lake Ledro, a fully developed steady flow condition would be reached after six days of constant unidirectional wind blowing over at the free surface. This condition is not reached in small-and medium-size lakes for two main reasons: the rapid change of the wind direction and intensity does not allow for reaching a steady state; the presence of lateral boundaries generates a circulation in the cross-sections orthogonal to the wind direction (Toffolon, 2013).

In order to highlight the role of the boundaries, the eddy viscosity profiles developed both within the simplified domain and within Lake Ledro in presence of Coriolis force are analized. The wind utilized is an easterly homogeneous and constant wind blowing at $U_{10} = 4$ ms^{-1}. Figure 4.6 also shows the vertical profiles of eddy viscosity obtained in simplified domain and in Lake Ledro in presence of the Coriolis force. In the surface boundary layer the vertical eddy viscosity in the bounded simplified domain increases at the same rate than in the unbounded case. This is no true for the domain reproducing the actual geometry and bathymetry of Lake Ledro where the $\langle \nu_V \rangle$ is mostly constant in the surface layer and then increases at a smaller rate with respect to the oceanic case reaching its maximum in the interior of the lake.

In Fig. 4.7 is possible to appreciate the effect of the Coriolis force on the vertical profile of the eddy viscosities computed in the simplified rectangular domain: the Coriolis force causes the reduction of the vertical eddy viscosity due to the stabilization effect of the Coriolis force on the turbulence intensity (see Barri and Andersson (2010) for a discussion). The orizzontal eddy viscosity is characterized by spikes due to the too short time average considered for computing the stress at the numerator of 4.1. The same analysis has been conducted for the domain reproducing the actual geometry and bathymetry of Lake Ledro: also in this case the Coriolis force causes a reduction of the shear stress (Fig. 4.8c,d,e,f), thus producing lower values of both vertical and horizontal eddy viscosities. Overall, the analysis of the eddy viscosities confirms that a marked anisotropy exists in Lake Ledro even for non-stratified conditions herein studied.

4.3 Turbulent Kinetic Energy and TKE Dissipation Rate

The Turbulent Kinetic Energy (TKE) is a measure of the intensity of velocity fluctuations within the water body:

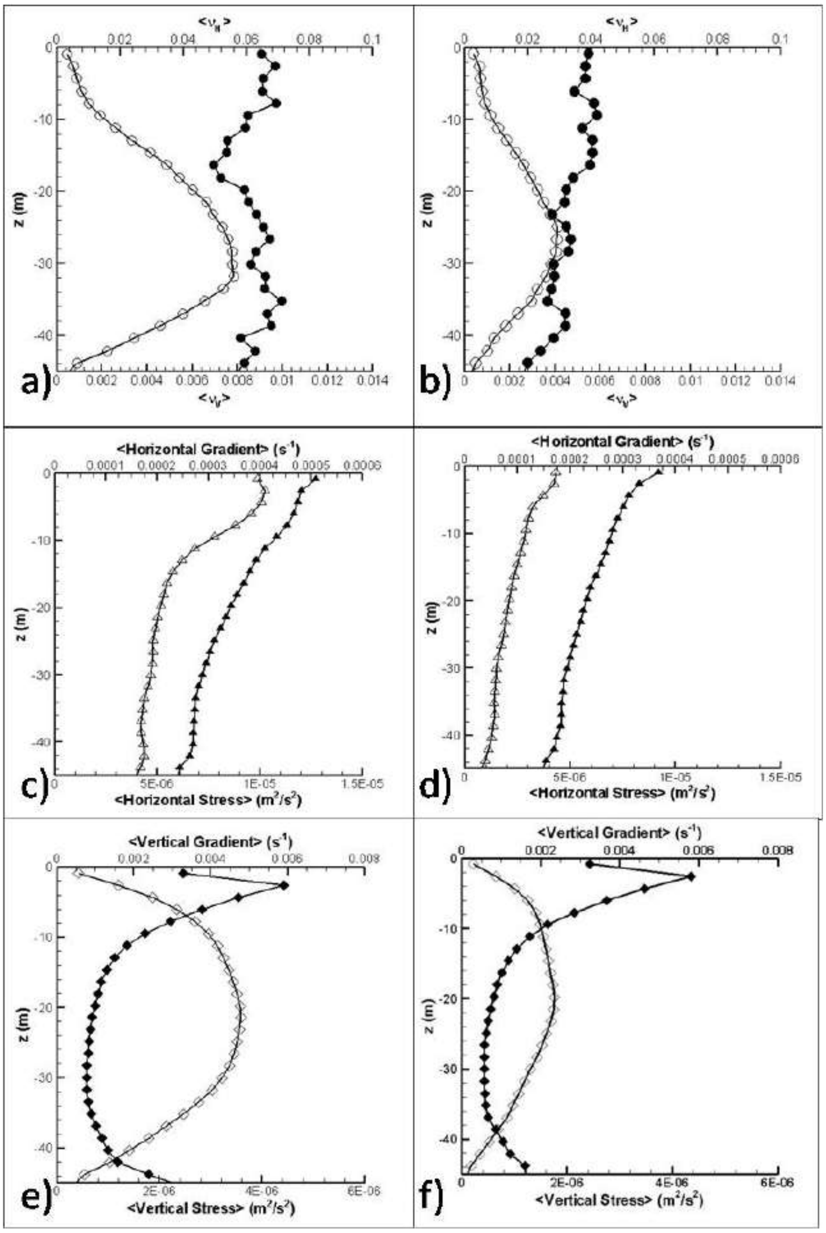

Figure 4.8: HSWC. Vertical profiles of horizontally averaged quantities obtained in Lake Ledro (2-hour average at steady state): (a,b) vertical eddy viscosity $\langle \nu_V \rangle$ (○) and horizontal eddy viscosity $\langle \nu_H \rangle$ (•); (c,d) horizontal stresses (△) and horizontal gradients (▲) along x axes, horizontal stresses (▽) and horizontal gradients (▼) along y axes; (e,f) vertical stress along z axis (◇) and vertical gradients along z axis(◆). Stresses and gradients correspond respectively to numerator and denominator in Eqs. 4.2 and 4.1. The quantities shown in the right column (b,d,f) are calculated in presence of Coriolis force, conversely the quantity on the left column (a,c,e) are calculated in absence of Coriolis force.

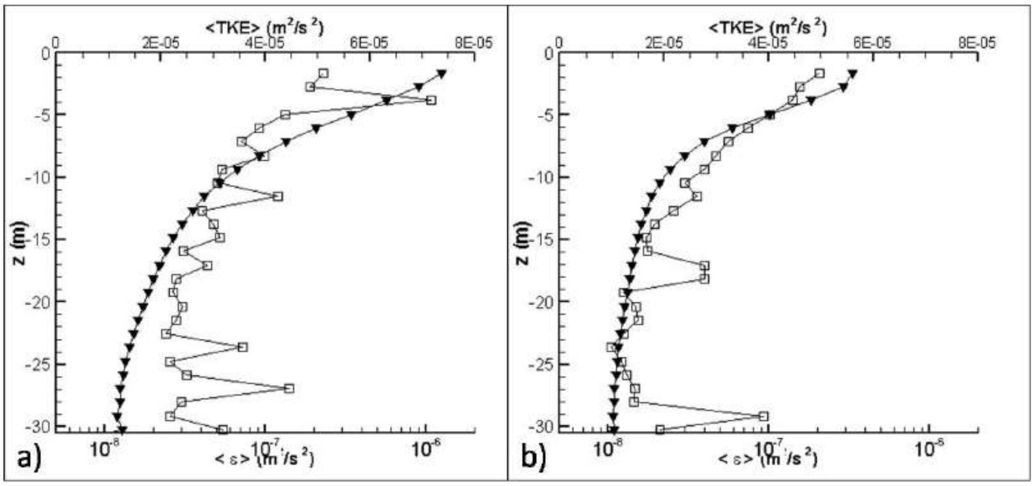

Figure 4.9: HSWC. Vertical profile of the space-time $\langle \epsilon \rangle$ ($\square$) and $\langle TKE \rangle$ ($\blacktriangledown$) averaged over 2 hours at the steady state: a) with Coriolis force and b) without Coriolis force.

$$\widetilde{TKE} = \frac{1}{2}(\widetilde{u'u'} + \widetilde{v'v'} + \widetilde{w'w'}) \tag{4.3}$$

It is mainly confined in the resolved scales and the SGS contribution is generally low. The resolved-scale dissipation rate of TKE is:

$$\widetilde{\epsilon_r} = -2\nu\, \widetilde{s_{ij}s_{ij}}\,, \qquad s_{ij} = \frac{1}{2}\left(\frac{\partial u_i{}'}{\partial x_j} + \frac{\partial u_j{}'}{\partial x_i}\right). \tag{4.4}$$

However, since most of the dissipative scales of motion are confined in the subgrid, the total ϵ was estimated adding to ϵ_r the rate of energy transferred from the filtered motion to the residual one ($P_{SGS} \equiv -\tau_{ij}S_{ij}$), which is equal to the SGS dissipation rate ϵ_{SGS} of the turbulent energy for high Reynolds numbers (Pope, 2000). According to the eddy viscosity model of Eq. 2.7,

$$\widetilde{\epsilon_{SGS}} = \widetilde{P_{SGS}} = -\widetilde{\tau_{ij}}\widetilde{S}_{ij} = 2\widetilde{\nu_\tau}\widetilde{S}_{ij}\widetilde{S}_{ij}\,, \tag{4.5}$$

hence,

$$\widetilde{P_{SGS}} = 2\widetilde{\nu}_{\tau,H}(\widetilde{S}_{11}^2 + 2\widetilde{S}_{22}^2 + \widetilde{S}_{12}^2) + 2\widetilde{\nu}_{\tau,V}(2\widetilde{S}_{13}^2 + \widetilde{S}_{33}^2 + 2\widetilde{S}_{23}^2). \tag{4.6}$$

The total dissipation rate of TKE is expressed as $\widetilde{\epsilon} = \widetilde{\epsilon_r} + \widetilde{\epsilon_{SGS}}$.

The vertical profiles of $\langle TKE \rangle$ and $\langle \epsilon \rangle$, averaged over 2 hours after having reached the steady state, in presence and in absence of Coriolis force were calculated and reported in Fig. 4.9. High values of $\langle TKE \rangle$ are observed close to the free surface and small values are detected at the bottom. This is an evidence of the fact that the wind is the main source of turbulence. The averaged dissipation rate of TKE ranges between 10^{-8} W kg^{-1} and 10^{-6} W kg^{-1}; it has the maximum in the Surface Boundary Layer (SBL), decreases exponentially with the depth in the top 15 m and reaches the minimum value at the bottom of the domain, in both cases the values of $\langle \epsilon \rangle$ are in qualitative agreement with measurements obtained in other lakes Wuest et al. (2000).

Chapter 5

HOMOGENEOUS WIND FIELD

5.1 The Velocity Field

In order to estimate the wind-driven circulation in Lake Ledro produced by a cyclic wind, the effect of the wind cycle shown in Fig. 3.1a uniformly applied to the entire lake surface has been simulated.

As a representative example of the circulation occurring during the winter period, snapshots were taken at 13:00 of 20 January 2012, when the wind direction is 135° and the speed $\sim 5\ \mathrm{m\,s^{-1}}$ for 4 hours. This instantaneous velocity field is representative of the time period around the early afternoon when wind usually blows from south-east with the same intensity as of 13:00 of 20 January. The wind acting on the surface of the lake during this period is depicted in Fig.5.1a.

The vertical and horizontal instantaneous velocity components and streamlines 2.5 m below the free surface are shown in Fig. 5.2, together with vertical transects along the axes AB and CD defined in Fig. 1.1b. The streamlines indicate the presence of upwelling and downwelling areas along the windward and leeward shoreline of the lake, respectively (Fig. 5.2a). The vertical velocity in the upwelling region is of the order of $1 \times 10^{-3}\ \mathrm{m\,s^{-1}}$ for about 6 hours in the central part of the day. This gives an estimation of uprising of

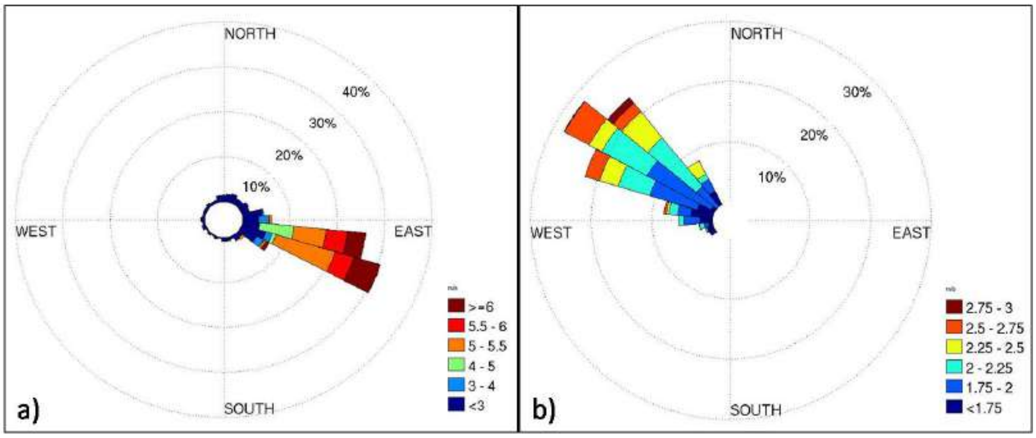

Figure 5.1: Wind rose related to the wind acting on the lake surface (m/s): a) between 11:00 and 13:00 of the 20^{th} of January; b) during the morning (00:00 - 08:00) of the 16^{th} of January.

the order of 21 meters, hence providing a physical explanation for the sudden rising of the *P. rubescens* cyanobacteria along the coasts of Lake Ledro.

The horizontal velocity is relatively low along the leeward side of the coastline in the downwelling areas (north-western coasts, see Fig. 5.2b). The horizontal velocity in the lake interior (below 15 m of depth) is opposite to the circulation in the surface layer (Fig. 5.2c), indicating the typical presence of a return flow and hence of a vertical circulation. The return flow is better appreciable when the wind holds the direction for a long time.

Figure 5.3 shows the vertical profiles of the horizontal velocity components (averaged on the horizontal plane and in time, one hour) in the morning of the second day (between 00:00 and 01:00 of 17 January). In this case the wind has been blowing from north-west for 4 hours with the same strength (~ 1.7 m s^{-1}) and the inversion occurs at ~ 8 m. In the case of turning wind it is hard to establish a fixed depth where the horizontal velocities change direction because it evolves depending on the wind.

The typical wind driven circulation generated during the morning, shown in Fig. 5.4a, is different from the circulation generated during the afternoon because of the different direction and intensity of the wind acting on the surface: it blows from north-west at ~ 2 m s^{-1} (Fig.5.1b). The streamlines depicted in Fig. 5.4a are tilted with respect to the wind direction because of the

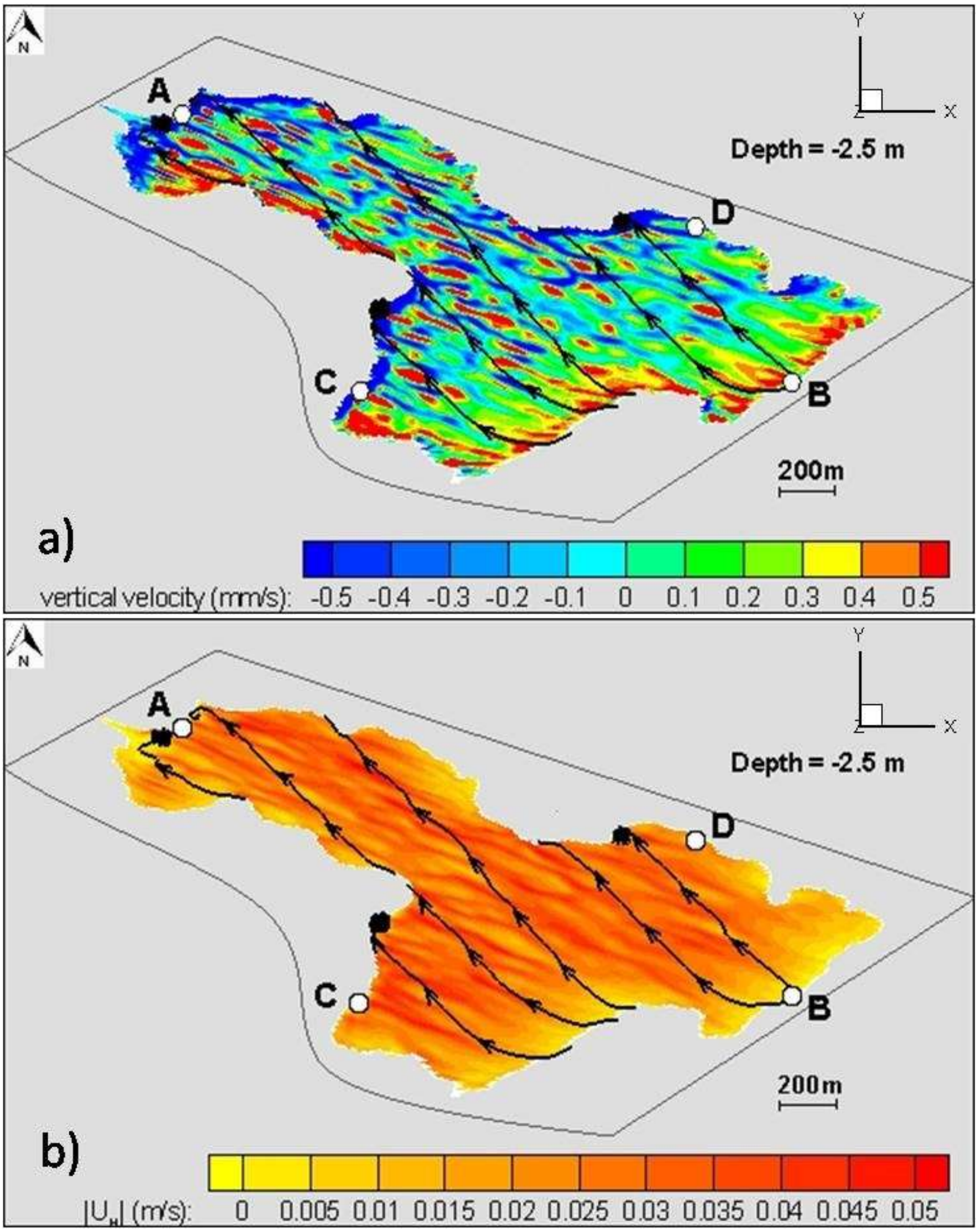

Figure 5.2: continue

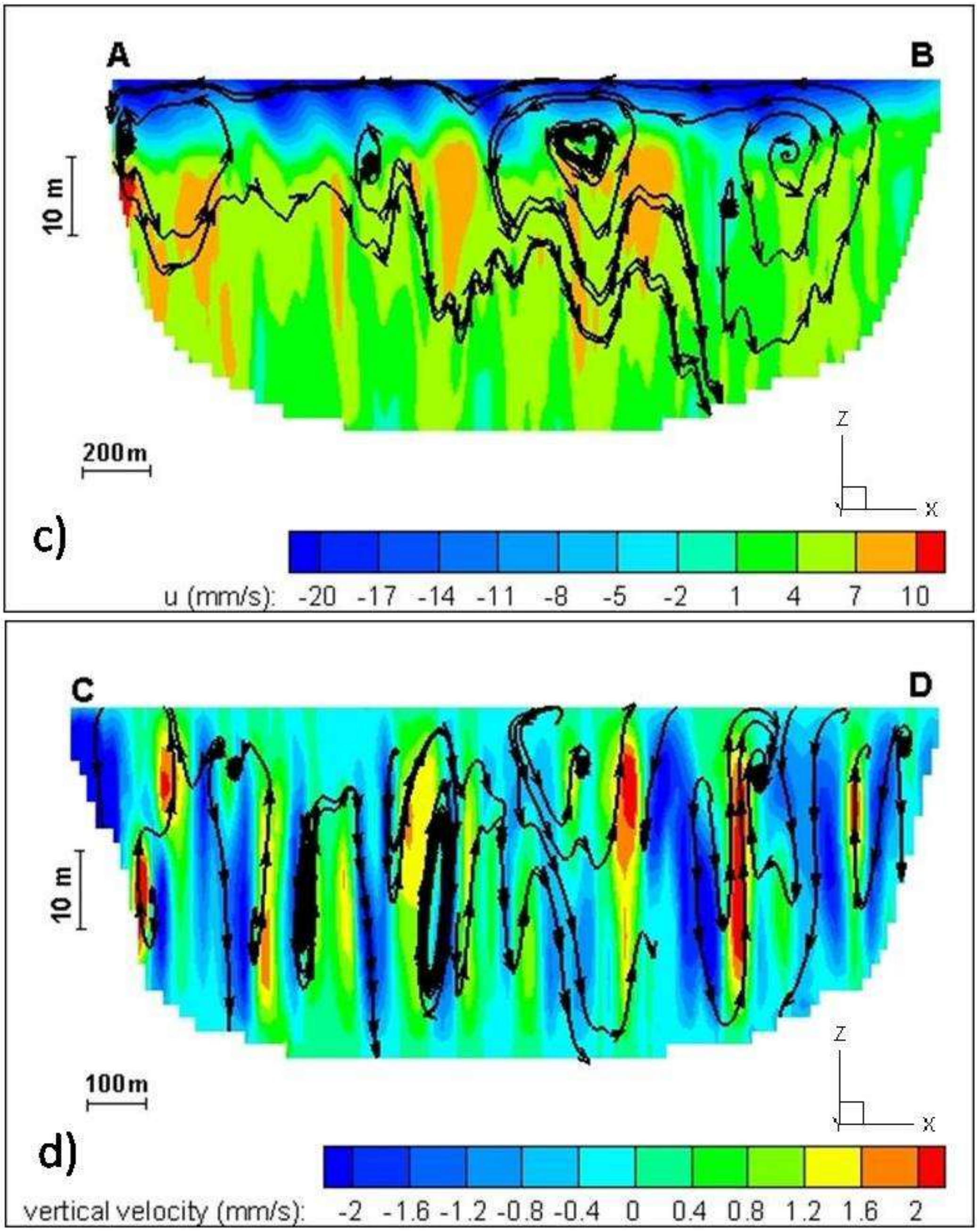

Figure 5.2: HWC. Snapshot of the streamtracers and instantaneous field at 13:00 of 20 January: a) vertical, and b) horizontal ($|U_h|$) velocity, on a horizontal plane at 2.5 m depth; c) u in transect AB and d) w in transect CD

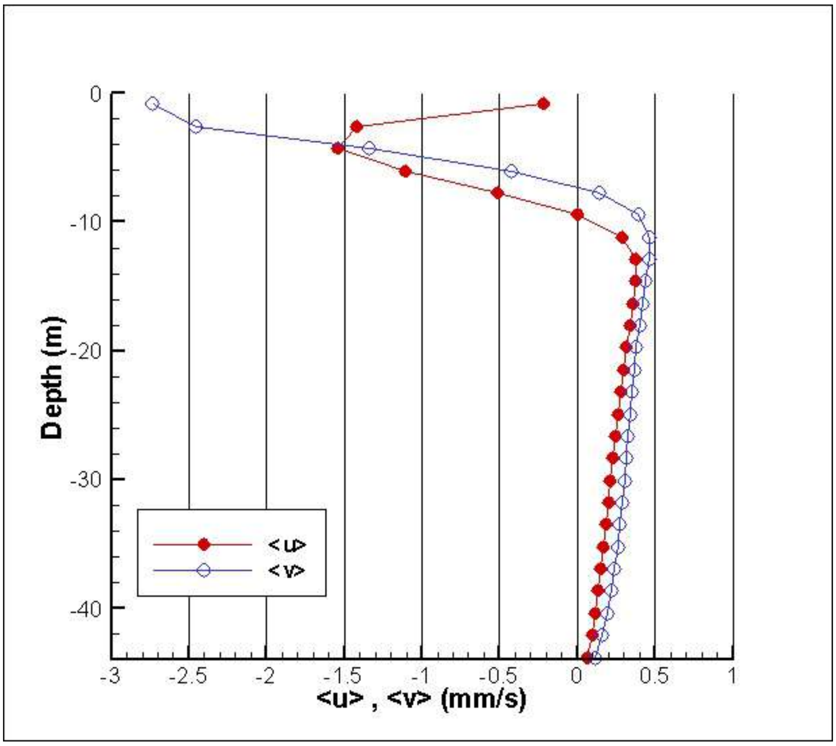

Figure 5.3: HWC. Vertical profile of the space-time $\langle u \rangle$ ($\bullet$) and $\langle v \rangle$ (solid line with $\circ$) averaged over 1 hour between 00:00 and 01:00 of 17 January.

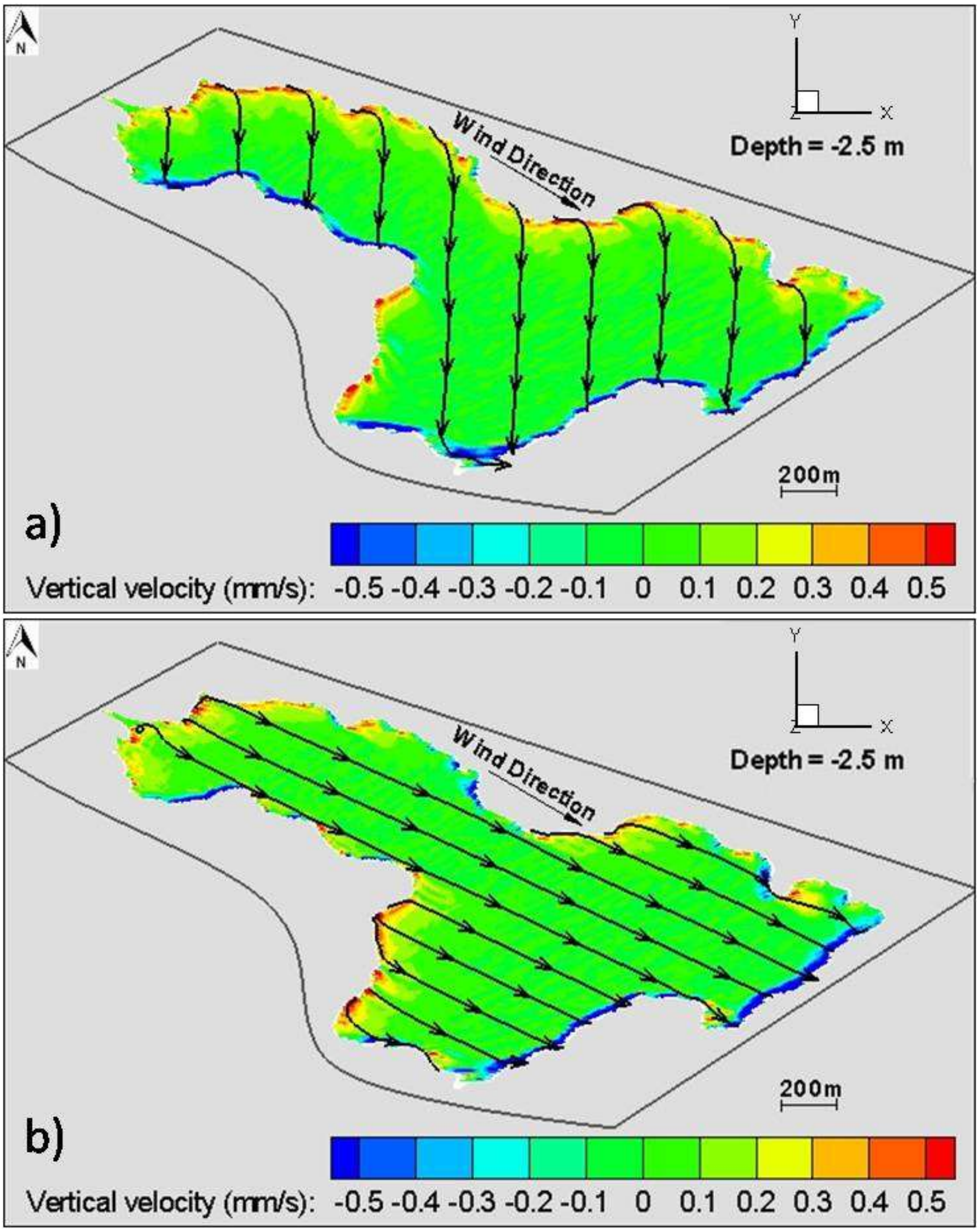

Figure 5.4: HWC. Snapshot of the results of the simulation with homogeneous wind field at 08:00 of 16 January when the wind blows from north-west at ~ 2m/ s^{-1}, as shown in Fig5.1b, with the contribution of the Coriolis Force (a) and without the contribution of the Coriolis force (b).

Coriolis effect. This has been verified repeating the simulation without the contribution of the Coriolis force and observing that, in the latter case, the instantaneous streamlines are aligned with the wind direction (Fig. 5.4b). Also in this case the Rossby number is of the order of $0.05 << 1$ ($Ro = U_H/(Lf)$, with $U_H = 0.01$ m s^{-1}, $L = 2000$ m and $f = 10^{-4}$ s^{-1}). Hence rotational effects may have a role both in the deviation of the velocity vectors and in the suppression of vertical mixing (see Salon and Armenio (2011) for a discussion). Moreover, Toffolon (2013) showed that Coriolis force in narrow lakes can produce a secondary circulation (in the vertical plane orthogonal to the wind direction) with a resulting Ekman transport and downwelling/upwelling at the coast. The Coriolis force is weak during the afternoon when the horizontal velocity present in the lake is ~ 0.05 m s^{-1} giving a Rossby number ~ 0.25.

5.2 Spatial Distribution of Eddy Viscosity with Time-Varying Wind

Contour plots of $\langle \nu_V \rangle_t$ and $\langle \nu_H \rangle_t$ are shown in Fig. 5.5. They were calculated over a time window of 8 hours between 00:00 and 08:00 of the second day, under the wind condition measured at the meteorological station. Panels a and b show respectively the distribution of the two quantities over the vertical plane in the transect AB of Fig. 1.1. Panels c and d show the distribution of the two quantities over horizontal planes at $z = -7.7$ m and $z = -16.3$ m.

The eddy viscosities are strongly anisotropic, with the horizontal coefficient being about 2 orders of magnitude larger than the vertical one even in the neutral conditions herein investigated. In the SBL, the horizontal eddy viscosity $\langle \nu_H \rangle_t$ (Fig. 5.5a) decreases with depth up to $z \sim -16$ m, then it grows reaching a maximum at $z \sim -40$ m. The vertical eddy viscosity $\langle \nu_V \rangle_t$ (Fig. 5.5b) is very small at the surface and it increases in the SBL reaching its maximum at $z \sim -28$ m.

Interestingly, the two quantities exhibit substantial inhomogeneity along the horizontal planes. In the lake interior the horizontal eddy viscosity $\langle \nu_H \rangle_t$

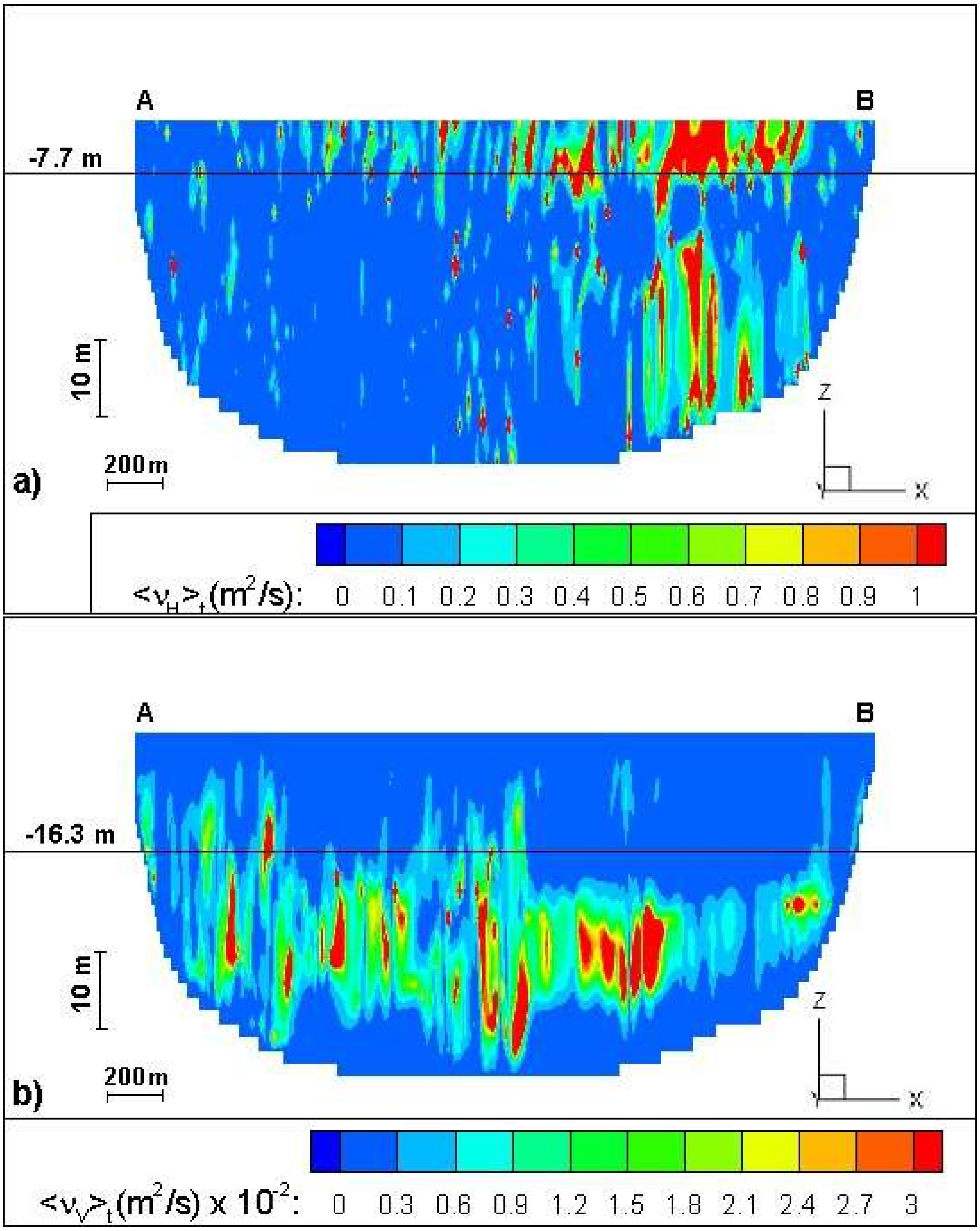

Figure 5.5: continue

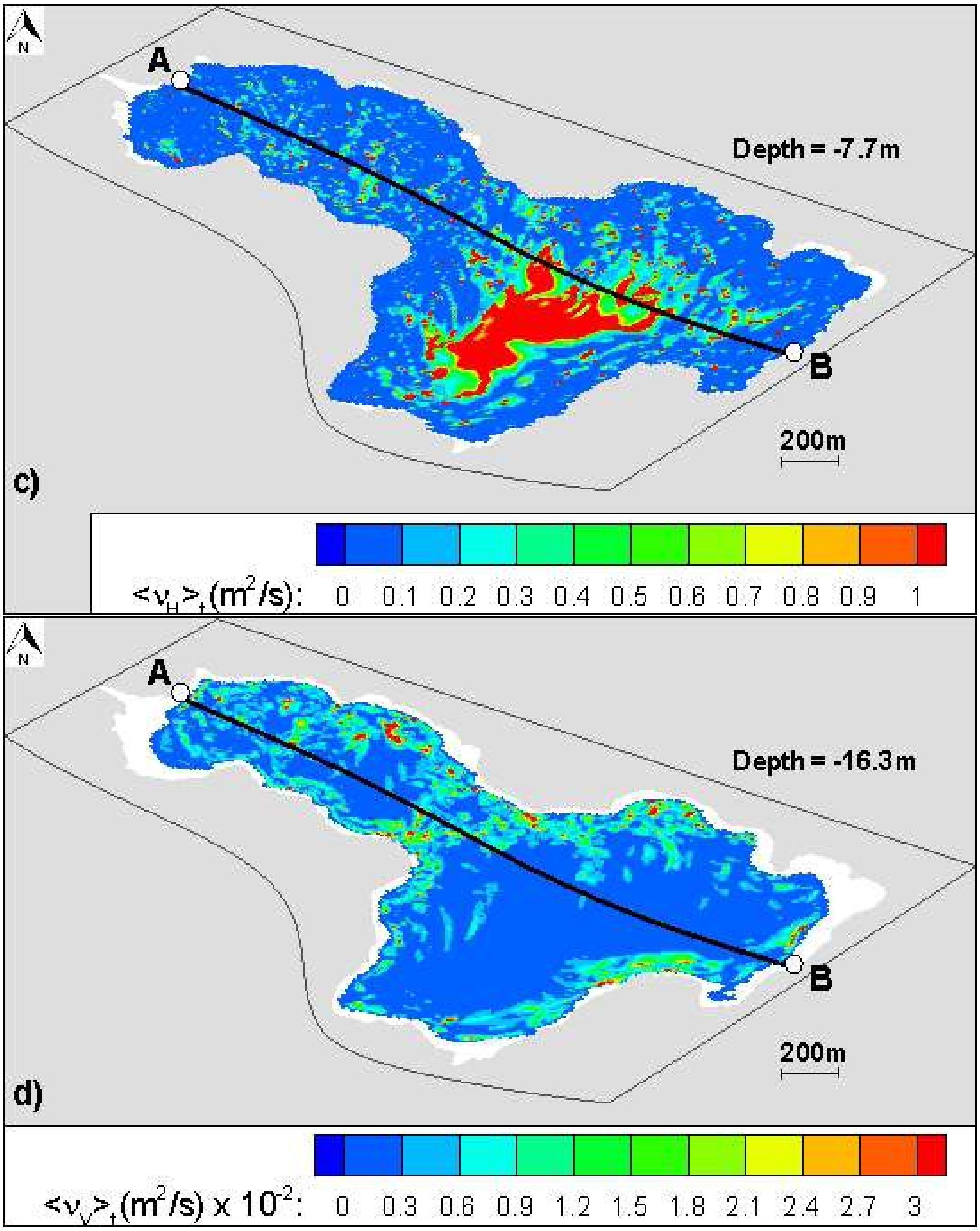

Figure 5.5: HWC. Eddy viscosities obtained averaging over 8-hour between 00:00 and 08:00 of 17 January. Contour plots of: a) $\langle \nu_H \rangle_t$ over the transect AB of Fig. 1.1a; b) $\langle \nu_V \rangle_t$ over the transect AB of Fig. 1.1a; c) $\langle \nu_H \rangle_t$ on a horizontal plane at $z = -7.7$ m; d) $\langle \nu_V \rangle_t$ on a horizontal plane at $z = -16.3$ m.

is much larger far from the coastline (Fig. 5.5c) where the values of the horizontal velocity gradients are smaller. Conversely, the vertical eddy viscosity $\langle \nu_V \rangle_t$ is larger along the shoreline, due to the presence of the boundary layers associated to upwelling and downwelling regions, with high values of the Reynolds shear stresses ($\langle u'w' \rangle_t$ and $\langle v'w' \rangle_t$).

Figure 5.6a reports the vertical profiles of the space-time averaged values of $\langle \nu_H \rangle$ and $\langle \nu_V \rangle$. Differently from those shown in Fig. 4.8, here the quantities are obtained over the time window of 8 hours as described above. Unlike the case with the steady mean wind where $\langle \nu_H \rangle$ remains constant along the depth , in this case it is roughly constant down for the first 5 m and then it decreases reaching its minimum value at around $z = -15$ m, due to a rapid reduction of the Reynolds shear stresses (Fig. 5.6b) showing the presence of a minimum-stress plane. The vertical eddy viscosity $\langle \nu_V \rangle$ increases with the distance from the free surface down to $z \sim$ -30 m similarly to the case shown in Fig. 4.6. For larger depths, $\langle \nu_V \rangle$ first increases rapidly because of the decrease of the vertical gradients of the horizontal velocities and successively decreases due to the rapid decrease of the Reynolds shear stress (Fig. 5.6c). The behavior of the vertical eddy viscosity in the bottom region is representative of the weakness of the bottom boundary layer as will be discussed later.

Finally in Fig. 5.7 we show the space-time averaged eddy viscosities $\langle \nu_V \rangle$ and $\langle \nu_H \rangle$ along the six days simulated. The evolution of the flow starting from the quiescent state takes approximately 1 day; for this reason the first day of simulation is not discussed. The quantity $\langle \nu_V \rangle$ is always at its climax in the core of the water basin, and its intensity is modulated according to the wind stress. The maximum of the horizontal eddy viscosity $\langle \nu_H \rangle$ is close to the free surface and large values of this quantity propagate up to the deep layers in case of large wind stress. Moreover, in order to quantify the vertical and horizontal eddy viscosity associated to a certain intensity of wind stress, these quantities have been made non dimensional with $u^* H$, where $u^* = \sqrt{\tau_w / \rho}$ is a velocity scale representative of the wind intensity and H is an inertial length scale (the mean depth of the lake), and shown in Fig 5.8. The evolution in time of the vertical profile of the two non dimensional quantities will be used in the next Chapter in order to evaluate the role of

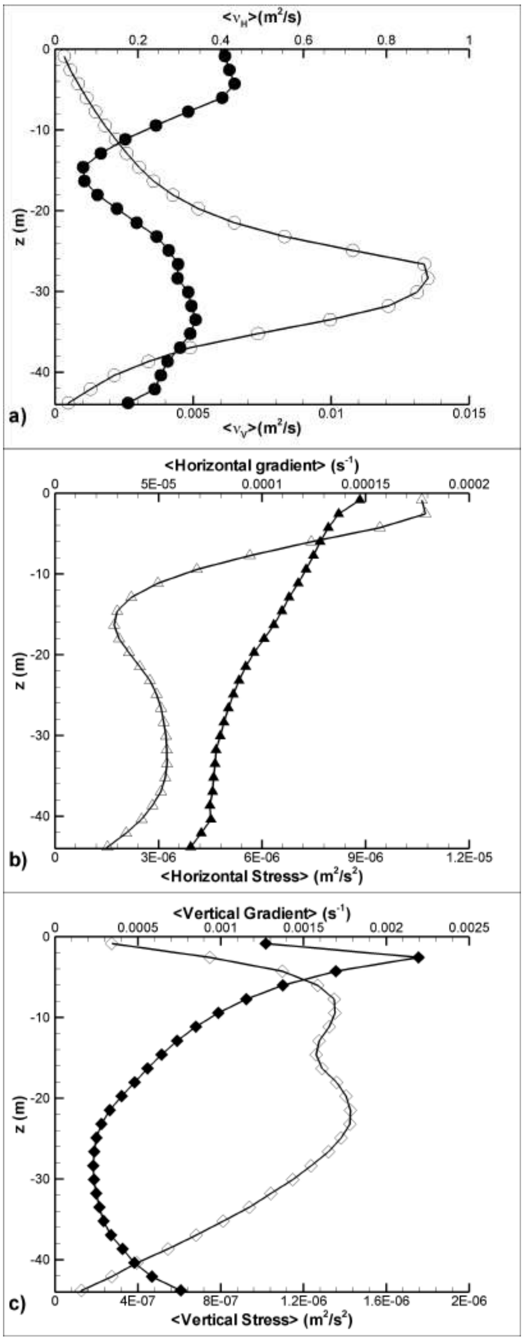

Figure 5.6: HWC. Vertical profiles of space-time quantities averaged over 8 hours: a) $\langle \nu_V \rangle$ (○) and $\langle \nu_H \rangle$ (•); b) horizontal stresses (△) and horizontal gradients (▲); c) vertical stress along z axis (◇) and vertical gradients along z axis (◆). Stresses and gradients correspond respectively to numerator and denominator in Eqs. 4.1 and 4.2.

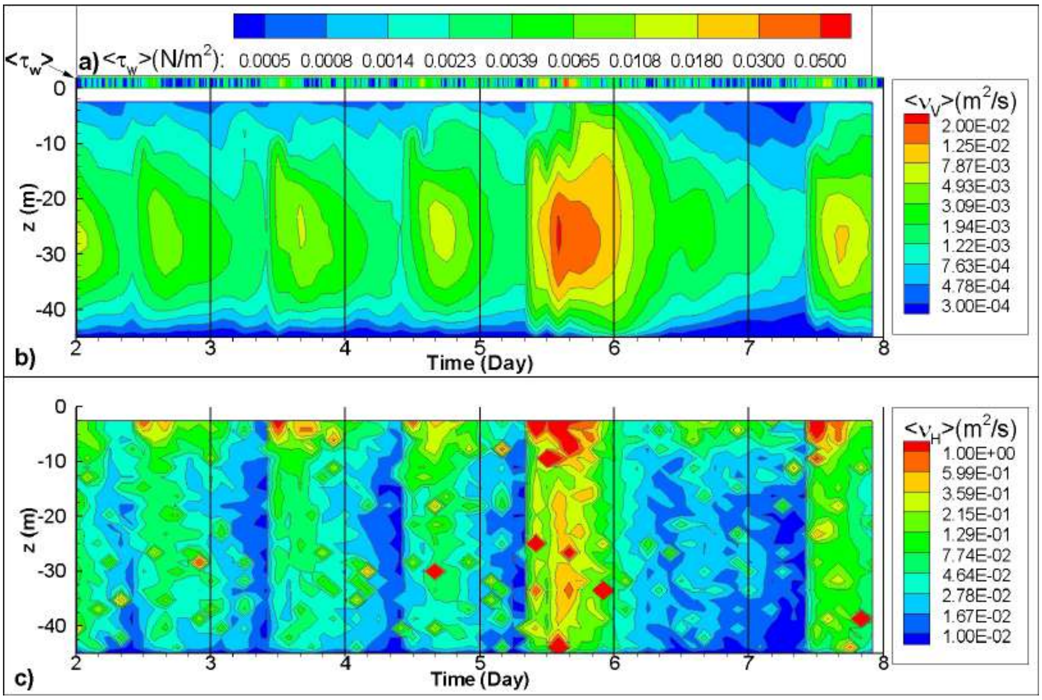

Figure 5.7: HWC. Vertical profiles of space-time quantities averaged over 2 hours along the latter six days of simulation: a) $\langle \tau_w \rangle$; b) $\langle \nu_V \rangle$ and c) $\langle \nu_H \rangle$.

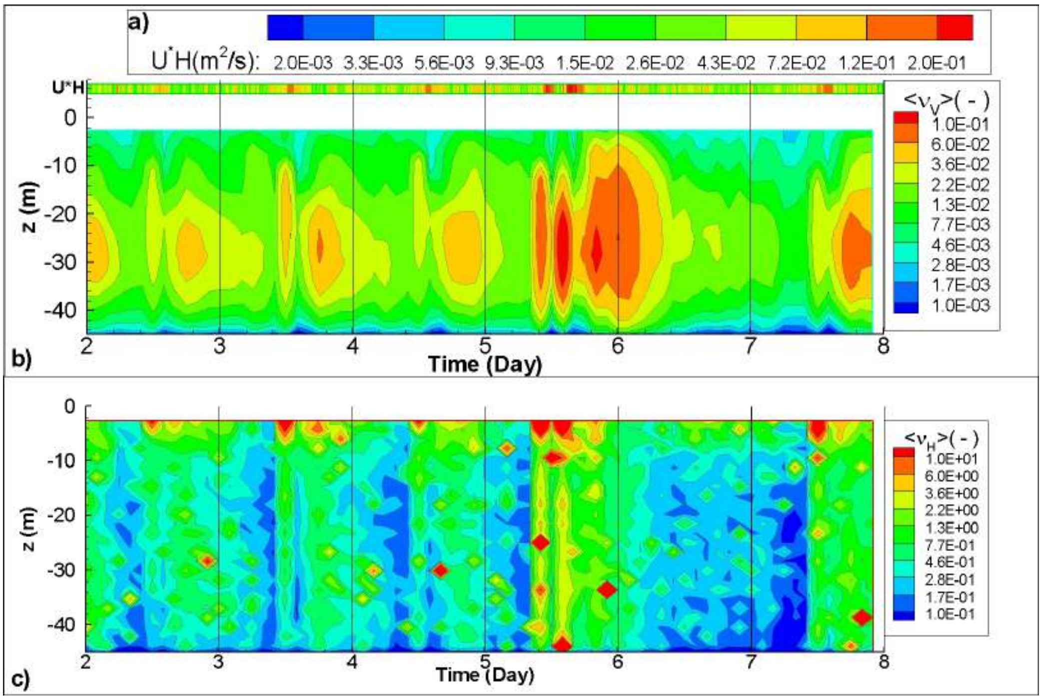

Figure 5.8: HWC. Vertical profiles of space-time quantities averaged over 2 hours along the latter six days of simulation: a) $\langle u^*H \rangle$; b) $\langle \nu_V \rangle$ normalized with u^*H and c) $\langle \nu_H \rangle$ normalized with u^*H.

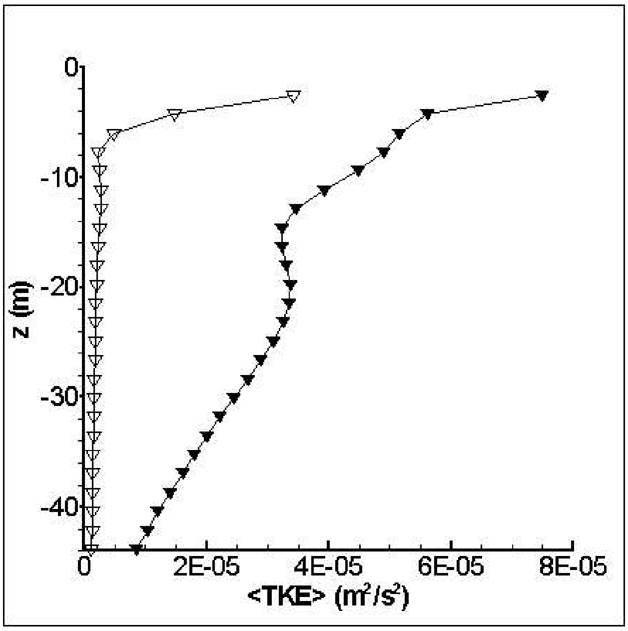

Figure 5.9: HWC. Vertical profile of the space-time $\langle TKE \rangle$ averaged over 2 hours between 10:00 - 12:00 of day 3 ($\triangledown$) and between 14:00 and 16:00 of day 5 ($\blacktriangledown$).

the inhomogeneity of the wind on the hydrodynamic of the lake.

5.3 Turbulent Kinetic Energy and TKE Dissipation Rate

As for the eddy viscosity analysis, $\langle TKE \rangle$ and $\langle \epsilon \rangle$ were calculated between 10:00 -12:00 of day 3 and between 14:00 and 16:00 of day 5, when the wind is characterized by $\langle \tau_w \rangle \sim 0.002 N/m^2$ and $\langle \tau_w \rangle \sim 0.02 N/m^2$ respectively; they are reported in Fig. 5.9 and Fig. 5.10. High values of $\langle TKE \rangle$ are detected close to the free surface, a 'minimum-stress' plane is present at $z \sim -16$ m and small values are observed at the bottom of the lake. As claimed in section 4.3 this is an evidence of the fact that the wind is the main source of turbulence, the latter nearly absent at the bottom of the lake, consistently with the results of the eddy viscosity analysis.

The total dissipation rate is composed of two terms. The contribution

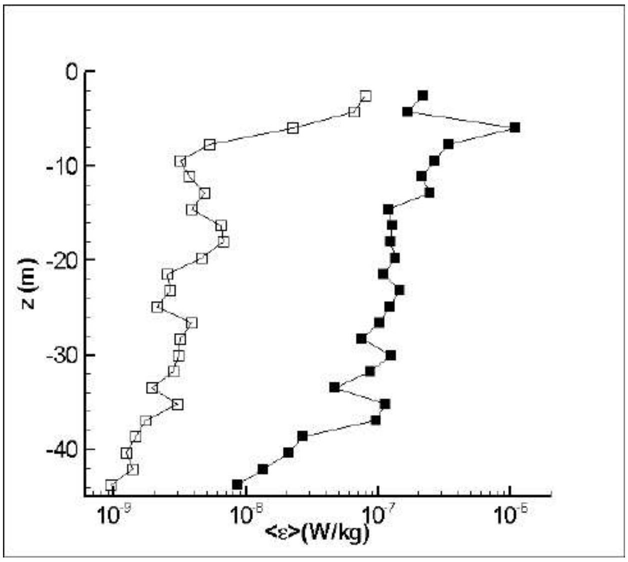

Figure 5.10: HWC. Vertical profile of the space-time $\langle\epsilon\rangle$ averaged over 2 hours between 10:00 - 12:00 of day 3 (□) and between 14:00 and 16:00 of day 5 (■).

of the resolved scales is of the order of $10^{-14} - 10^{-15}$ W kg^{-1}, suggesting that most of the dissipation occurs at the subgrid scales, as expected due to the resolution herein employed.

The averaged dissipation rate ranges between 10^{-9} W kg^{-1} and 10^{-6} W kg^{-1}; it peaks in the SBL, decreases exponentially in the top 15 m and reaches the minimum value at the bottom of the lake. The typical increase of ϵ in the Bottom Boundary Layer (BBL) is not present in our case, due to the absence of stratification and seiches (Wuest et al., 2000). On the other hand, it is possible to estimate the intensity of the boundary layer induced in the Lake Ledro due to seiches by taking advantage of the knowledge on tidal-induced boundary layer theory (see Salon et al. (2007) and references therein). Based on available data, a typical free-surface seiche in the Lake Ledro has been estimated as having a period of $T_s = 2L_s/\sqrt{(gH_s)} \sim 240$ s, considering a horizontal length $L_s = 2500$ m, with a typical amplitude $H_s = 0.04$ m. With these values we can calculate a horizontal pressure gradient associated to the hydrostatic unbalance between the two sides of the lake having an amplitude of $\Pi_0 = 0.16$ N m^{-3}. Assuming a sinusoidal oscillation of the horizontal

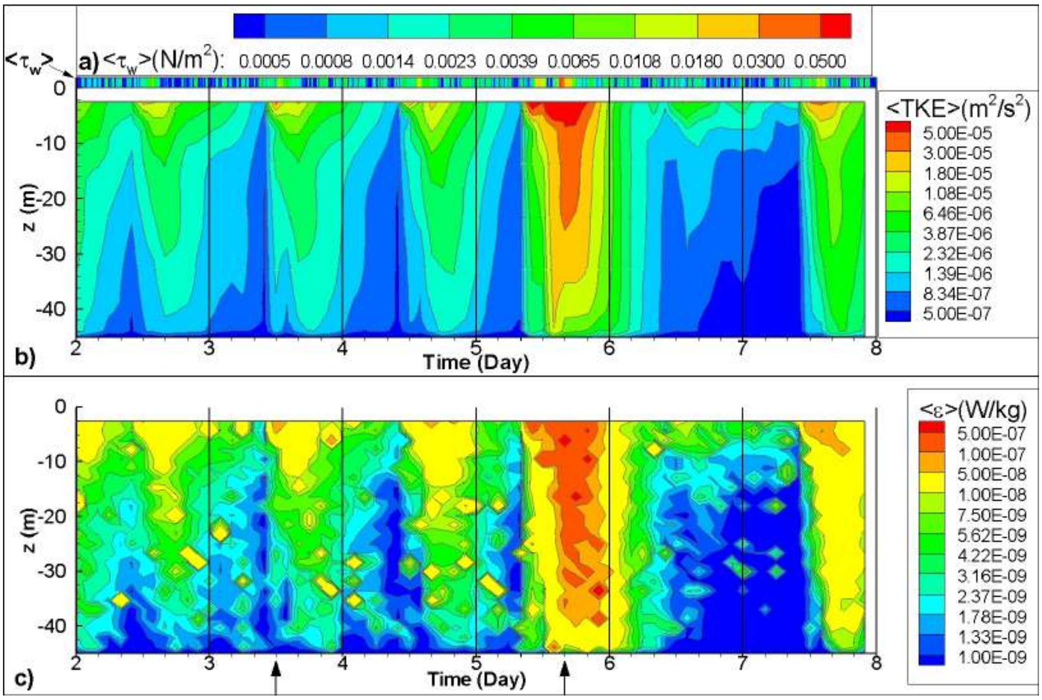

Figure 5.11: HWC. Vertical profiles of space-time quantities averaged over 2 hours along the latter six days of simulation: a) $\langle\tau_w\rangle$; b) $\langle TKE\rangle$ and c) $\langle\epsilon\rangle$. The vertical profile of the $\langle TKE\rangle$ and $\langle\epsilon\rangle$ at the time indicated by the arrows in c) are reported in Fig. 5.9 Fig. 5.10.

pressure gradient $\Pi = \Pi_0 \sin(2\pi t/T_s)$, since in the outer layer of the BBL $\partial U/\partial t = -\Pi$, we can estimate the amplitude of the free-stream motion at the bottom surface as $U_s = T_s \Pi_o/(2\pi\rho) = 6.1 \times 10^{-3}$ m s^{-1}. The BBL intensity can be estimated based on the value of $Re = U_s^2 T_s/(2\pi\nu) \sim 1400$ smaller than the value 1.5×10^5 at which the boundary layer moves into a transitional intermittent regime (Salon et al. (2007)); thus the BBL induced by the free surface seiche is very weak and in the laminar regime. Hence, the typical increase of ϵ in the BBL is not expected to occur due to free-surface seiches.

Figure 5.11 shows the evolution along the latter 6 days simulated of the vertical profiles of two-hour space-time averaged $\langle TKE\rangle$ and $\langle\epsilon\rangle$. They appear substantially modulated according to the intensity of the wind stress. $\langle TKE\rangle$ is approximately in phase with the wind stress at the free surface, peaking a bit earlier than the wind intensity and approximately in phase

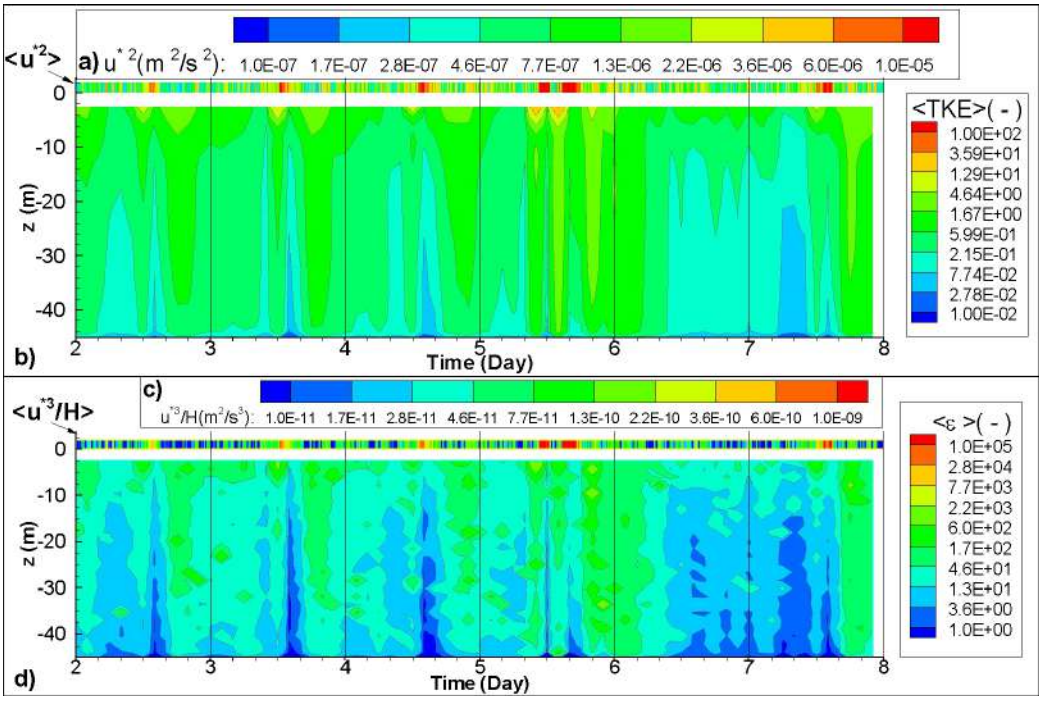

Figure 5.12: HWC. Vertical profiles of space-time quantities averaged over 2 hours along the latter six days of simulation: a) $\langle u^{*2} \rangle$; b) $\langle TKE \rangle$ normalized with u^{*2}; c) $\langle u^{*3}/H \rangle$ and d) $\langle \epsilon \rangle$ normalized with u^{*3}/H

with the change of wind direction which may constitute an additional source of turbulence. $\langle TKE \rangle$ exhibits the largest values in the free-surface region, as expected due to the fact that the wind stress is the only source of turbulence. It propagates toward the deeper layers with a time delay of the order of 8 hours, appearing a bit reduced when the wind intensity increases. This indicates that the large scales of motions, represented by the large vortices present in the water basin are not able to transfer turbulent fluctuations very rapidly along the water depth. When the wind increases, the turbulence is enhanced and is able to transfer at a faster rate fluctuations toward the bottom.

The space-time averaged $\langle \epsilon \rangle$ behaves similarly to $\langle TKE \rangle$ indicating the presence of equilibrium turbulence along the water column, thus suggesting that the unsteady term of the transport equation of TKE may plays a minor role. Overall the analysis suggest that the turbulent time scales are much smaller that the time scale of the wind forcing. Moreover, the horizontal distribution of TKE in the SBL is similar to that of ν_H, supporting the correlation between the two quantities.

Like the eddy viscosity analysis, in order to evaluate the role of the wind shear stress on the magnitude of the $\langle TKE \rangle$ and its dissipation rate, these quantities have been scaled with u^{*2} and u^{*3}/H respectively, and shown in Fig 5.12. They will be used in Chapter 6 in order to evaluate the role of the inhomogeneity of the wind on the hydrodynamic of the lake.

Chapter 6

INHOMOGENEOUS WIND FIELD

The results shown in the previous sections are relative to an idealized wind, which acts homogeneously over the surface of the lake. Although in some cases this condition may be representative of the actual situation, it is hardly met for peri-alpine lakes, which are characterized by being embedded in valleys with complex orography, creating complex local wind patterns. In this section the circulation generated by an inhomogeneous wind stress has been analized, provided by the WRF model, with the aim of highlighting the main differences with the HWC.

6.1 Velocity Field Inhomogeneities and Kinetic Energy

The main differences with the previous HWC is that inhomogeneity may create zones of relevant horizontal divergence in the free surface region and also that the local orography may produce zones of either very low or high wind speed. The latter effect is quantified by the root mean square deviations (RMS) of the two horizontal components U_w and V_w of the wind velocity with respect to their space averaged values (Fig. 6.1).

The first three days are characterized by a low inhomogeneity of the

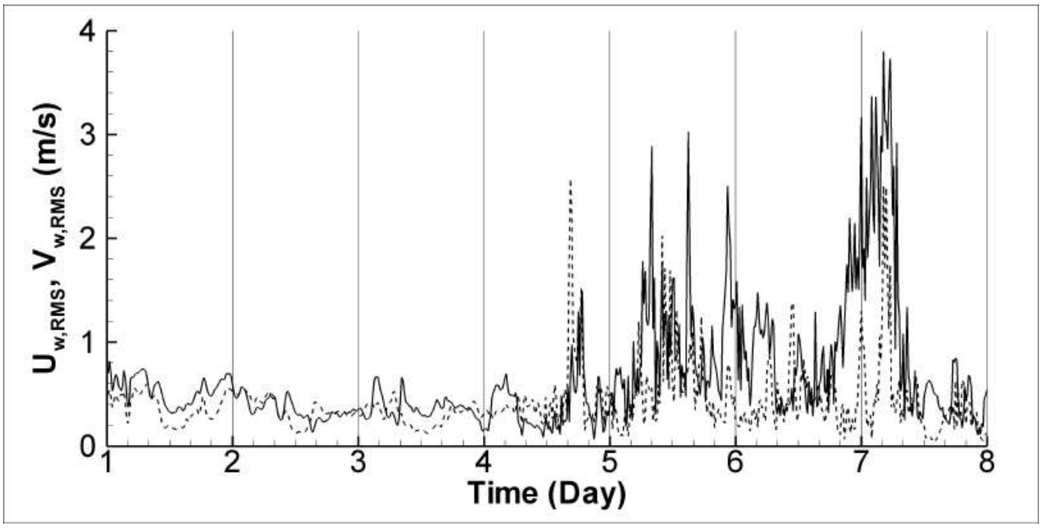

Figure 6.1: IWC. Root Mean Square (RMS) of U_w (solid line) and V_w (dotted line) over the lake between day 1 (16 January 2012) and day 7 (22 January 2012).

direction of wind: the hydrodynamics generated during these three days indeed do not differ significantly from that generated using the homogeneous wind condition. On the contrary, the last 4 days are characterized by a strong inhomogeneity in the wind forcing: peaks of the RMS of U_w and V_w occur in the afternoon of day 4 of the simulation, during day 5, and in the early morning of day 7.

Figure 6.2 shows the instantaneous wind field 2.8 m above the water surface and the horizontal divergence of the velocity field below the free surface. One of the two effects of wind inhomogeneity is the occurrence of non-zero horizontal divergence. Positive values indicate local upwelling events, the opposite is true for negative values. These effects are even more intense in correspondence of the most relevant wind stress events acting on the surface of the lake. In general, the inhomogeneity of the wind represents an additional source of mixing, not present when the wind blows homogeneously on the surface of the lake. This lends justification to the discussion of eddy viscosities, turbulent kinetic energy and its dissipation rate reported below.

In Fig. 6.3 the temporal and spatial response of the lake in terms of horizontally-averaged Kinetic Energy ($KE = 1/2\rho\sqrt{u^2 + v^2 + w^2}$) to the non-

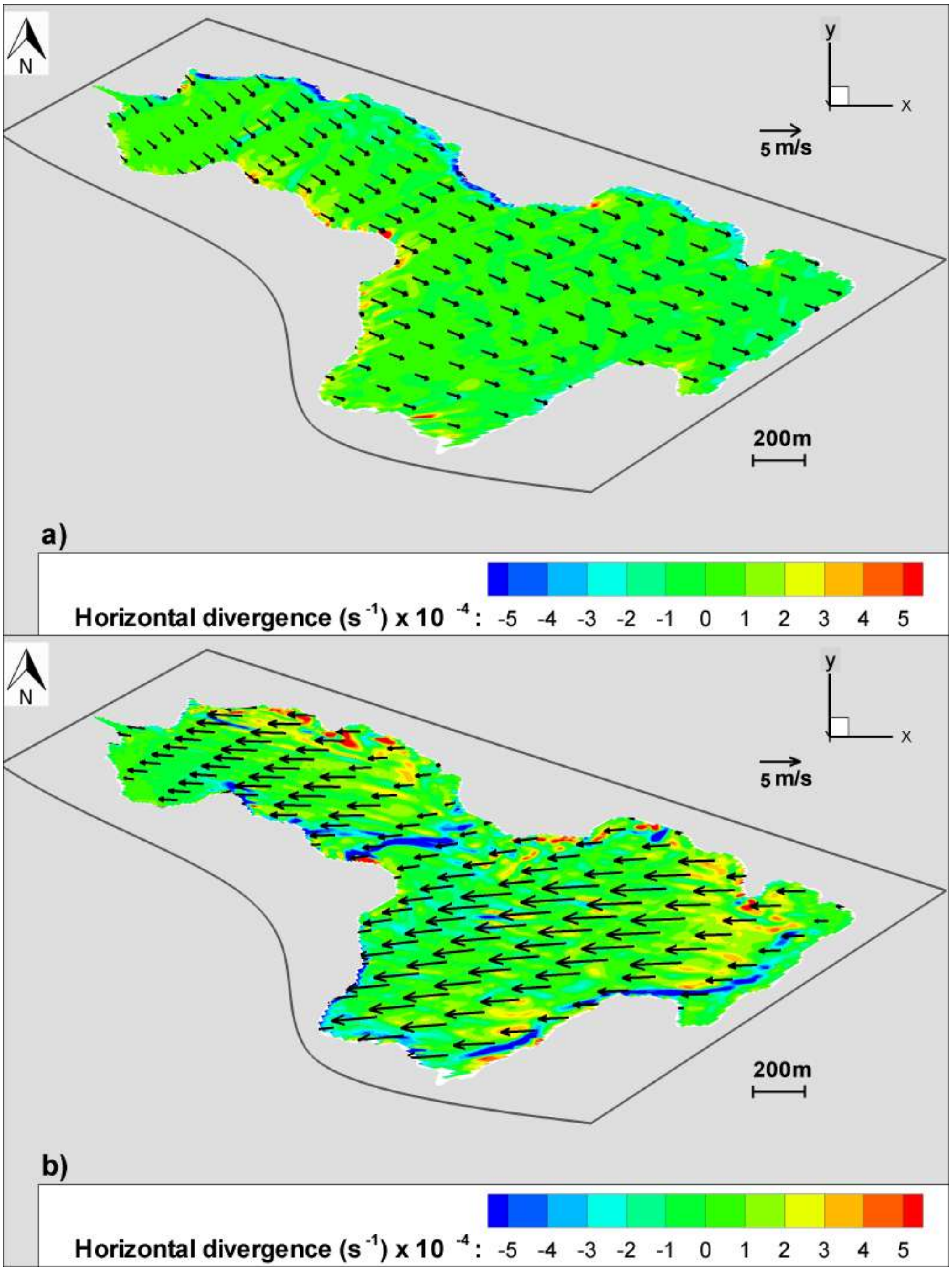

Figure 6.2: IWC. Contour plot at z=-0.8m of depth of the divergence of the horizontal velocity field together with vectors of the wind field 2.8 m above the surface of the Lake: a) small inhomogeneity at 19:30 of the day 3 b) large inhomogeneity at 23:15 of day 6.

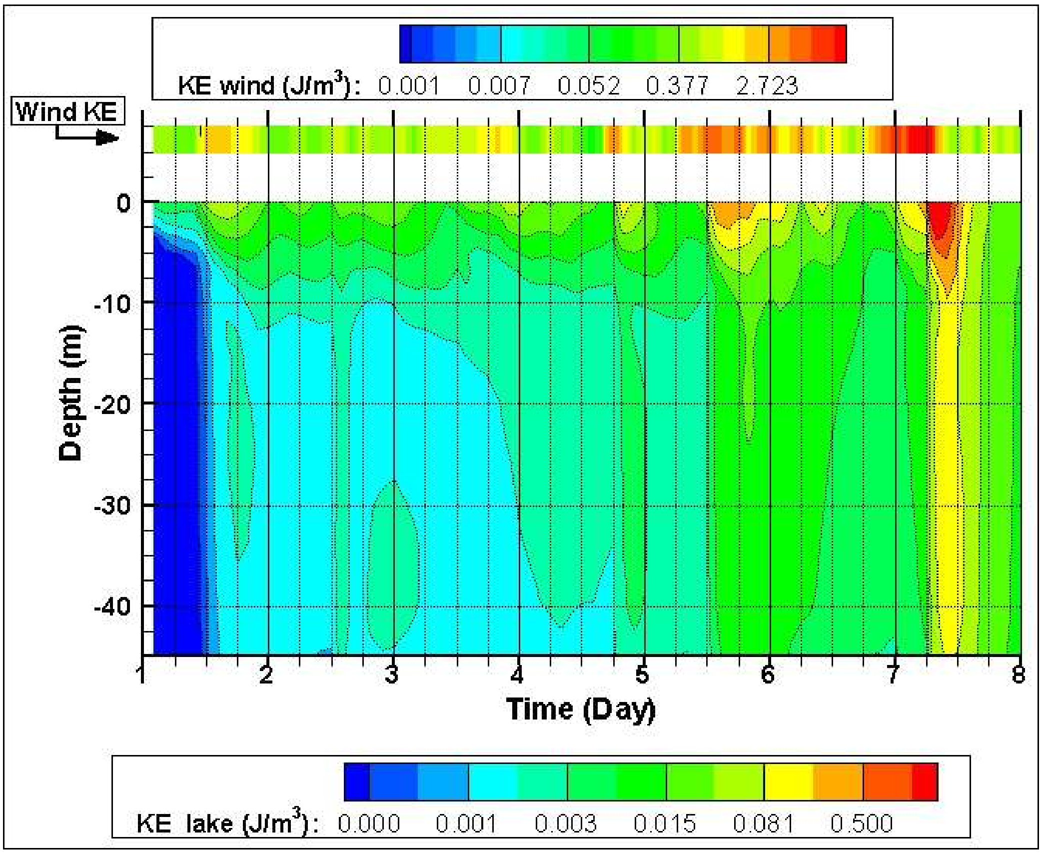

Figure 6.3: IWC. Temporal evolution of the horizontally-averaged Kinetic Energy (KE) in the simulation with realistic inhomogeneous wind forcing: KE of the wind (first row), and vertical distribution of the KE in the lake. Starting from the quiescent state, the flow field in the inner part of the lake can be considered developed after the first 12 hours.

homogeneous wind conditions are shown, starting from the quiescent state. After 12 hours the velocity field along the water column can be considered developed and, as observed in section 5.3 for the homogeneous-wind case, after 24 hours the entire flow field can be considered developed. The evolution of the KE along the water column follows in time the peak of wind KE, but only in correspondence of the long-lasting wind KE events (between 06:00 of 5^{th} day and 00:00 of the 6^{th} day, and between 18:00 of the 6^{th} day and 09:00 of the 7^{th} day) higher values of KE are obtained at the bottom of the lake.

6.2 Eddy Viscosities

Fig. 6.4 shows the contour plots of the eddy viscosities calculated taking into account the 8-hour averaged field (in the interval 08:00 - 16:00 of the 5^{th} day) for the inhomogeneous wind case. Differently from the homogeneous wind case, the horizontal eddy viscosity exhibits high values only in the SBL up to $z = -8$ m (Fig. 6.4a, Fig. 6.5a); below that depth it decreases rapidly, whereas the vertical eddy viscosity increases reaching its maximum in the interior of the lake between -20 and -30 m (Fig. 6.4b and Fig. 6.5a), as in the homogeneous wind case. Moreover, there is evidence of a weak 'minimum-stress plane' (Fig. 6.5b,c), where the horizontal and, especially, the vertical Reynolds stresses exhibit a local minimum in the interior of the lake. The horizontal distribution of the two eddy viscosities for the inhomogeneous wind case, just above the 'minimum-stress plane' (7.7 m below the surface) presents relatively higher values of horizontal (Fig. 6.4c) and vertical (Fig. 6.4d) eddy viscosity in the center of the lake and along the shoreline, respectively.

The evolution along the latter 6 days, of the vertical profile of the two-hours space-time averaged eddy viscosities is in Fig. 6.6. With respect to the HWC (Fig. 5.7) the vertical eddy viscosity is less regular (periodic) and overall smaller in the first days of light breeze and low inhomogeneity. However, the quantities made non dimensional with Hu^* (Fig. 6.7), are overall larger for the inhomogeneous case with respect to the HWC (Fig. 5.8). This means that the eddy viscosity resulting from a certain wind stress is larger in the inhomogeneous case. This is even more true in the last days

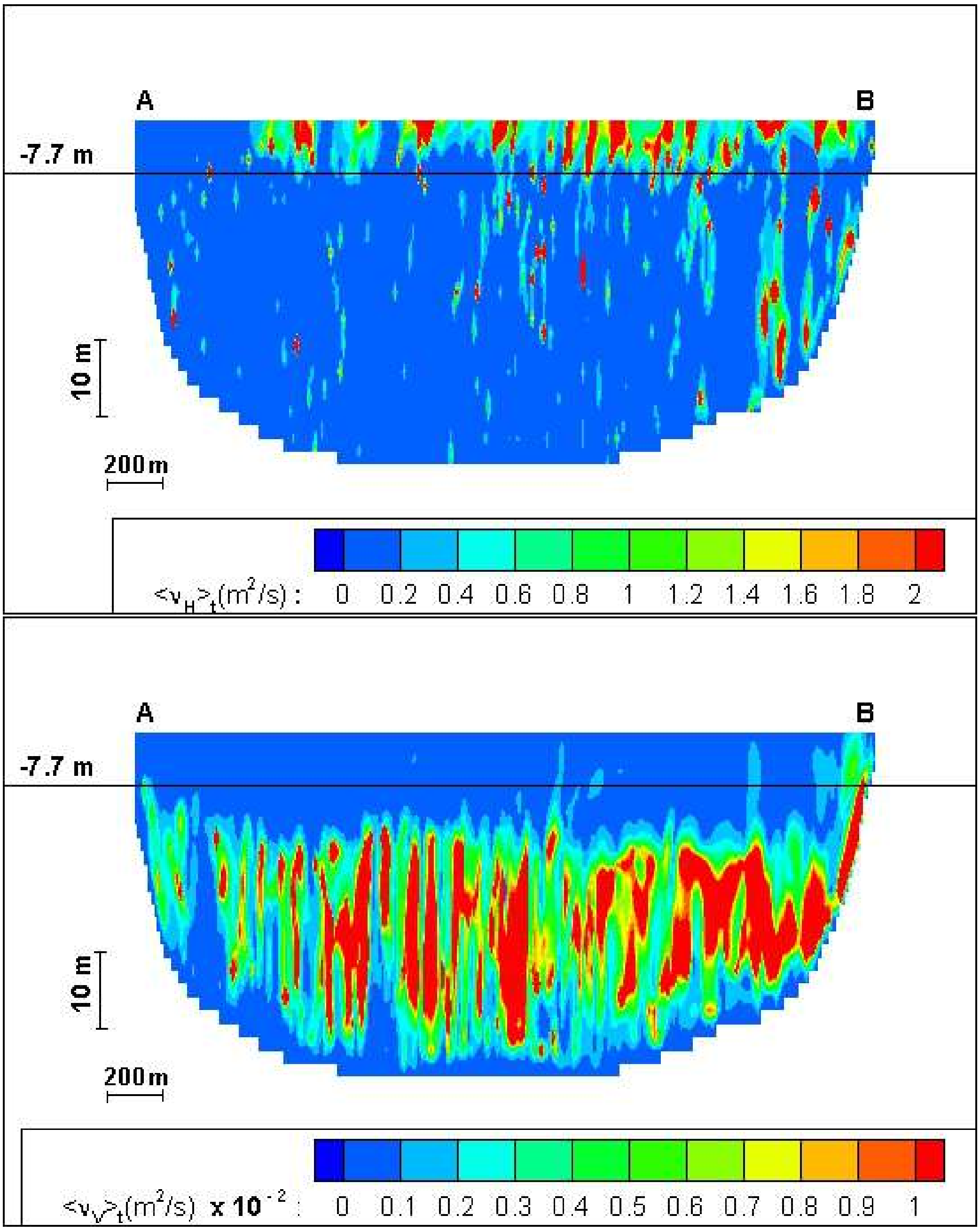

Figure 6.4: continue

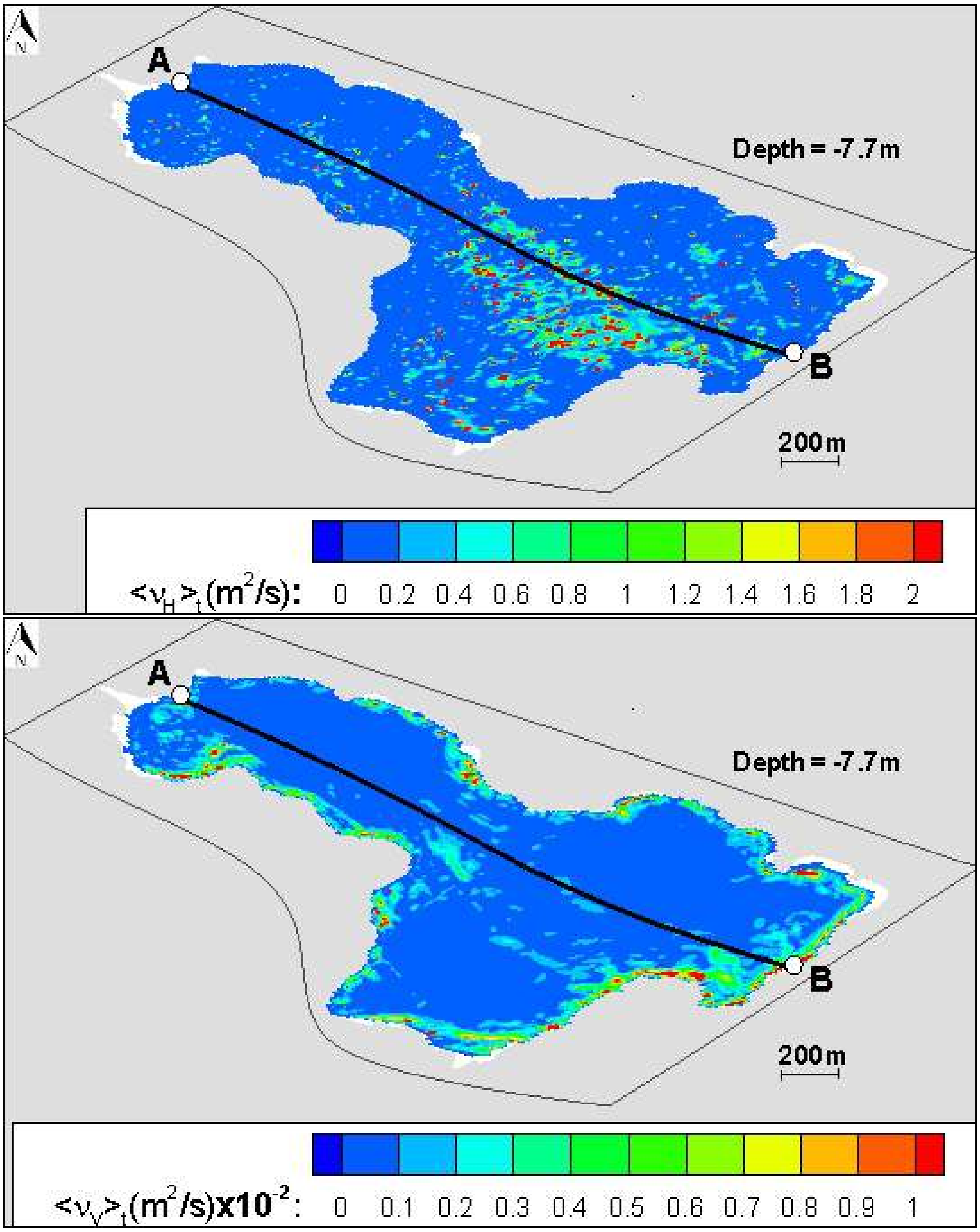

Figure 6.4: IWC. Horizontal ν_H (a, c) and vertical ν_V (b, d) eddy viscosity obtained from the simulation with inhomogeneous wind forcing (8-hour average between 08:00 and 16:00 of 20 January: contour plots along the major axis AB (a, b; see Fig. 1.1a) and on a horizontal plane at z=7.7 m (c,d)

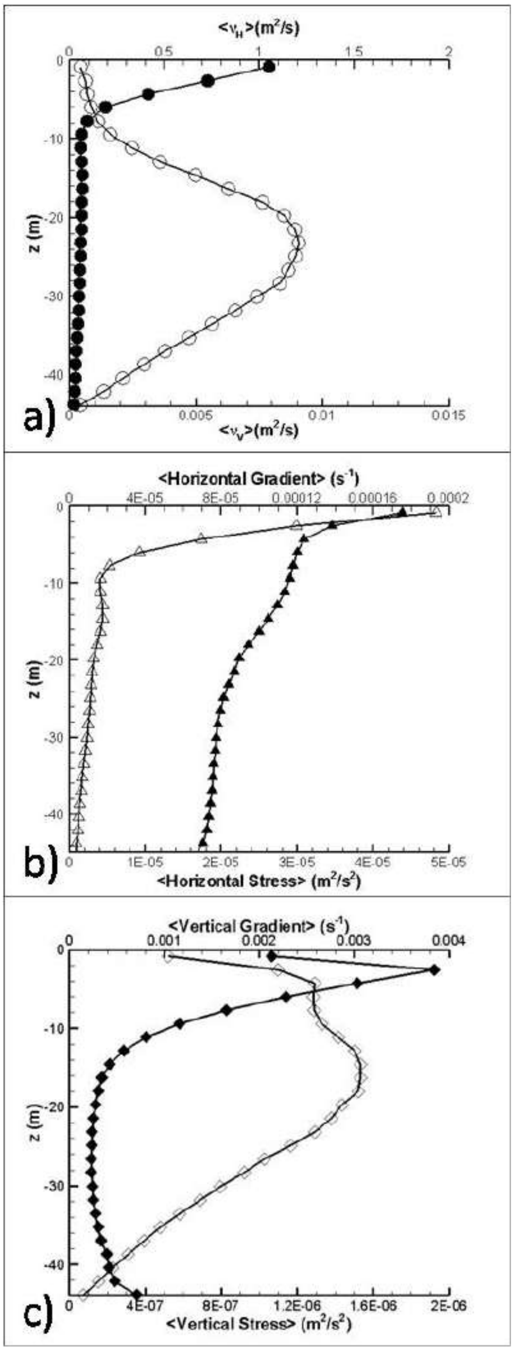

Figure 6.5: IWC. Vertical profiles of horizontally averaged quantities (simulation with inhomogeneous wind forcing, 8-hour average between 08:00 and 16:00 of 20 January): a) vertical eddy viscosity $\langle \nu_V \rangle$ (○) and horizontal eddy viscosity $\langle \nu_H \rangle$ (•); b) horizontal stresses (△) and horizontal gradients (▲); c) vertical stress along z axis (◇) and vertical gradient along z axis (◆). Stresses and gradients correspond respectively to numerator and denominator in Eqs. 4.2 and 4.1.

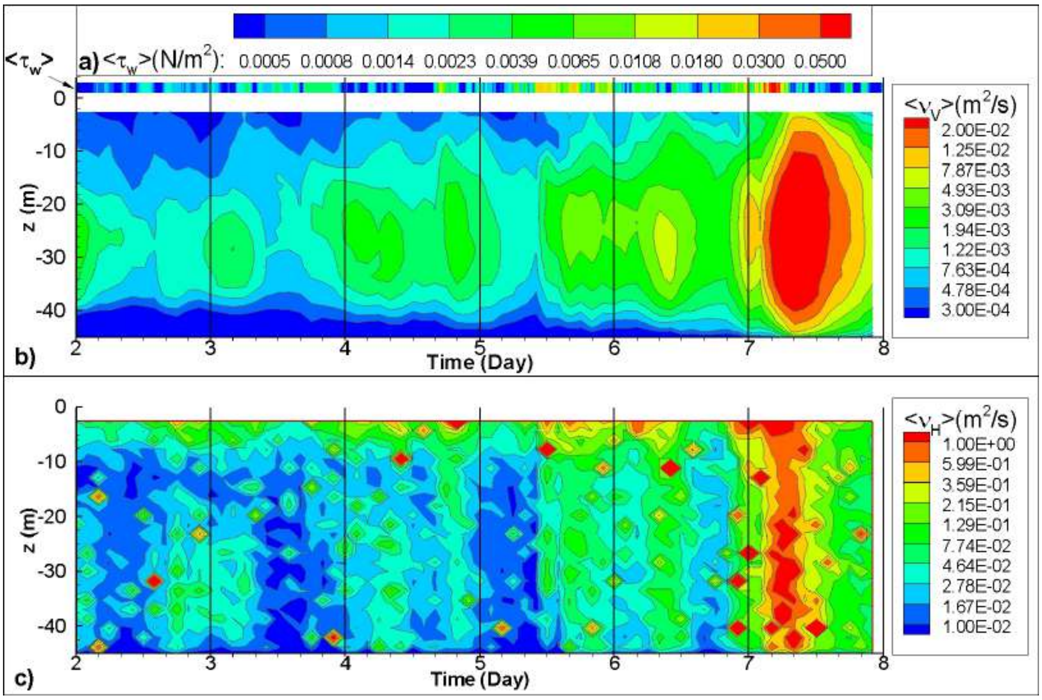

Figure 6.6: IWC. Vertical profiles of space-time quantities averaged over 2 hours along the latter six days of simulation: a) $\langle \tau_w \rangle$; b) $\langle \nu_V \rangle$ and c) $\langle \nu_H \rangle$.

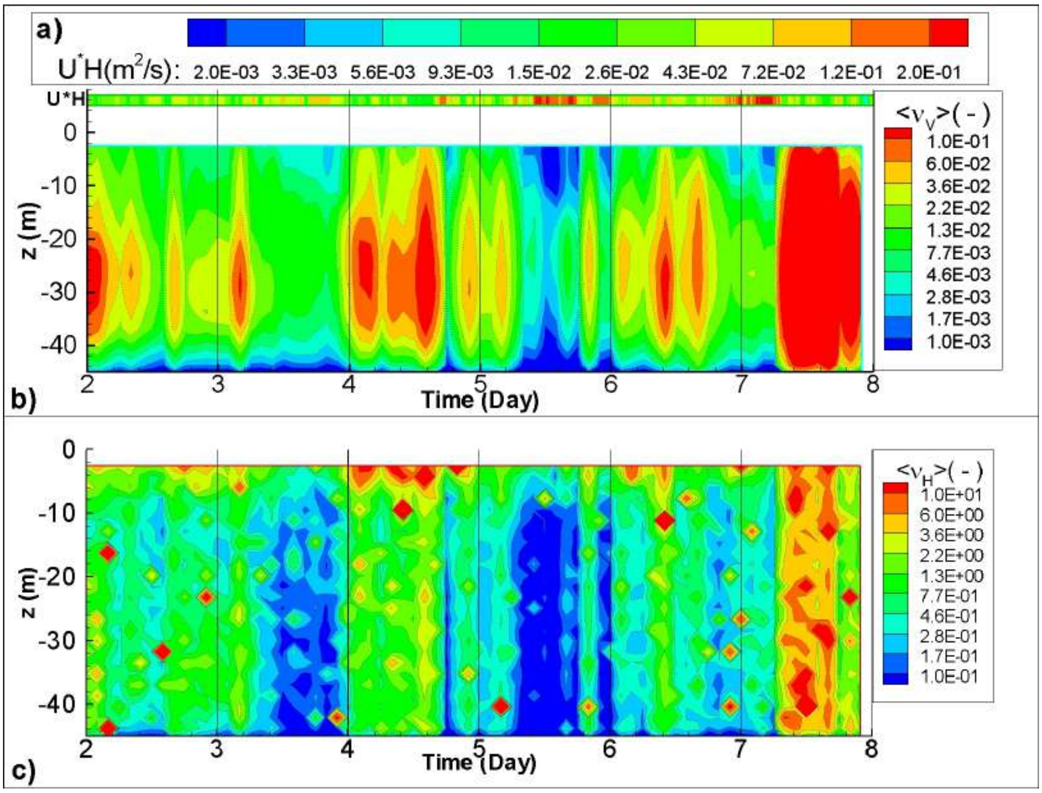

Figure 6.7: IWC. Vertical profiles of space-time quantities averaged over 2 hours along the latter six days of simulation: a) $\langle u^* H \rangle$; b) $\langle \nu_V \rangle$ normalized with $u^* H$ and c) $\langle \nu_H \rangle$ normalized with $u^* H$.

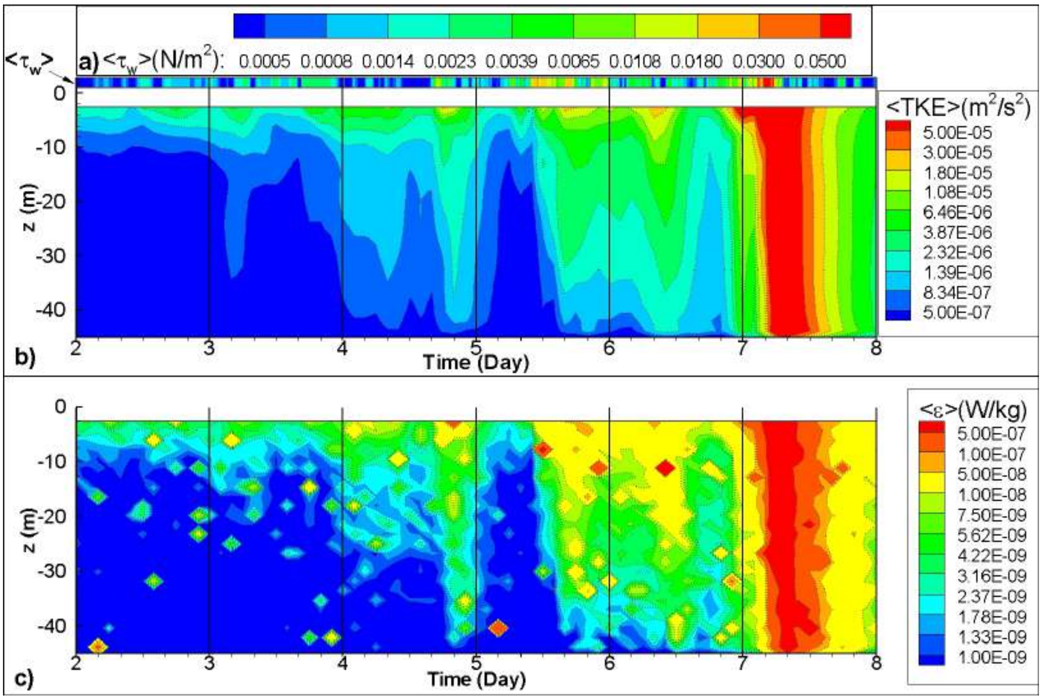

Figure 6.8: IWC. Vertical profiles of space-time quantities averaged over 2 hours along the latter six days of simulation: a) $\langle \tau_w \rangle$; b) $\langle TKE \rangle$ and c) $\langle \epsilon \rangle$.

of the simulations, characterized by the synoptic events giving rise to large inhomogeneity. The same discussion holds for the horizontal eddy viscosity. Even if the dimensional values in the case of light breeze appear larger in HWC, the non dimensional values are always larger in the IWC.

6.3 Turbulent Kinetic Energy and TKE Dissipation Rate

The same behavior holds for the evolution along the six days of the vertical profiles of the two-hours space-time averaged TKE and its dissipation rate (Fig. 6.8). In presence of light wind the dimensional values appear larger for HWC. However, in order to quantify the turbulent kinetic energy and its dissipation rate associated to a certain intensity of wind stress, these quantities have been made non dimensional with u^{*2} and u^{*3}/H respectively, and

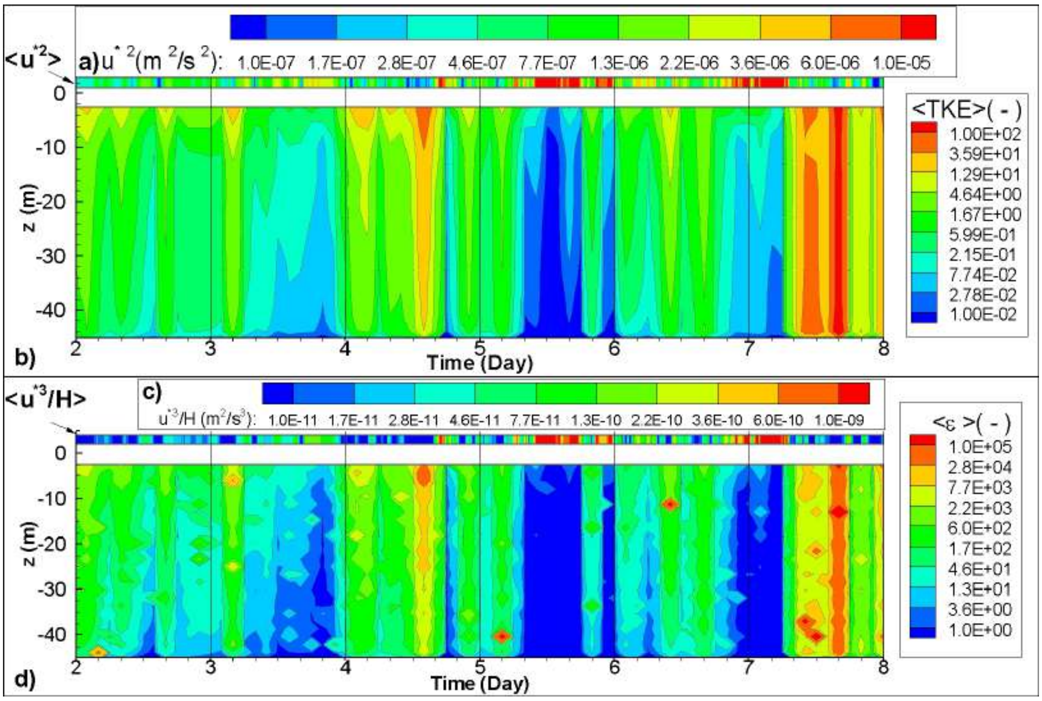

Figure 6.9: IWC. Vertical profiles of space-time quantities averaged over 2 hours along the latter six days of simulation: a) $\langle u^{*2} \rangle$; b) $\langle TKE \rangle$ normalized with u^{*2}; c) $\langle u^{*3}/H \rangle$ and d) $\langle \epsilon \rangle$ normalized with u^{*3}/H.

reported in in Fig. 6.9. As for the eddy viscosities, the non dimensional quantities appear always larger for the IWC with respect to the HWC. Finally, in presence of large inhomogeneity, (last day of the simulation) the dimensional quantities appear larger for the IWC, suggesting that spatial variation of the wind stress may provide an additional source of mixing. The phase-lag between the wind stress and the two quantities $\langle TKE \rangle$ and $\langle \epsilon \rangle$ is not appreciably different from the HWC. The phase-lag between the values of the two quantities at the surface and the correspondent values at the bottom of the lake appears a bit reduced and of the order of 6 hours suggesting that inhomogeneity may affect the response time of turbulence in the lake interior.

Chapter 7

STRATIFIED CASE

The analysis of the hydrodynamics of the Lake Ledro with different wind conditions has been conducted in presence of a neutral stratification. Such study is representative of the period between January and March when the temperature difference over the water column is about 0.5 ℃. The temperature difference between the bottom and the surface increases as summer approaches, reaching its maximum around 18 ℃ in July. With a such thermal stratification the buoyancy term of eq.2.4 cannot be neglected. In the present Chapter the stable stratification case is analyzed. The cases reported below refer to April and November when the temperature difference between the surface and the bottom of the Lake Ledro is about 5 ℃. Two wind conditions are considered of the Stratified Case (SC): the Homogeneous and Steady Wind Case (HSWC) and the Inhomogeneous Wind Case (IWC) both already described in the previous Chapters for the neutral case.

7.1 Homogeneous and Steady Wind Field

In order to estimate the effect of stable thermal stratification on the wind-driven circulation in Lake Ledro a steady homogeneous eastern wind with $U_{10} = 6m/s$ has been applied uniformly to the surface for 48 hours in absence of the Coriolis force. The thermal stratification has been initialized by imposing a temperature equal to 5 ℃ and 10 ℃ at the bottom and at the surface of the lake, respectively, and by applying a linear temperature gradient between them. The analysis shown in the present section is relative to the 2-hours average velocity field obtained after simulating 48 hours.

7.1.1 Velocity Field

As a representative example of the circulation occurring in presence of an homogeneous steady wind, snapshots of the 2-hours average velocity field were taken.

The vertical velocity averaged over 2 hours, the streamtracers and the isotherms at $z = -6m$ are shown in Fig. 7.1 together with the vertical transects along the axes AB. The streamlines and the contour of the vertical velocity indicate the presence of upwelling and downwelling areas along the windward and leeward shoreline of the lake, respectively and the presence in the central part of the lake of areas characterized by strong upwelling/divergence and downwelling/convergence aligned with the direction of the wind (Fig. 7.1a. Unlike the superstreaks described in Chapters 4, these cells span for about 100 m and are confined in the Surface Mixed Layer (SML); moreover, these areas constitute a sort of horizontal boundaries for the horizontal vortices (i.e. recirculation areas) shown in Fig. 7.1a which are absent in the neutral stratification case. In Fig. 7.1b is possible to appreciate that in correspondence of the downwelling and upwelling areas the horizontal velocity is concordant and opposite to the direction of the wind, respectively. Finally, the transect along the major axes of the lake is shown in Fig. 7.1c: in the SML the vertical stratification is weak and the horizontal $|U_H|$ is greater than in the interior of the lake where the flow is in a quiescent state.

7.1.2 Spatial Distribution of Eddy Viscosities

Contour plots of $\langle \nu_V \rangle_t$ and $\langle \nu_H \rangle_t$ over horizontal planes at $z = -6$ m are shown in Fig. 7.2.

As in the neutral cases, eddy viscosities are strongly anisotropic, with the horizontal one being about 2 orders of magnitude larger than the vertical one.

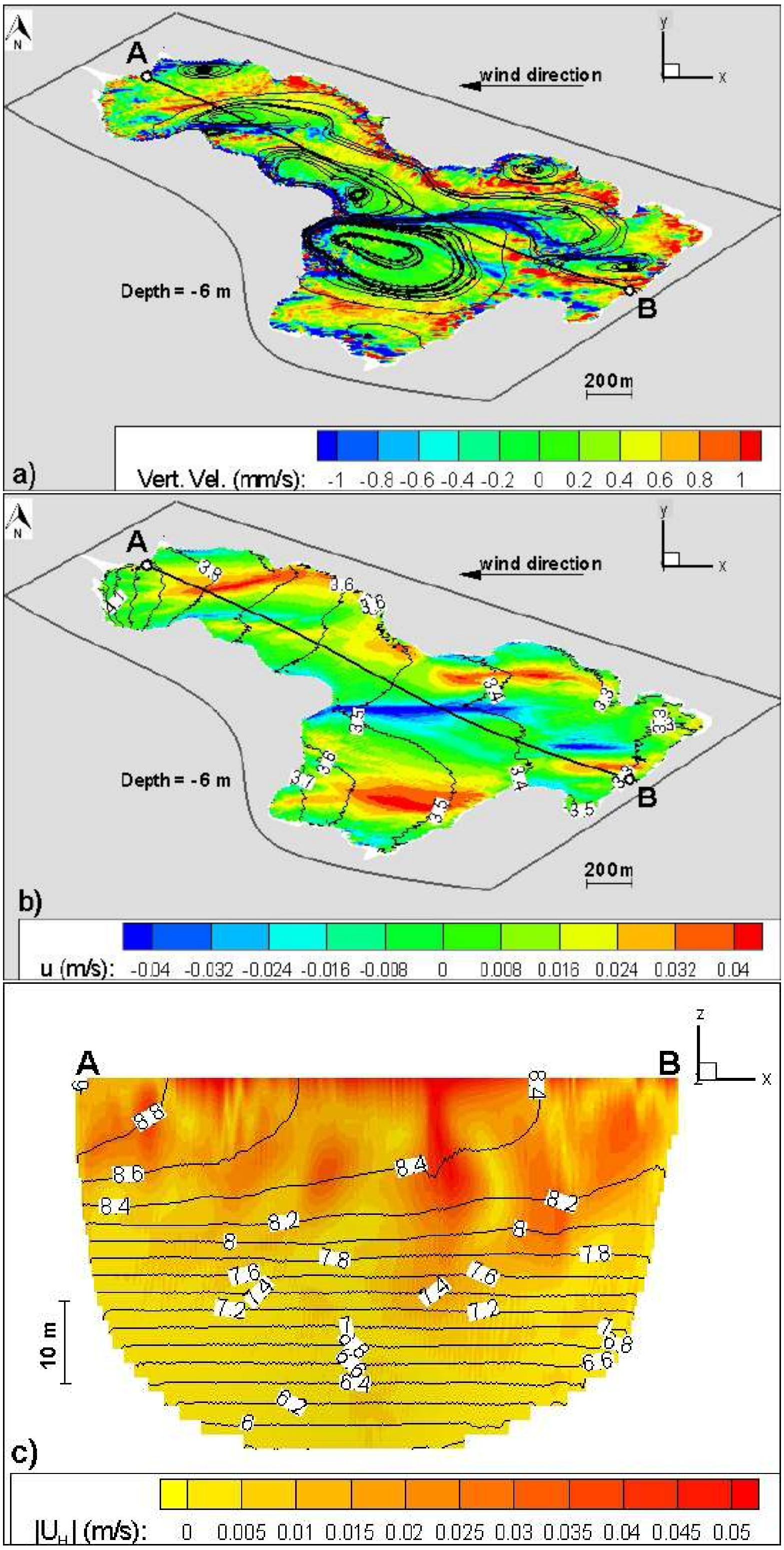

Figure 7.1: SC-HSWC. Snapshot of the velocity field averaged over 2 hours with easterly wind $U_{10} = 6\ m/s$: a) streamtracers and vertical velocity on a horizontal plane at 6 m depth, b) isotherms and u velocity on a horizontal plane at 6 m depth, c) isotherms and horizontal ($|U_H|$) velocity in transect AB.

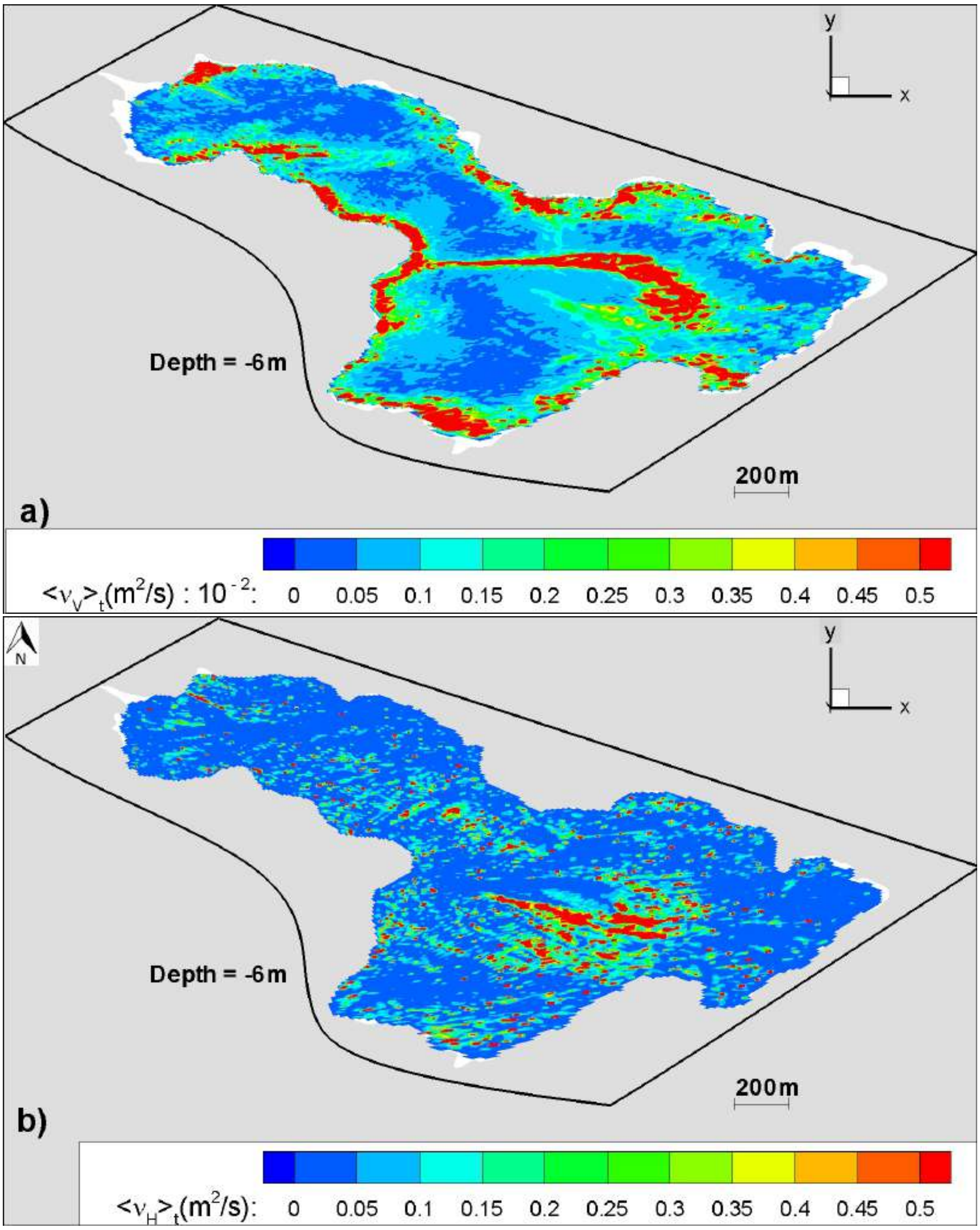

Figure 7.2: SC-HSWC. Eddy viscosities obtained averaging over 2-hours. Contour plots of: a) $\langle \nu_V \rangle_t$ and b) $\langle \nu_H \rangle_t$ on a horizontal plane at z=-6 m.

The two quantities exhibit substantial inhomogeneity along the horizontal planes.

In correspondence of the recirculation areas the horizontal eddy viscosity $\langle \nu_H \rangle_t$ presents its relative maximum due to the combination of the maximum of horizontal stress and the minimum horizontal gradients. Conversely the areas in correspondence of the convergence of the velocity field and along the shoreline are characterized by large values of vertical stresses and small values of vertical gradients; it turns into values of $\langle \nu_V \rangle_t$ shown in Fig 7.2. Stresses and gradients correspond respectively to numerator and denominator in Eqs. 4.1 and 4.2. The vertical profile of the two quantities $\langle \nu_H \rangle$ and $\langle \nu_V \rangle$ together with the vertical and horizontal stresses and gradients are reported in Fig.7.3. Differently from the neutrally stratified case, both the horizontal and vertical eddy viscosities have their maximum in the SML. They decrease with depth up to $z \sim -16$ m and remain constant in the interior of the lake. Differently from the HSWC shown in Section 4.2, the horizontal eddy viscosity seems to increases slightly in the bottom boundary layer, whereas the vertical stresses have greater values in the SML rather than in the interior of the lake (see Fig. 4.8c).

7.1.3 Turbulent Kinetic Energy and TKE Dissipation Rate

The vertical profiles and the spatial distribution over the horizontal plane at z=-6 m of $\langle TKE \rangle$ and $\langle \epsilon \rangle$ are shown in Fig. 7.4 and Fig. 7.5. High values of $\langle TKE \rangle$ are observed in the SML in particular in the areas of convergence and divergence and along the shoreline like in the neutral stratification cases shown in the previous chapters. The averaged dissipation rate of TKE has the maximum in the SML and decreases exponentially with the depth down to the bottom, specifically it has greater values along the shoreline and in correspondence of the greater values of the $\langle \nu_H \rangle$ and $\langle \nu_V \rangle$ in Fig. 7.2.

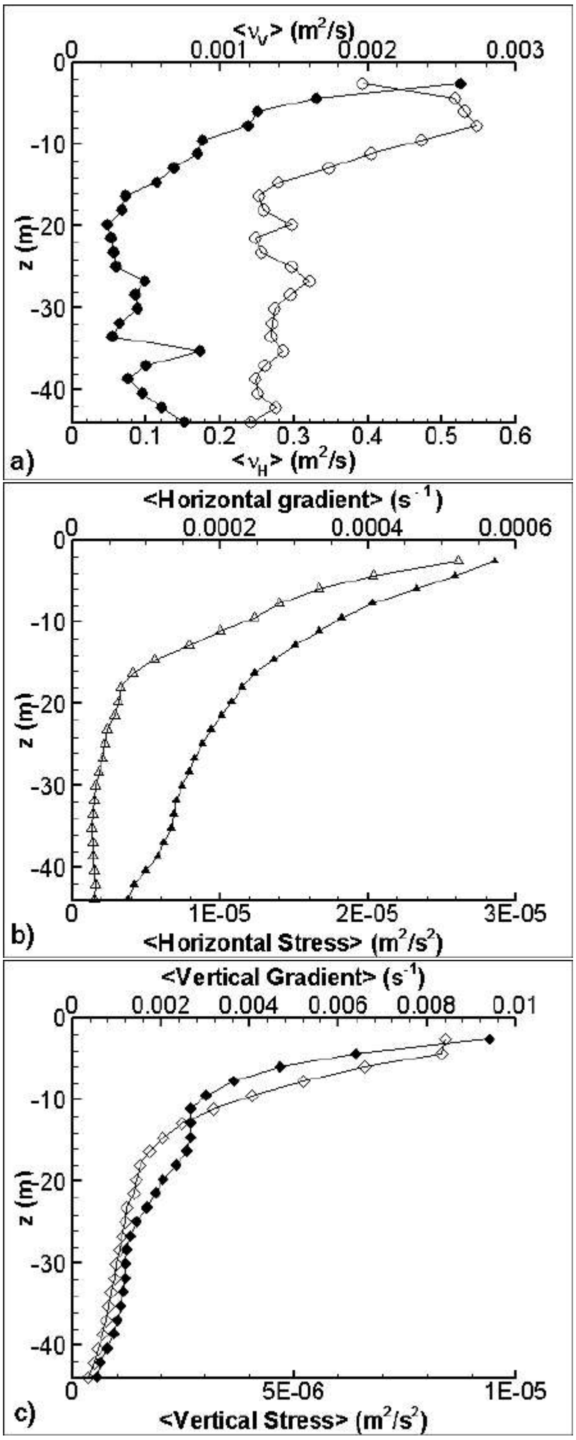

Figure 7.3: SC-HSWC. Vertical profiles of space-time quantities averaged over 2 hours: a) $\langle \nu_V \rangle$ (○) and $\langle \nu_H \rangle$ (•); b) horizontal stresses (△) and horizontal gradients (▲); c) vertical stress along z axis (◇) and vertical gradients along z axis (◆). Stresses and gradients correspond respectively to numerator and denominator in Eqs. 4.1 and 4.2.

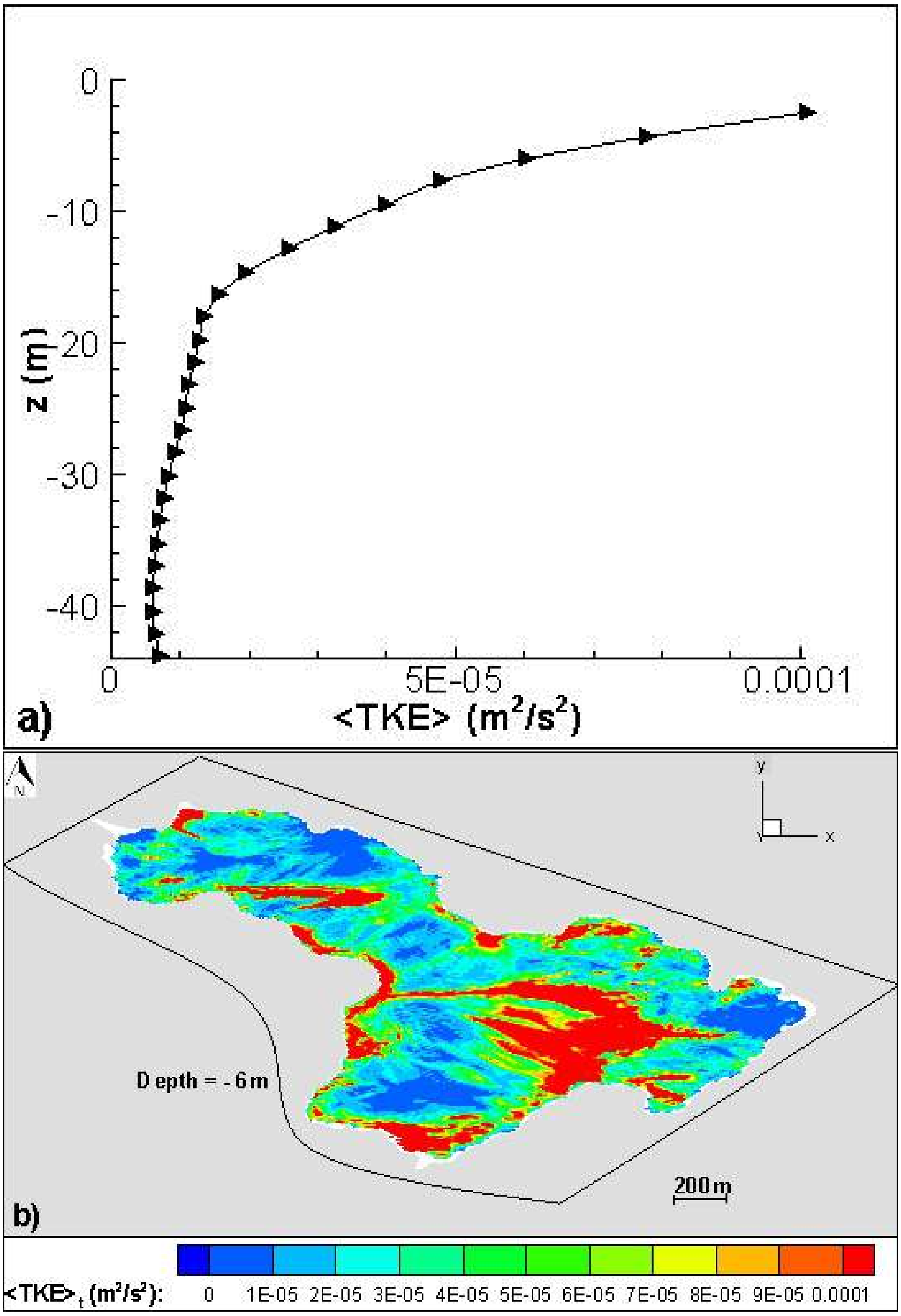

Figure 7.4: SC-HSWC. TKE: a) Vertical profile of $\langle TKE \rangle$ averaged over 2 hours, b) contour plot of $\langle TKE \rangle_t$ on a horizontal plane at z=-6 m.

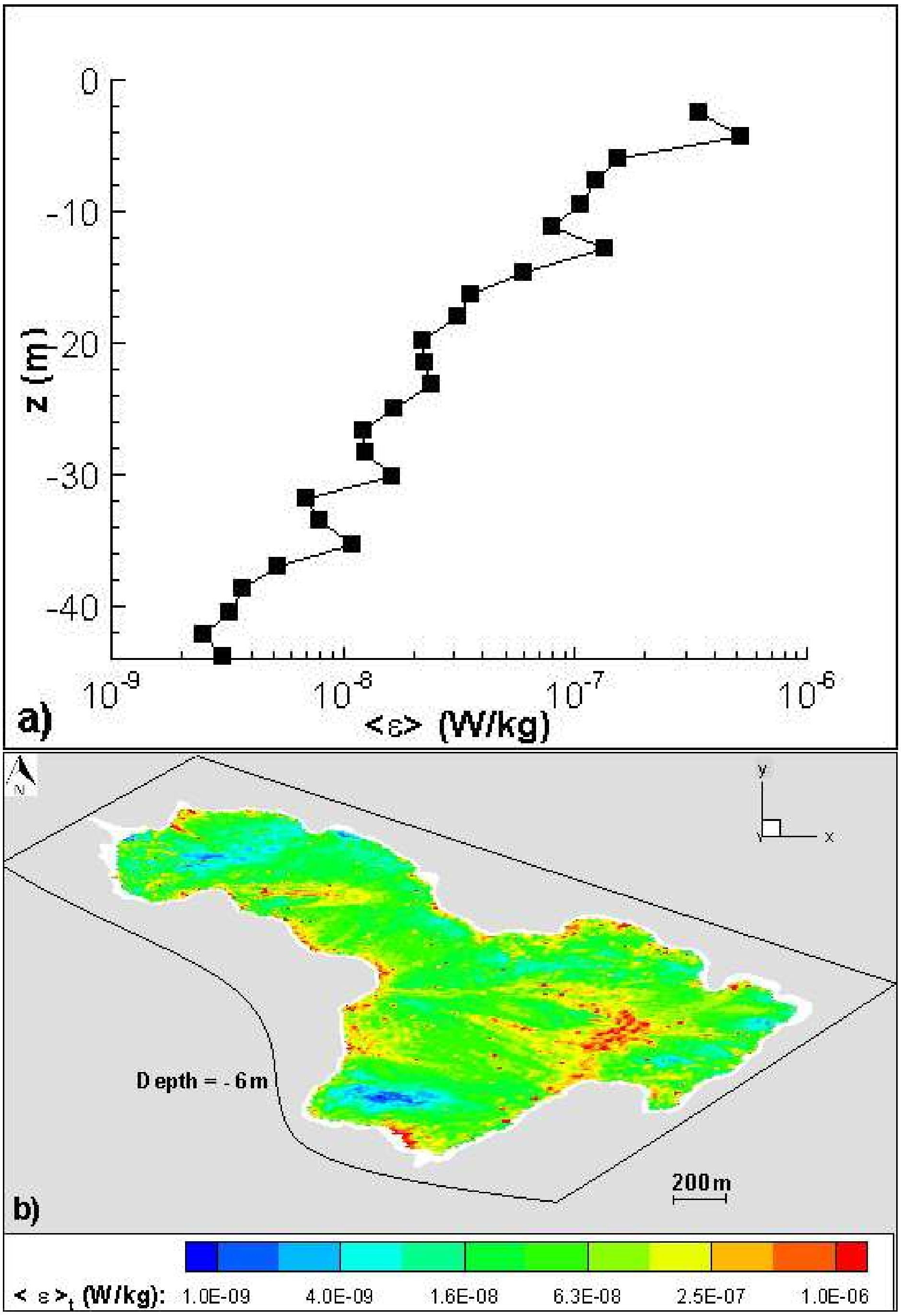

Figure 7.5: SC-HSWC. TKE dissipation rate: a) Vertical profile of $\langle\epsilon\rangle$ averaged over 2 hours, b) contour plot of $\langle\epsilon\rangle_t$ on a horizontal plane at z=-6 m.

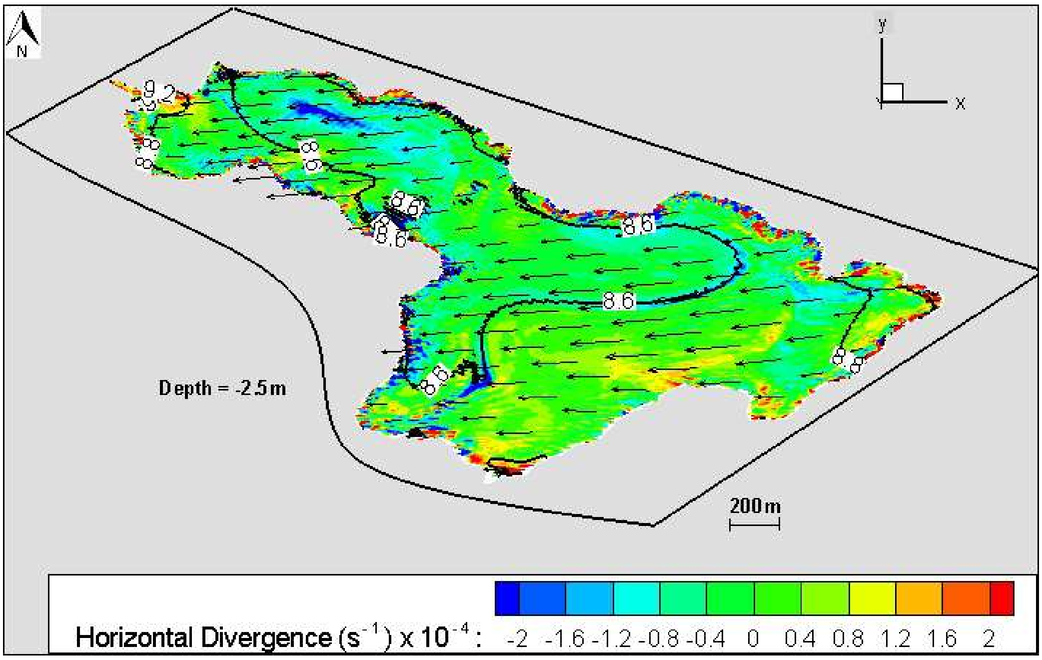

Figure 7.6: SC-IWC. Contour plot at z=-2.5 m of the divergence of the horizontal velocity field together with vectors of the wind field at elevation 2.8 m above the surface of the Lake, and the isotherms of the temperatures in ℃, on day 7 at 13:00.

7.2 Inhomogeneous Wind Field

The present section shows the study of the wind driven circulation generated in Lake Ledro in presence of thermal stratification under the action of inhomogeneous wind.

7.2.1 Velocity Field

Figure 7.6 shows the instantaneous wind field 2.8 m above the water surface and the horizontal divergence of the velocity field over a horizontal plane at $z = -2.5m$ at an instant following a period of strong wind inhomogeneity. As in the IWC, where the stratification is neutral (see Fig. 6.2), the convergence/divergence areas are generated and driven by the wind; such turbulent structures tend to be aligned with the isotherms as it can be seen in Fig. 7.6. These phenomena are associated with the blossom of *P. rubescens* in Lake

Ledro even during spring/autumn periods, that is, in the seasons where stratification is weakened.

7.2.2 Evolution in Time of the Eddy Viscosities, TKE and Its Dissipation Rate

As done for the neutral case, the evolution along the six days of the vertical profiles of the 2-hours space-time averaged $\langle \nu_V \rangle$, $\langle \nu_H \rangle$, TKE and its dissipation rate has been calculated.

Figure 7.7 shows the evolution in time of the vertical profile of the eddy viscosities in the latter six days of simulation in presence of inhomogeneous wind and thermal stratification. With respect to the IWC the aforementioned quantities are smaller in the SC (see Fig.6.6). A phase lag of the values of the two quantities between the surface and the bottom of the lake is appreciable by looking at the Fig. 7.7c: the maximum value of $\langle \nu_H \rangle$ at the bottom appears with approximately 10 hours of delay with respect to the maximum value at the surface which, in turn, is in phase with the wind stress intensity.

In the same way, a phase-lag of the quantities $\langle TKE \rangle$ and $\langle \epsilon \rangle$ between the surface and bottom is most noticeable in the case here discussed with respect to the IWC. Moreover, in Fig. 7.8 in the morning of day 7 the peaks of values of TKE and its dissipation rate are easily recognizable at the surface and also at the bottom of the lake. These phenomena are due to the presence of the thermal stratification: the strong wind squalls produce internal waves which transfer momentum to the bottom more efficiently enhancing the formation of the bottom boundary layer with some hours of delay with respect to the peak of wind intensity. The vertical profile of $\langle TKE \rangle$ and $\langle \epsilon \rangle$ at 08:00 of the day 7 are shown in Fig. 7.9: differently from the HWC and IWC the quantities increase in the bottom boundary layer.

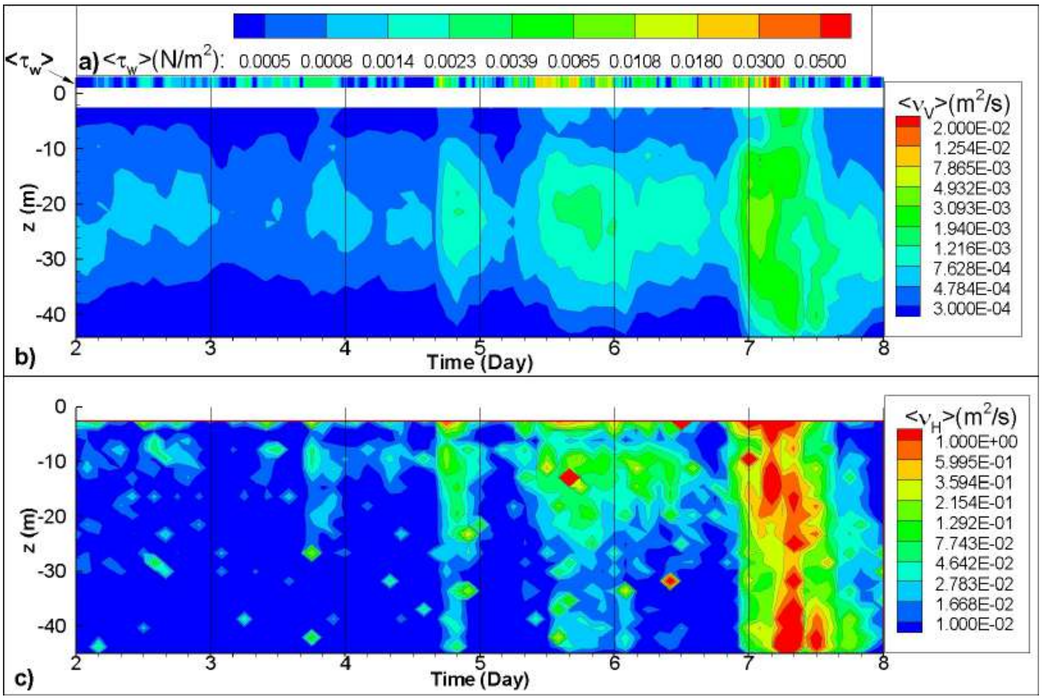

Figure 7.7: SC-IWC. Vertical profiles of space-time quantities averaged over 2 hours along the latter six days of simulation: a) $\langle \tau_w \rangle$; b) $\langle \nu_V \rangle$ and c) $\langle \nu_H \rangle$.

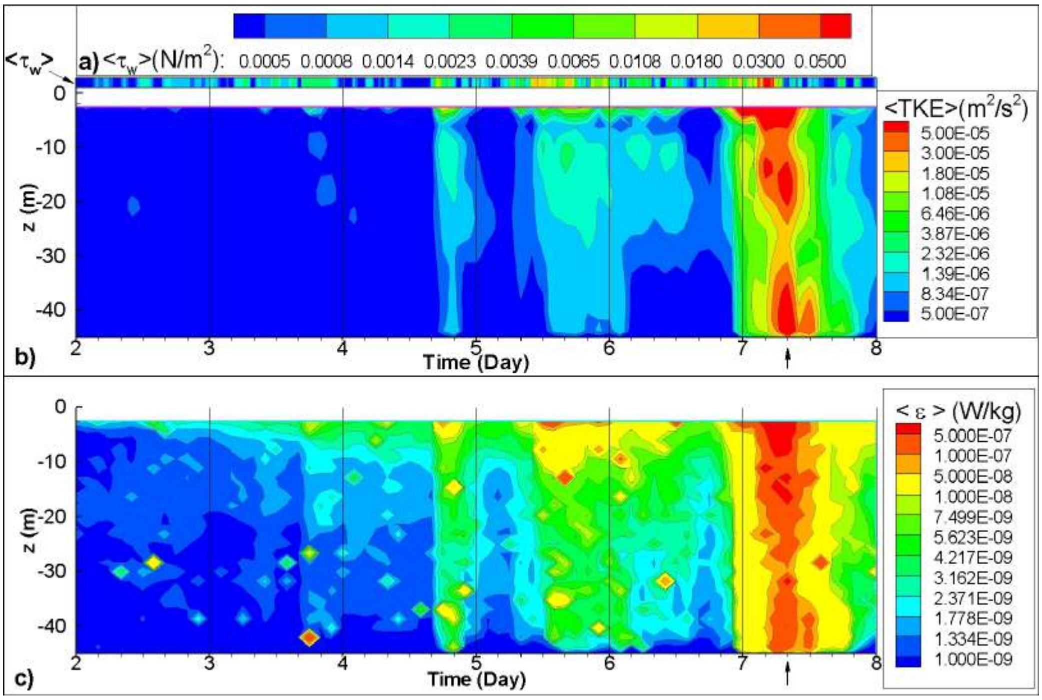

Figure 7.8: SC-IWC. Vertical profiles of space-time quantities averaged over 2 hours along the latter six days of simulation: a) $\langle \tau_w \rangle$; b) $\langle TKE \rangle$ and c) $\langle \epsilon \rangle$. The vertical profile of the $\langle TKE \rangle$ and $\langle \epsilon \rangle$ at the time indicated by the arrow in c) are reported in Fig. 7.9.

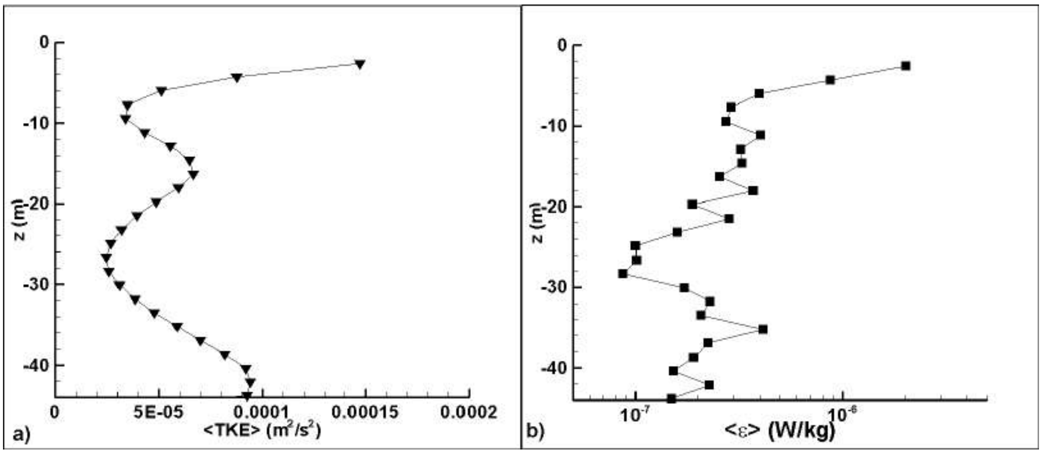

Figure 7.9: SC-IWC. Vertical profile of the space-time a)$\langle TKE \rangle$ and b) $\langle \epsilon \rangle$ averaged over 2 hours between 06:00 and 08:00 of the day 7.

Chapter 8

CONCLUSIONS

An eddy-resolving model (LES-COAST) was applied to study the hydrodynamics and the turbulent structures of a lake as a whole. The case study concerns Lake Ledro, a peri-alpine lake in northern Italy. It has been studied for three main reasons: The lake suffers from metalimnetic blooms of the cyanobacteria *P. rubescens*, which appears at the lake surface during winter in neutrally stratified conditions; its own dimensions are suitable for a high-resolution simulation; it is a significant example of a lake where orographic features affect the wind distribution over the lake surface.

The wind forcing was reproduced using two different conceptual methodologies: first we considered the case of spatially homogeneous wind field with values obtained from measurements at a weather station; successively, we considered an inhomogeneous wind field obtained through a 'local-scale' meteorological simulation, carried out using an atmospheric model (WRF). Two periods of the year have been simulated: the winter period, when the stratification is neutral, and the spring/autumn period when the thermal stratification is weak (i.e. about 5 ℃ difference between surface and bottom). Overall, the analysis shows that:

- The hydrodynamics during the winter months is characterized by the development of a velocity field in the surface boundary layer, which inverts its own direction approximately at a depth of 10 m.
- The Coriolis force plays a role in the dynamics by tilting the velocity

field to the right with respect to the wind direction. This is particularly true under light breeze conditions, where the surface current is weak. Moreover, the rotation of the earth reduces the shear stresses as a consequence of the flattening of the turbulent structures, this reduction is also reflected on the vertical profiles of eddy viscosities.

- Upwelling and downwelling regions are recognized along the leeward and windward coastline respectively in both neutral and stable stratified conditions. The estimation of the vertical uprising associated to the vertical velocity in the upwelling region, may give explanation to the sudden appearance of the cyanobacteria at the lake surface.

- In the neutrally stratified cases no substantial bottom boundary layer activity is present for three main reasons: the time window over which the wind acts steadily along a direction is not long enough to allow for the development of a turbulent bottom boundary layer; The estimation of the surface seiches shows that they are too weak to produce a significant turbulent boundary layer at the bottom of the lake; The absence of large amplitude internal waves associated to stable stratification.

- In agreement with classic literature, the horizontal eddy viscosity is two orders of magnitude larger than the vertical one. When looking at their spatial distribution, they exhibit inhomogeneous behavior over the horizontal planes. The horizontal eddy viscosity is larger in the interior of the lake than close to the coastline, whereas the vertical eddy viscosity is larger along the coasts due to the presence of the boundary layer. The vertical profiles of the space-time averaged eddy viscosities were also discussed. In the neutrally stratified case the horizontal one evidences the presence of a ‘minimum-stress plane’ just below the SBL; the vertical one has its own climax in the core of the water basin. It substantially differs from that obtained for an hypothetical unbounded surface Ekman layer (the typical ocean case) because of the presence of the lateral boundaries reproducing the geometries of the lake and because of the absence of a steady mean wind able to develop a steady-state flow field. Also, the study shows that, under significant wind unsteadiness, the vertical eddy viscosity appears different from the theoretical profile obtained in idealized steady conditions.

In the thermally stratified case with steady wind both the eddy viscosities are larger at the surface and decrease with depth in the SBL. Then the vertical one remains constant and the horizontal one increases slightly by approaching the bottom. Conversely in the non homogeneous wind case the evolution in time of the vertical profiles of the eddy viscosities have smaller values with respect to the neutrally stratified case although preserving the same trend.

- Peculiar superstreaks are reproduced in the interior of the lake in presence of neutral stratification condition. Their lifetime is of the order of hours, they span over the entire depth of the lake and are elongated along the direction of motion. This kind of structures was recently visualized in laboratory experiments of shallow-water wall-bounded turbulence as well as in simulations of Couette flows. They supply vertical mixing in the water column. Conversely, in presence of stable stratification, downwelling and upwelling areas are simulated in correspondence of the wind squalls and are confined in the surface mixed layer where result aligned with the isotherms.

- The turbulent kinetic energy and its dissipation rate in the neutral stratification condition are roughly in phase with the wind forcing. They propagate toward the bottom with a phase lag of some hours with respect to the values at the free surface. Also, they propagate down to the bottom with the same rate indicating the presence of equilibrium turbulence even under the unsteady conditions herein studied. In presence of stable stratification the evolution in time of $\langle TKE \rangle$ and $\langle \epsilon \rangle$ presents smaller values with respect to the neutral stratified IWC and highlights the presence of a BBL.

- The role of a spatially inhomogeneous wind stress was assessed by imposing the wind field simulated by the meteorological model, thus accounting for the sheltering and channeling effects of the surrounding steep orography. We measured the degree of inhomogeneity calculating the RMS deviations of the wind distribution over the lake. Under light breeze conditions, and in presence of small inhomogeneity, the dimensional values of eddy viscosities, TKE and its dissipation rate are more sensitive to the wind intensity and appear slightly affected by inhomogeneity. However, when these quantities are made non dimensional, thus considering them with respect to the wind forcing, it clearly appears that inhomogeneity supplies more mixing. This is particularly true under synoptical events where inhomogeneity is large. Wind inhomogeneity seems to reduce the response time of turbulence within the lake, transferring fluctuations at a faster rate compared to HWC.

- The stable stratification inhibits the vertical circulation and the turbulence in the interior of Lake Ledro. On the other hand, it enhances the formation of internal seiches which are responsible of the transfer of momentum from the wind to the bottom of the lake. Internal seiches do not develop under light breeze conditions, whereas, in presence of wind squalls, they transfer momentum to the bottom, increasing there the values of TKE and of its dissipation rate. The surface mixing layer is characterized by the presence of large convergence and divergence areas either with homogeneous steady wind or with inhomogeneous wind. These turbulent structures result much larger than the superstreaks observed in neutrally stratified condition but differently from them they are confined in the surface layer.

Bibliography

ARRILAGA, J.A., C. YAGUE, M. SASTRE, C. ROMÀN-CASCÒN. 2016. A characterisation of sea-breeze events in the eastern Cantabrian coast (Spain) from observational data and WRF simulations. Atmospheric Research, **181**: 265-280

BARBATO, G. 1977. Note idrobiologiche sul Lago di Ledro.Ann. Mus. Civ. St. Nat. Brescia, **14**: 92-109.

BARRI, M. AND H. I. ANDERSSON. 2010. Turbulent flow over a backward-facing step. Part 1. Effects of anti-cyclonic system rotation. Journal of Fluid Mechanics. **665**: 382-417.

BOSCAINI, A., F. BRESCANCIN, N. SALMASO. 2012. Progetto di ricerca per lo sviluppo dei fattori fisico-chimici che regolano lo sviluppo del cianobatterio Planktothrix Rubescens nel lago di Ledro (in Italian).

BURCHARD, H., P.D. CRAIG, J.R. GEMMRICH, H. VAN HAREN, P.P. MATHIEU, H.M. MEIER, W.A.N.M. SMITH, H. PRANDKE, T.P. RIPPETH, E.D. SKYLLINGSTAD, W.D. SMYTH, D.J. WELSH, H.W. WIJESEKERA. 2008. Observational and numerical modelling methods for quantifying coastal ocean turbulence and mixing. Prog Oceanogr, **76**: 399-442.

D'ALELIO, D., N. SALMASO. 2011. Occurrence of an uncommon Planktothrix (Cyanoprokaryota, Oscillatoriales) in a deep lake south of the Alps. Phycologia, **50**: 379-383.

DITTKO, K.A., M.P. KIRKPATRICK, S.W. ARMFIELD. 2013. Large Eddy

Simulation of complex sidearms subject to solar radiation and surface cooling. Water Research, **47**: 4918-4927.

Galea, A.,M. Grifoll, F. Roman, M. Mestres, V. Armenio, A. Sanchez-Arcilla and L. Zammit Mangion. 2014. Numerical simulation of water mixing and renewals in the Barcelona harbour area: the winter season. Environmental Fluid Mechanics, **14**: 1405-1425.

Giovannini, L., D. Zardi, M. De Franceschi, F. Chen. 2015. Numerical simulations of boundary-layer processes and urban-induced alterations in an Alpine valley. International Journal of Climatology, **34**: 1111-1131.

Giovannini, L., L. Laiti, D. Zardi, M. De Franceschi. 2015. Climatological characteristics of the Ora del Garda wind in the Alps. International Journal of Climatology, **35**:4103-4115.

Hsu, S.A., E.A. Meindl and D.B. Gilhousen. 1994. Determining the power-law wind-profile exponent under near-neutral stability conditions at sea. Journal of Applied Meteorology, **33**: 757-765.

Kundu, P.K., I.M. Cohen, D.R. Dowling. 2012. Fluid Mechanics. Academic Press.

Laiti, L., D. Zardi, M. de Franceschi, G. Rampanelli and L. Giovannini. 2014. Analysis of the diurnal development of a lake-valley circulation in the Alps based on airborne and surface measurements. Atmospheric Chemistry and Physics, **14**: 9771-9786.

Laval, B., J. Imberger, B.R. Hodges and R. Stoker. 2003. Modeling circulation in lakes: spatial and temporal variations. Limnology and Oceanography, **48**: 983-994.

Lee, M.J., J. Kim 1991. The structure of turbulence in a simulated plane Couette flow. Proc.8th Symp. Shear Flows, Munich, Germany, paper 5-3.

Lorke, A., L. Umlauf, T. Jonas and A. Wuest. 2002. Dynamics of turbulence in low- speed oscillating bottom-boundary layers of stratified basins. Environmental Fluid Mechanics, **2**: 291-313.

MIRONOV, D., A. TERZHEVIK, G. KIRILLIN, T. JONAS, J. MALM, D. FARMER. 2002. Radiatively driven convection in ice-covered lakes: Observations, scaling, and a mixed layer model. Journal of Geophysical Research, **107**: C4,3032.

PAPANASTASIOU, D.K., D. MELAS, I. LISSARIDIS. 2010. Study of wind field under sea breeze conditions; an application of WRF model. Atmospheric Research, **98**: 102-117.

PAPAVASSILIOU, D.V., T.J. HANRATTY. 1997. Interpretation of large-scale structures observed in a turbulent plane Couette flow. International Journal of Heat and Fluid Flow, **18**: 55–69.

PETRONIO, A., F. ROMAN, C. NASELLO AND V. ARMENIO. 2013. Large Eddy Simulation model for wind-driven sea circulation in coastal areas, Nonlinear Processes in Geophysics, **20**: 1095-1112.

PIOMELLI, U. 1999. Large-eddy simulation: achievements and challenges. Progress in Aerospace Sciences, **35**: 335-362.

PIOMELLI, U. 2008. Wall-layer models for large-eddy simulations. Progress in Aerospace Sciences, **44**: 437-446.

PODSETCHINE, V. AND G. SCHERNEWSKI. 1999. The influence of spatial wind inhomogeneity on flow patterns in a small lake. Water Research, **15**: 3348-3356.

POPE, S.B. 2000. Turbulent Flows. Cambridge University Press.

POSCH, T., O. KOSTER, M.M. SALCHER AND J. PERNTHALER. 2012. Harmful filamentous cyanobacteria favoured by reduced water turnover with lake warming. Nature Climate Change, **2**: 809-813.

RAMPANELLI, G., D. ZARDI AND R. ROTUNNO. 2004. Mechanisms of up-valley winds. Journal of the Atmospheric Sciences, **61**: 3097-3111

RODI, W., G. COSTANTINESCU, T. STOESSER. 2013. Large-Eddy simulation in hydraulics. CRC Press.

Roman, F., V. Armenio, J. Fröhlich. 2009a. A simple wall layer model for Large Eddy Simulation with immersed boundary method, Physics of Fluids, **21**: 101701.

Roman, F., E. Napoli, B. Milici and V. Armenio. 2009b. An improved immersed boundary method for curvilinear grids. Computers and Fluids, **38**: 1510-1527.

Roman, F., G. Stipcich, V. Armenio, R. Inghilesi, S. Corsini. 2010. Large eddy simulation of mixing in coastal areas. International Journal of Heat and Fluid Flow, **31**: 327-341.

Rubbert, S. and J. Kongeter. 2005. Measurements and three-dimensional simulations of flow in a shallow reservoir subject to small-scale wind field inhomogeneities induced by sheltering. Aquatic Sciences, **67**: 104-121.

Rueda, F.J., S.G. Schladow, S.G. Monismith and M.T.Stacey. 2005. On the effects of topography on wind and generation of currents in a large multi-basin lake. Hydrobiologia, **532**: 139-151.

Salmaso, N., G. Morabito, F. Buzzi, L. Garibaldi, M. Simona and R. Mosello. 2006. Phytoplankton as an indicator of the water quality of the deep lakes south of the Alps. Hydrobiologia, **563**: 167-187.

Salon, S., V. Armenio, A. Crise. 2007. A numerical investigation of the Stokes boundary layer in the turbulent regime. Journal of Fluid Mechanics, **570**: 253-296.

Salon, S., V. Armenio. 2011. A numerical investigation of the turbulent Stokes–Ekman bottom boundary layer. Journal of Fluid Mechanics, **684**: 316-352.

Sander, J., A. Simon, T. Jonas, A. Wüest 2000. Surface turbulence in natural waters' A comparison of large eddy simulations with microstructure observations. Journal of Geophysical Research, **105**: 1195-1207.

SARKAR, S., V. ARMENIO. 2013. Direct and Large Eddy Simulation of Environmental flows. Handbook of Environmental Fluid Dynamics, Vol. two: 283-299.

SCALO, C., L. BOEGMAN, U. PIOMELLI. 2013. Large-eddy simulation and low-order modeling of sediment-oxygen uptake in a transitional oscillatory flow. Journal of Geophysical Research - Oceans, **118**: 1926–1939.

SERAFIN, S., D. ZARDI. 2010. Structure of the atmospheric boundary layer in the vicinity of a developing upslope flow system: a numerical model study. Journal of the Atmospheric Sciences, **67**: 1171-1185.

SKAMAROCK, W.C., J.B. KLEMP, J. DUDHIA, D.O. GILL, D.M. BARKER, M.G. DUDA, X.-Y. HUANG, W. WANG, J.G. POWERS. 2008. A description of the advanced research WRF version 3. NCAR Technical Note TN-475+STR, 125.

SMAGORINSKY, J. 1963. General circulation experiments with the primitive equations. Monthly Weather Review, **91**: 99-120.

TEJADA-MARTINEZ, A. E., AND C. E. GROSCH 2007. Langmuir turbulence in shallow water. Part 2. Large-eddy simulation. Journal of Fluid Mechanics, **576**: 63-108.

TOFFOLON, M., AND G. RIZZI. 2009. Effects of spatial wind inhomogeneity and turbulence anisotropy on circulation in an elongated basin: a simplified analytical solution. Advances in Water Resources, **32**: 1554-1566.

TOFFOLON, M. 2013. Ekman circulation and downwelling in narrow lakes. Advances in Water Resources, **53**: 76-86.

WHITTON, B.A. 2012. Ecology of Cyanobacteria II: Their Diversity in Space and Time, Springer Netherlands.

WU, J. 1982. Wind-stress coefficient over sea surface from breeze to hurricane. 1982. Journal of Geophysical Research, **87**: 9704-9706.

WUEST, A., G. PIEPKE, D.C. VAN SENDEN. 2000. Turbulent kinetic energy balance as a tool for estimating vertical diffusivity in wind-forced stratified waters. Limnologly and Oceanography, **45**: 1388-1400.

WUEST, A. AND A. LORKE. 2003. Small-Scale Hydrodynamics in lakes. Annual Review of Fluid Mechanics, **35**: 373-412.

ZANG, J., R. STREET, J. KOSEFF 1994. A non-staggered grid, fractional step method for the time-dependent incompressible Navier-Stokes equations in curvilinear coordinates. Journal of Computational Physics, **114**: 18-33.

ZIKANOV, O., D.N. SLINN, M.R. DHANAK. 2003. Large-eddy simulations of the wind-induced turbulent Ekman layer. Journal of Fluid Mechanics, **495**: 343-368.